THE PRESSURE EFFECT ON PARTICLE SIZE DISTRIBUTION OF RECYCLING NDFEB MAGNETS

A THESIS SUBMITTED TO
THE GRADUATE SCHOOL OF NATURAL AND APPLIED SCIENCES
OF
MIDDLE EAST TECHNICAL UNIVERSITY

BY

GİZEM ÖZALTUN

IN PARTIAL FULFILLMENT OF THE REQUIREMENTS
FOR
THE DEGREE OF MASTER OF SCIENCE
IN
METALLURGICAL AND MATERIALS ENGINEERING

DECEMBER 2024

Approval of the thesis:

THE PRESSURE EFFECT ON PARTICLE SIZE DISTRIBUTION OF RECYCLING NDFEB MAGNETS

submitted by **GİZEM ÖZALTUN** in partial fulfillment of the requirements for the degree of **Master of Science** i**n Metallurgical and Materials Engineering, Middle East Technical University** by,

Prof. Dr. Naci Emre Altun
Dean, **Graduate School of Natural and Applied Sciences** _____

Prof. Dr. Ali Kalkanlı
Head of the Department, **Met. and Mater. Eng., METU** _____

Prof. Dr. Mahmut Vedat Akdeniz
Supervisor, **Metallurgical and Materials Eng., METU** _____

Assoc. Prof. Dr. Öznur Çakır
Co-Supervisor, **Met. and Mater. Eng., Yildiz Technical Uni.** _____

Examining Committee Members:

Prof. Dr. Ali Kalkanlı
Metallurgical and Materials Eng, METU _____

Prof. Dr. Mahmut Vedat Akdeniz
Metallurgical and Materials Eng., METU _____

Assoc. Prof. Dr. Öznur Çakır
Metallurgical and Materials Eng., Yildiz Technical Uni. _____

Assist. Prof. Dr. Yusuf Keleştemur
Metallurgical and Materials Eng., METU _____

Assist. Prof. Dr. Şeniz Uçar
Metallurgical and Materials Eng., METU _____

Date: 05.12.2024

I hereby declare that all information in this document has been obtained and presented in accordance with academic rules and ethical conduct. I also declare that, as required by these rules and conduct, I have fully cited and referenced all material and results that are not original to this work.

Name Last name : Gizem Özaltun

Signature :

ABSTRACT

THE PRESSURE EFFECT ON PARTICLE SIZE DISTRIBUTION OF RECYCLING NDFEB MAGNETS

Özaltun, Gizem
Master of Science, Metallurgical and Materials Engineering
Supervisor: Prof. Dr. Mahmut Vedat Akdeniz
Co-Supervisor: Assoc. Prof. Dr. Öznur Çakır

December 2024, 98 pages

Rare earth permanent magnets (REPMs), specifically NdFeB magnets, play a crucial role in industries due to their improved magnetic performance. However, sustainable alternatives, such as recycling, are needed, as there are significant geopolitical supply concerns regarding the dependence on rare earth elements (REEs), which are also included in the list of critical raw materials identified by the European Commission. The objective of this thesis is to investigate the impact of hydrogen pressure on scrap NdFeB magnets using different characterization techniques to obtain ideal particle size distribution for further manufacturing steps. In this study, scrap NdFeB permanent magnets from hard disk drives were subjected to the hydrogen decrepitation (HD) process at different pressures (2, 4, and 6 bar) followed by a ball-milling process. Magnetic measurements showed the demagnetization of HD powders, a consequence of hydrogen entering the structure. Unexpectedly, M/H tests revealed that ball-milled powders had increased coercivity. The X-ray diffraction analysis showed the formation of $Nd_2Fe_{14}B_{3.31}$ and Nd_2O_3 phases, confirming that there is no NdH_2 phase formation at room temperature. The research additionally demonstrated differences in the expected hydrogen concentration associated with pressure. The 4 bar HD powders, which showed the highest $Nd_2Fe_{14}B_{3.31}$ phase

content and the least amount of oxide phase, were found to have the best conditions for further processing. Characterization of the particle size distribution showed that when hydrogen pressure got higher, the particle size dramatically reduced. However, the excessive particle size reduction after ball-milling showed that it was a consequence of the prolonged milling time.

Keywords: Recycling, Permanent Magnet, Hydrogen Decrepitation

ÖZ

ÖMRÜ TAMAMLANMIŞ NDFEB MIKNATISLARIN PARÇACIK BOYUTU DAĞILIMINDA BASINÇ ETKİSİ

Özaltun, Gizem
Yüksek Lisans, Metalurji ve Malzeme Mühendisliği
Tez Yöneticisi: Prof. Dr. Mahmut Vedat Akdeniz
Ortak Tez Yöneticisi: Doç. Dr. Öznur Çakır

Aralık 2024, 98 sayfa

Nadir toprak kalıcı mıknatıslar, özellikle de NdFeB mıknatısları, gelişmiş manyetik performansları nedeniyle endüstrilerde çok önemli bir rol oynamaktadır. Ancak, Avrupa Komisyonu tarafından belirlenen kritik hammaddeler listesinde de yer alan nadir toprak elementlerine bağımlılıkla ilgili önemli jeopolitik tedarik endişeleri duyulmasından dolayı geri dönüşüm gibi sürdürülebilir alternatiflere ihtiyaç bulunmaktadır.

Bu tezin amacı, ideal parçacık boyutu dağılımını elde etmek için farklı karakterizasyon teknikleri kullanarak hidrojen basıncının hurda NdFeB mıknatıslar üzerindeki etkisini araştırmaktır. Çalışmada, sabit disk sürücülerinin hurda NdFeB kalıcı mıknatısları kullanılarak farklı basınçlarda (2, 4 ve 6 bar) hidrojen ile kırma (HD) işlemi yapıldıktan sonra bilyalı öğütme işlemi gerçekleştirilmiştir. Manyetik ölçümler, yapıya giren hidrojenin bir sonucu olarak HD tozlarının demanyetize olduğunu göstermiştir. Beklenmedik bir şekilde, M/H testleri, bilyeyle öğütülmüş tozların artan zorlayıcılığa sahip olduğunu ortaya koymuştur. Analizler, $Nd_2Fe_{14}B_{3.31}$ ve Nd_2O_3 fazlarının oluşumunu ortaya çıkararak oda sıcaklığında NdH_2 fazı oluşumu olmadığını doğrulamıştır. Araştırma ayrıca basınçla ilişkili beklenen hidrojen

konsantrasyonunda farklılıklar göstermiştir. En yüksek $Nd_2Fe_{14}B_{3.31}$ faz içeriğini ve en az oksit miktarını gösteren 4 bar HD tozlarının sonraki işlemler için en iyi koşullara sahip olduğu bulunmuştur. Parçacık boyutu dağılımının karakterizasyonu, hidrojen basıncı yükseldiğinde parçacık boyutunun önemli ölçüde azaldığını göstermiştir. Ancak, bilyalı öğütme sonrasında parçacık boyutundaki aşırı düşüş, bunun uzun öğütme süresinin bir sonucu olduğunu göstermiştir.

Anahtar Kelimeler: Geri Dönüşüm, Kalıcı Mıknatıs, Hidrojenle Kırma

To My Beloved Family,

Nuray and Gözde

ACKNOWLEDGMENTS

I would like to express my deepest gratitude to my supervisor, Prof. Dr. Mahmut Vedat Akdeniz, for his understanding, support, guidance, encouragement, and constructive feedback throughout the research.

I am grateful to my co-supervisor Assoc. Prof. Dr. Öznur Çakır for her guidance, with precious ideas, valuable feedback, constructive criticism, and support throughout this work.

I would like to thank my colleagues and friends, Senem Sarıtaş Batan, Cansu Kaplan, Gizem Kaplan, Tülay Koç Delice, Gülşah Türker, Furkan Akpunar, Nasuh Arık, and Özden Acar for their assistance and wise advices.

I want to express my heartfelt gratitude to my friend, practically my sister, Ceren Göktaş for her unwavering support and presence, not only for her invaluable help in this study but also for being an integral part of my life.

Finally, I must extend my deepest gratitude to my mother Nuray, and my sister Gözde, for their never-ending support in this study and throughout my life, for doing their best in everything they can help me with, emotional support, belief in me, in short, for being my family.

TABLE OF CONTENTS

ABSTRACT v

ÖZ vii

ACKNOWLEDGMENTS x

TABLE OF CONTENTS xi

LIST OF TABLES xiv

LIST OF FIGURES xv

LIST OF ABBREVIATIONS xviii

LIST OF SYMBOLS xix

CHAPTERS

1 INTRODUCTION 1

2 LITERATURE REVIEW 5

2.1 Origin of Magnetism 5

2.2 Magnetic Domains 6

2.3 Fundamental Concepts of Magnetic Properties 8

2.3.1 Intrinsic Magnetic Properties 9

2.3.2 Extrinsic Properties 12

2.4 Permanent Magnets 16

2.4.1 Overview of NdFeB Magnets 20

2.5 Production of NdFeB Magnets 25

2.5.1 Effect of Particle Size Distribution on Microstructure and Magnetic Properties 31

2.6 Recycling of NdFeB Magnets 33

2.6.1 Hydrogen Decrepitation Process 34

3 EXPERIMENTAL PROCEDURE 41
3.1 Starting Materials 41
3.2 Sample Preparation 42
3.3 Experimental Techniques 43
3.3.1 Hydrogen Decrepitation Process 43
3.3.2 Ball Milling 44
3.4 Characterization Techniques 45
3.4.1 Chemical Composition Analysis 45
3.4.2 Microstructural Analysis 46
3.4.3 Magnetic Measurement 47
3.4.4 Particle Size Analysis 47
3.4.5 Oxygen and Hydrogen Contents 47
3.4.6 X-Ray Diffraction (XRD) Analysis 48
4 RESULTS AND DISCUSSION 51
4.1 Inductively Coupled Plasma Optical Emission Spectroscopy 51
4.2 Microstructural Examination 52
4.2.1 Before Hydrogen Decrepitation Process 52
4.2.2 After Hydrogen Decrepitation Process 54
4.3 Magnetic Measurement 59
4.4 Oxygen and Hydrogen Content 61
4.5 X-Ray Diffraction 62
4.6 Particle Size Distribution 72
5 CONCLUSION AND FUTURE RECOMMENDATIONS 81
5.1 Conclusions 81

5.2 Future Recommendations 84

REFERENCES 87

LIST OF TABLES

TABLES

Table 2.1 Magnetic properties of some permanent magnets [1]. 18
Table 2.2 Invariant and monovariant reactions for the NdFeB ternary system [41]. 24
Table 4.1 The composition of the scrap NdFeB magnet with standard deviations . 52
Table 4.2 Chemical composition (wt%) of the protective coating 54
Table 4.3.Oxygen and Hydrogen contents (wt%). 61
Table 4.4 Lattice parameters of $Nd_2Fe_{14}B$ phase and Rietveld parameters for demagnetized NdFeB magnet. 63
Table 4.5 XRD phase analysis results (wt%) for 2 bar HD, 4 bar HD, and 6 bar HD. 66
Table 4.6 Lattice parameters of $Nd_2Fe_{14}BH_{3.31}$ phase and Rietveld parameters for 2 bar HD, 4 bar HD, and 6 bar HD. 67
Table 4.7 XRD phase analysis results (wt%) for 2 bar BM, 4 bar BM and 6 bar BM. 70
Table 4.8 Lattice parameters of $Nd_2Fe_{14}BH_{3.31}$ phase and Rietveld parameters for 2 bar BM, 4 bar BM, and 6 bar BM. 71
Table 4.9 The position, FWHM, crystalline size, and microstrain for the observed peak having the highest intensity 71
Table 4.10 D10, D50, and D90 values based on the cumulative amount after the HD process 76
Table 4.11 D10, D50, and D90 values based on the percentage of the cumulative amount after ball-milling 79

LIST OF FIGURES

FIGURES

Figure 2.1 Representation of the division of magnetization into domains a) single domain, b) two domains, c) four domains, and d) closure domain [12] 7
Figure 2.2 180° twist boundary's shift in the magnetic dipoles' orientation [9]. 8
Figure 2.3 Graphical magnetization curves for a ferromagnet where the field is pointed in both the easy and hard directions [9]. 12
Figure 2.4 Schematic representation of a) B-H and b) M-H hysteresis loops 13
Figure 2.5 Diagrammatic representation of the distinction between soft and hard magnets in a hysteresis loop. 14
Figure 2.6 Representation of (BH)max in a hysteresis loop. 16
Figure 2.7 Different devices contain permanent magnets [14]. 17
Figure 2.8 Development of the energy product BHmax for commercial permanent magnets during the last few decades at room temperature [30]. 18
Figure 2.9 Illustration of a) an isotropic magnetic material with randomly aligned crystallographic axes of different grains, b) anisotropic magnetic material with parallel aligned crystallographic axes of different grains. 20
Figure 2.10 The tetragonal unit cell of $Nd_2Fe_{14}B$ [37]. 21
Figure 2.11 The liquid phase projection of the NdFeB ternary system, where U = transition, p = peritectic, e = eutectic, and E = ternary eutectic [44] 23
Figure 2.12 Binary phase diagram of the NdFeB alloy [44]..... 25
Figure 2.13 Representation of magnetic properties of the permanent magnets [38]. 26
Figure 2.14 A schematic illustration of typical manufacturing steps of NdFeB alloy [22]. 28
Figure 2.15 Mean size of particles compared to the powder input rate to the jet mill [12]. 29
Figure 2.16 Schematic drawing of the HD process of NdFeB magnet [82] 35

Figure 2.17 Diagrammatic illustration of the various fracture forms that may arise during the HD process: a) starting sample, b) intergranular and transgranular cracking c) entirely intergranular cracking, d) inadequate intergranular cracking [76]. 36
Figure 2.18 Variation in coercivity with degassing temperature of HD powder of sintered material [84].....37
Figure 3.1 Inside of the HDD. 41
Figure 3.2 a) VCM assembly b) NdFeB magnets in VCM assembly c) NdFeB magnets after separation of VCM assembly.....42
Figure 3.3 Fresh surfaces after the coating removal and hydrogen penetration into the magnet 43
Figure 3.4 a) The hydrogenation reactor b) Preparation of the reactor in the glove box c) Magnet powders separated from the VCM assembly after the HD process 44
Figure 3.5 Spex Sampleprep 8000D Mixer/Mill. 45
Figure 3.6 a) Placement of the jar in a vacuum pack to prevent oxygen contact during the BM process b) Dried powders after the BM process.....45
Figure 3.7 HITACHI SU5000 FE-SEM. 46
Figure 3.8 GMW Magnet Systems Model 3473-70 Electromagnet VSM 47
Figure 3.9 LECO TCH 600. 48
Figure 3.10 X-ray diffractometer (Malvern Panalytical/Empyrean). 49
Figure 4.1 A schematic representation of the results and discussion chapter. 51
Figure 4.2 SE image of the microstructure of the sintered scrap magnet.....53
Figure 4.3 BSE images of protective coating a) at 2500x magnification and b) at 10,000x magnification.....53
Figure 4.4 SEM images of intergranular and enclosed transgranular cracks, spherical Nd-rich phase, and its micro-indent impression after the HD processing at a) 2 bar (1), b) 2 bar (2) c) 4 bar, d) 6 bar. e) Closer look at the spherical Nd-rich phase. ..55
Figure 4.5 SE images of a) 2 bar HD, b) 4 bar HD, c) 6 bar HD powders at 1000x magnification. 56

Figure 4.6 SE images of a) 2 bar BM, b) 4 bar BM, c) 6 bar BM powders at 500x magnification, d) 2 bar BM, e) 4 bar BM, f) 6 bar BM powders at 10,000x magnification. 58
Figure 4.7 a) M-H graphs of scrap NdFeB magnet and, 2 bar, 4 bar, and 6 bar HD powders b) closer look at HD powders M/H curves 59
Figure 4.8 a) M-H graphs of scrap NdFeB magnet and, 2 bar, 4 bar, and 6 bar BM powders b) closer look at BM powders M/H curves 60
Figure 4.9 XRD pattern of the scrap NdFeB magnet before the HD process. 63
Figure 4.10 XRD pattern of 2 bar HD 65
Figure 4.11 XRD pattern of 4 bar HD 65
Figure 4.12 XRD pattern of 6 bar HD 66
Figure 4.13 Comparison of XRD peaks of a) the scrap NdFeB magnet before the HD process, b) 2 bar HD, c) 4 bar HD, and d) 6 bar HD. 67
Figure 4.14 XRD patterns of 2 bar BM 68
Figure 4.15 XRD patterns of 4 bar BM 69
Figure 4.16 XRD patterns of 6 bar BM 69
Figure 4.17 SEM images of particle size measurement of a) 2 bar HD, and b) 2 bar BM powders 73
Figure 4.18 The graph of the particle size distribution for 2 bar HD powder 74
Figure 4.19 The graph of the particle size distribution for 4 bar HD powder 74
Figure 4.20 The graph of the particle size distribution for 6 bar HD powder 75
Figure 4.21 The graph of the particle size distribution for 2 bar BM powder 77
Figure 4.22 The graph of the particle size distribution for 4 bar BM powder 77
Figure 4.23 The graph of the particle size distribution for 6 bar BM powder 78

LIST OF ABBREVIATIONS

ABBREVIATIONS

REEs	Rare Earth Elements
PMs	Permanent Magnets
REPMs	Rare Earth Permanent Magnets
CRMs	Critical raw materials
EoL	End-of-Life
HD	Hydrogen Decrepitation
HDDR	Hydrogenation-Disproportionation-Desorption-Recombination
GMRL	General Motors Research Laboratories
HREE	Heavy Rare Earth Element
TRL	Technology-Readiness Level
VCM	Voice Coil Motors
XRD	X-Ray Diffraction
FWHM	Full Width at Half Maximum
ICP-OES	Inductively Coupled Plasma Optical Emission Spectroscopy
MtM	Magnet-to-Magnet
FE-SEM	Field Emission-Scanning Electron Microscope
EDS	Energy Dispersive X-ray Spectroscopy
SE	Secondary Electron
BSE	Backscattering Electron

LIST OF SYMBOLS

SYMBOLS

μ_{orb}	Orbital magnetic moment
μ_s	Spin magnetic moment
χ	Magnetic susceptibility
μ	Permeability
Φ	Flux density concentration
M_s	Saturation (or spontaneous) magnetization
T_c	Curie temperature
m	Magnetic moment
V	Volume
K_1	Anisotropy constant
E_a	Magnetic anisotropy energy
B	Magnetic induction
(BH)max	Maximum energy product
M	Magnetization
H	Magnetic field
B_r	Remanent induction
M_r	Remanent magnetization
H_d	Demagnetization field
H_c	Coercivity

iH_c	Intrinsic coercivity
ϕ, T1	$Nd_2Fe_{14}B$
η, T2	$Nd_{1+\varepsilon}Fe_4B_4$
ρ, T3	Nd-rich Phase
β	FWHM
λ	X-ray wavelength
Å	Angstrom
χ^2	Chi-Square

CHAPTER 1

INTRODUCTION

Permanent magnets (PMs) are widely used in diverse commercial and residential products, automobiles, and aerospace industries. Their unique technological importance stems from their ability to make an attractive or repulsing action in accordance with the material without coming into contact with a ferromagnetic material, as well as to supply a constant magnetic flux without requiring any energy input or operational expenses for commercial rare earth permanent magnets (REPMs) based on the SmCo intermetallic compound have been developed. The discovery of the Sm-Co magnets resulted from searching for novel magnetic materials with an energy density greater than that of the Alnico PMs. However, the expense of producing the magnets prevented the Sm-Co-based magnets from being developed further on a global scale. The cost of the components was high, and the cobalt supply was unpredictable and inconsistent [1].

Two simultaneous discoveries of the $Nd_2Fe_{14}B$ resulted from several attempts to develop permanent magnets at a lower cost. In 1984, Sumitomo Special Metals Co. in Japan announced the discovery using a method similar to producing $SmCo_5$. In parallel with this, General Motors released a composition that was similar but made using a slightly different process based on rapid solidification technology. Since they have comparatively reduced cost than SmCo, the magnets manufactured by both techniques are commercially available on a large scale and have replaced Sm/Co alloys [2].

REPMs have widespread usage in an expanding range of industries and applications. Most of the applications for REPMs are the ones that come with weight, size, and performance constraints. Because of their exceptional performance, REPMs are

crucial for the minimization of a broad spectrum of devices and apparatus. Owing to their distinct physical characteristics, REPMs find considerable application in fields that include electric motor vehicles, wind turbines, and defense-related applications. The availability of rare earth elements (REEs) has become a significant societal concern, particularly as these materials are listed on various "critical minerals" and "critical metals" lists by global and regional organizations. For industrial customers and governments outside of China, the concentration of rare earth mining in China poses a geopolitical supply risk [3]. In December 2023, China established export prohibitions and limitations on critical minerals and technology. These consisted of the prohibitions on certain methods of extracting and separating REEs as well as methods for producing REPMs and compounds. Moreover, restrictions were broadened to encompass all previously unprohibited methods of rare-earth mining, mineral processing, and smelting. China is currently the largest producer of a number of critical mineral materials in the world. Therefore, its activities have raised concerns about their significance, especially as a number of these materials are designated on the United States critical minerals list [4].

In 2023, the European Commission released a list of raw materials that are essential in multiple new technological advances, emphasizing their susceptibility to shortages or political unrest. The EU list categorizes critical raw materials (CRMs) as having a high supply risk and significant economic relevance for the EU [5]. The evaluation attempts to identify risks and possibilities connected with CRMs after carefully examining the political and economic situations of the producing nations, the degree of supply concentration, the possibility for substitution, and the recycling rates [6]. This list also reveals that the global population, industrialization, digitization, the growing demand from developing countries as well as shifting towards climate neutrality concerning metals, minerals, and biological materials in low-emission technologies and products will be more of a pressure. Identified by the European Commission as the most supply risk material is the REEs [5].

Some European countries that do not have sufficient reserves of these materials are now turning their attention towards improving the recovery and recycling of REE

from alternative (secondary) sources. The recycling of the CRMs can provide supply security for a country to meet its needs in the future.

Recycling CRMs, including REEs, addresses significant environmental concerns, in which the use of rare earths from primary sources requires significant amounts of water, as well as significant amounts of energy and the use of acidic substances during the extraction process. Using End-of-Life (EoL) products as a source has lower emission and pollutant values than primary sources. By recycling REEs, these environmental impacts can be mitigated, promoting a more sustainable approach to resource management.

In this thesis study, the objective is to investigate how different pressures during the hydrogen decrepitation (HD) process impact the particle size of the scrap NdFeB magnet, which is a critical parameter in NdFeB magnet production. In this thesis, the topics covered in the study are given into five main chapters:

Chapter 2 involves the literature review, which provides fundamental information about magnetism and magnetic properties, together with an overview of permanent magnets covering their history and types. This chapter is also devoted to NdFeB magnets, presenting details regarding their crystal structure, phases in the alloy, production, and the effect of particle size during production. Moreover, the recycling of NdFeB magnets is considered, and its emphasis includes the hydrogen decrepitation process.

Chapter 3 covers the experimental procedure used for the HD process of scrap NdFeB magnets, their ball milling stage, and testing.

The experimental results regarding microstructural, structural and magnetic tests, with the respective discussions of each result, are presented in Chapter 4.

Finally, Chapter 5 presents significant conclusions reached at the end of the study. The thesis concludes with future studies that are believed to be helpful for other works and dissertations that will be undertaken on related subject.

CHAPTER 2

LITERATURE REVIEW

2.1 Origin of Magnetism

The theory of electromagnetism which explains how electric currents can generate magnetic fields, was established in the 19th century by Faraday and Maxwell. Understanding the origins of magnetism through electron motion and interactions has advanced as a result of this fundamental work. The two main sources of magnetism at the atomic level are orbital magnetic moments (μ_{orb}), due to electron movement around the nucleus, and spin magnetic moments (μ_s), from the movement of electrons on their axes, and additionally, spin-orbit interactions providing a further contribution. A material's total magnetic moment is determined by these components considered together, which affects its magnetic behavior and characteristics [7], [8].

The reaction of a material to an applied magnetic field, H, is referred to as its magnetic induction, B, and magnetization, M, are influencing variables for B, and M is the measure of magnetic moment per unit volume;

$$M = \frac{m}{V} \ \frac{emu}{cm^3} \quad (\textit{Equation 1})$$

The relationship between B, H, and M can be stated as follows:

$$B = \mu_0(H + M) \text{ (in SI unit), or } B = H + 4\pi M \text{ (in cgs unit), } (\textit{Equation 2})$$

where the permeability of free space is denoted by μ_0, which is the resistance experienced when creating a magnetic field in a classical vacuum. Permeability, μ is defined as the B/H ratio:

$$\mu = \frac{B}{H} \quad (\textit{Equation 3})$$

The ratio of M to H is called susceptibility, χ:

$$\chi = \frac{M}{H} \quad (\textit{Equation 4})$$

While μ displays how permeable a material is to a magnetic field, χ, a dimensionless property, shows how receptive a material is to an external magnetic field.

A high permeability material is one that has a high internal flux density concentration, Φ, which is the determination of the density of magnetic field lines. The flux density, Φ, inside the medium is equivalent to the B, Accordingly, $B = \Phi/A$ within a material is like $H = \Phi/A$ in free space. The flux density inside a material generally differs from outside. Based on this difference, materials can be categorized as diamagnetic if Φ inside is less than the outside, paramagnetic, or antiferromagnetic if slightly greater, and ferromagnetic or ferrimagnetic if much greater [9].

2.2 Magnetic Domains

In ferromagnetic materials, magnetic domains are regions where atomic magnetic moments are uniformly aligned, enabling the material to exhibit magnetization. The theory, first put out by Weiss in 1906 and expanded upon by researchers involving Ewing, Landau, and Lifschitz, describes how spontaneous magnetization can occur in the absence of an external magnetic field without changing the overall net magnetization [10].

Individual domains of ferromagnetic materials such as iron, cobalt, or nickel show spontaneous magnetization (M_s) in a macroscopic volume. However, the vector sum of these magnetizations results in zero net magnetization because of their random orientations. This cancellation occurs due to magnetic flux lines producing self-

demagnetizing fields, called the demagnetization field (H_d), which lead the dipoles to become misaligned and contribute to the overall energy of the material, specifically termed magnetostatic energy [11].

The formation of magnetic domains emerges as a strategy to minimize the magnetostatic energy of the system. The material can achieve a lower overall energy state by decreasing the self-demagnetizing fields [11]. For instance, because of the surface charges at its ends, a single, uniformly magnetized domain would have a large magnetostatic energy and generate strong self-demagnetizing fields as shown in Figure 2.1 (a). On the other hand, separating the material into several domains enables a configuration that reduces the overall energy and minimizes these effects. This reduction in the magnetostatic energy with increasing domain number can be seen in Figure 2.1 (b, c). These domains begin to align when an external magnetic field is introduced, increasing the overall magnetization until saturation is reached. To eliminate magnetostatic energy, a domain pattern that provides no magnetic poles at the block's surface is required. A method for doing this is illustrated in Figure 2.1(d).

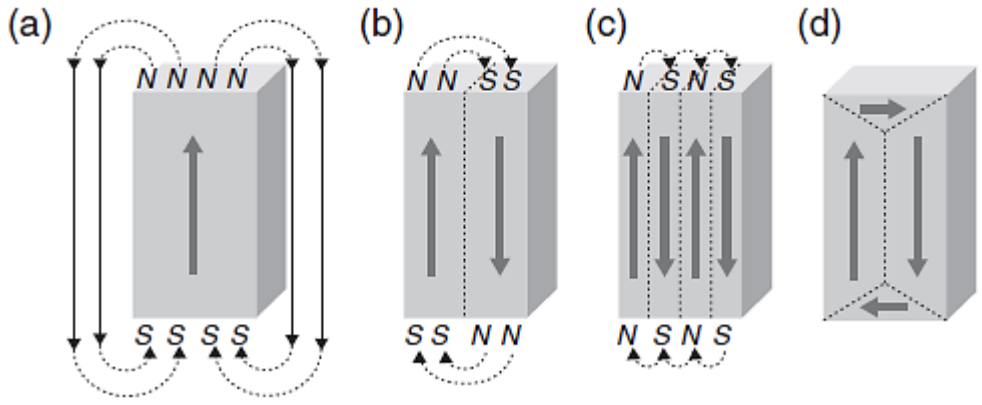

Figure 2.1 Representation of the division of magnetization into domains a) single domain, b) two domains, c) four domains, and d) closure domain [12]

Each domain wall, also known as a Bloch wall, represents the transition region between adjacent domains with differing magnetization directions. Between two domains, the magnetization in the wall progressively shifts from one favored

direction to the other, usually 180^0 or 90^0 [13]. One example of such a wall is the twist boundary, shown in Figure 2.2 for a 180^0 boundary [9]. The thickness of this wall results in an optimization between exchange energy, which favors parallel alignment of moments and wider walls to minimize the angle of change, and magnetocrystalline anisotropy energy, which encourages narrower walls with sharper transitions for better alignment with easy axes. The domain wall types that have no magnetic poles inside the material and avoid generating demagnetizing forces are the most energetically favourable.

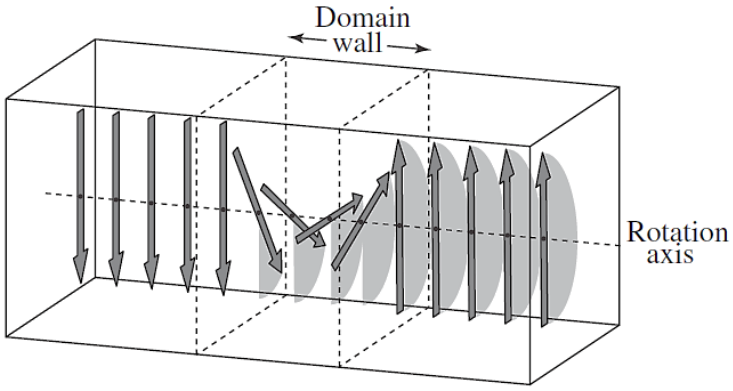

Figure 2.2 180° twist boundary's shift in the magnetic dipoles' orientation [9].

2.3 Fundamental Concepts of Magnetic Properties

The magnetic properties of materials are one of the most important parameters that explain their behavior when exposed to an external magnetic field. The complexity of these properties speaks to the need to address fundamental questions: where do the sources of magnetic moments originate, what process occurs when a magnetic field interacts with matter, and how can materials be classified based on their behavior in a magnetic field. This section investigates the magnetic properties which are categorized as either intrinsic or extrinsic [14], [15], [16]. In this way, the stage is prepared for the verification and further use of magnetic materials in various fields.

2.3.1 Intrinsic Magnetic Properties

The intrinsic magnetic properties, such as saturation magnetization (M_s), the Curie temperature (T_c), magnetic anisotropy, and magnetocrystalline anisotropy typically reflect the atomic origin of magnetism. These are properties of the chemical composition and crystal structure that are independent of the microstructure, including the distribution and existence of impurities and pores, as well as characteristics like crystallite or grain size. The iron-series (or 3d) transition-metal sublattice is crucial in defining the Ms and Tc for almost all PMs. Although some heavy atoms (4d, 5d, 4f, and 5f) also possess a magnetic moment, m, due to their larger atomic volume, V, their magnetism is reduced (Ms=m/V) [7], [17]**.**

2.3.1.1 Saturation Magnetization

The net magnetic moment of a material per unit volume is known as saturation magnetization (M_s). If the magnetization value remains unchanged even when the external field increases, saturation has occurred and all domains align with the applied field's direction. Domain alignment is improved by increasing the intensity of the externally applied field [7].

The ferromagnetic state disappears above Tc, and the value of Ms reduces with higher temperatures because of higher thermal disorder. When the temperature drops below Tc, the ferromagnetic state returns, demonstrating the complete reversibility of this behavior [12].

The unpaired 4f electrons in REEs give them high magnetic moments, which provide high magnetization levels when combined with the high magnetic moments of the transition metal components.

2.3.1.2 Curie Temperature

The Curie temperature (T_c) is the temperature at which the nature of a material undergoes a drastic change in its magnetic properties. Below T_c, magnetic moments are ordered, conferring ferromagnetic properties. Magnetic moments start to realign when the temperature rises to T_c, and magnetic moments become disordered and the spontaneous magnetization disappears transforming the behavior to resemble that of paramagnetic material. Thermal agitation reduces net magnetization by causing the magnetic moments to line up weaker as the temperature rises over the Curie threshold. Therefore, any moments that would align are likely to have their orientations randomized by the higher thermal motion of the atoms [7].

2.3.1.3 Magnetic Anisotropy

The dependency of magnetic energy on the directions of magnetization with respect to the crystal axes is known as magnetic anisotropy [16]. High magnetic anisotropy is necessary for PMs to sustain magnetization in the ideal direction, hence it is an essential factor [7]. Many PM alloys possess an easy magnetization axis (c-axis) perpendicular to the basal plane (a–b plane) and uniaxial crystal structures including hexagonal, tetragonal, and rhombohedral crystals. The RE sublattice contributes significantly to the magnetic anisotropy of RE transition-metal alloys [17].

The simplest expression of magnetic anisotropy for a magnet of volume V is:

$$E_a = K_1 V \sin 2\theta \quad (\textit{Equation 5})$$

This is referred to as lowest-order uniaxial anisotropy, and the initial uniaxial anisotropy constant is K_1, which is commonly utilized to characterize uniaxial magnets. The easy magnetic direction in the case of $K_1>0$ is along the c (or z) axis, which is known as easy axis anisotropy; in the case of $K_1<0$, on the other hand, the easy magnetic direction that can be any location on the a-b (or x-y) plane, which is known as easy-plane anisotropy [16].

The orientation of the magnetic moments and the shape of the hysteresis cycle depend on the magnetic anisotropy, which defines their suitable use in practice.

In ferromagnetic materials, the orientation of the magnetic moments and the shape of the hysteresis cycle depend on the magnetic anisotropy, which determines their applicability for particular applications. In this context, high anisotropy is required for hard magnets while low anisotropy is characteristic for soft magnets [7].

2.3.1.4 Magnetocrystalline Anisotropy

Magnetocrystalline anisotropy reflects how spin-orbit coupling and crystal-field interactions enable magnetic characteristics to depend on crystallographic orientations. The magnetization process differs along distinct crystal axes, producing easy and hard magnetization axes; however, in ferromagnetic materials, magnetocrystalline anisotropy leads to magnetic moments being preferentially oriented with the easy axis, where it is easier to achieve saturation magnetization when an external field is applied [15]. In contrast to easy axes, hard axes need significantly higher fields to achieve saturation, even though the same saturation magnetization can be obtained regardless of the axis. The region between magnetization curves, given in Figure 2.3, indicates the magnetocrystalline anisotropy energy, which is the energy difference per unit volume between magnetization along easy and hard directions.

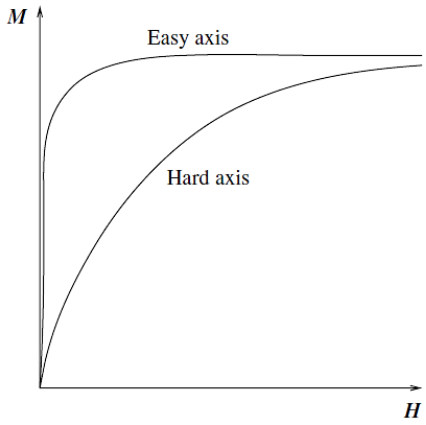

Figure 2.3 Graphical magnetization curves for a ferromagnet where the field is pointed in both the easy and hard directions [9].

The magnetocrystalline anisotropy is significant in the case of RE materials because of the large spin-orbit coupling coming from their heavy atomic structure. In RE materials, overcoming spin-orbit coupling requires a significant amount of energy. This results in a large magnetocrystalline anisotropy, which means that high fields are needed to reverse the magnetization, thus being useful in applications that need high coercive fields [9].

2.3.2 Extrinsic Properties

Extrinsic magnetic properties, including hysteresis loops, coercivity, remanence, and maximum energy product, are highly microstructure-sensitive. Impurities, processing methods, and microstructural features strongly affect the extrinsic properties.

2.3.2.1 Hysteresis Loops

For a better understanding of the extrinsic properties of magnetic materials hysteresis loops are plotted as the graphs of magnetic induction (B) or magnetization (M) in terms of an external magnetic field (H). M-H hysteresis loops (Figure 2.4 (b)) are obtained by plotting the volume-averaged M as a function of H, while B-H loops

(Figure 2.4 (a)) illustrate the flux density B = μ0 H + μ0 M as a function of H. A hysteresis loop demonstrates how a magnetized material begins as an unmagnetized state and progresses along a curve from 0 to saturation (Bs) as the field is increased in a positive direction. B increases since B = H + 4πM, even if the magnetization remains constant following saturation. The saturation induction is defined as the value of B at B_s, and the normal induction curve is the path taken by B from the demagnetized condition to Bs. The induction drops from Bs to the residual induction (Br) when H is decreased to zero following saturation.

Important characteristics of M-H loops include remanent magnetization (M_r), which is the remaining magnetization after the external field is removed, and coercivity (H_c), which is the field required to reduce magnetization to zero. The maximum energy product ((BH)max), which represents the highest magnetostatic energy stored outside the magnet, can be determined with the use of B-H loops. To enhance accuracy, these loops typically are adjusted for the demagnetizing field (DM), which makes the hysteresis loops more

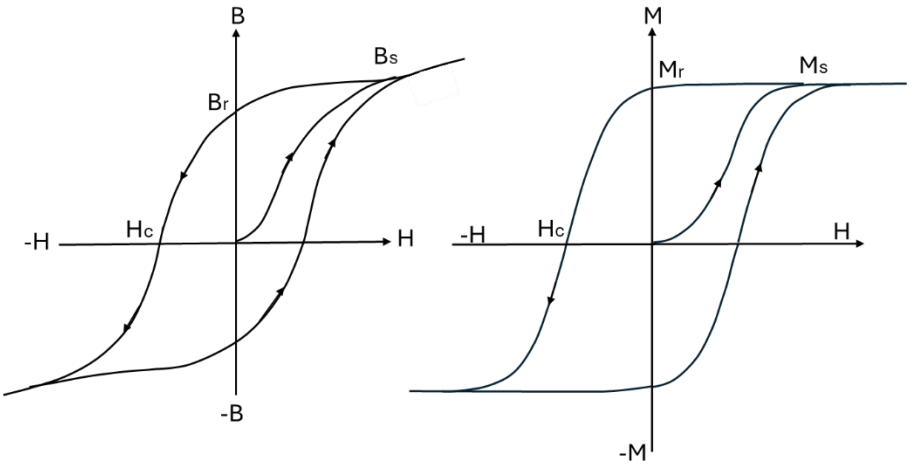

Figure 2.4 Schematic representation of a) B-H and b) M-H hysteresis loops

2.3.2.2 Coercivity

The strength of the external reverse field that is required in the process of demagnetization of the materials until negligible magnetic induction of the ferromagnetic material is referred to as coercivity (H_c). This property defines whether the material is a soft or hard ferromagnetic material. It is therefore clear that while hard magnets and soft magnets differ in many ways, the difference is most apparent in the shape and other characteristics of the loop (see. Figure 2.5) Hard magnetic materials, often known as permanent magnets, are suitable for applications requiring steady, long-lasting magnetic fields because of their high coercivity—which exceeds 10 kA/m (125 Oe) and significant residual magnetism. Conversely, soft magnetic materials are good for applications where magnetic induction varies often due to their low coercivity (less than 1 kA/m (12.5 Oe)) and ease of magnetization and demagnetization with weak fields. In soft magnets, intrinsic coercivity, the field strength at which magnetization is completely neutralized, is frequently in line with H_c; however, in hard magnets, it is much higher, indicating higher resistance to demagnetization [9], [14], [18].

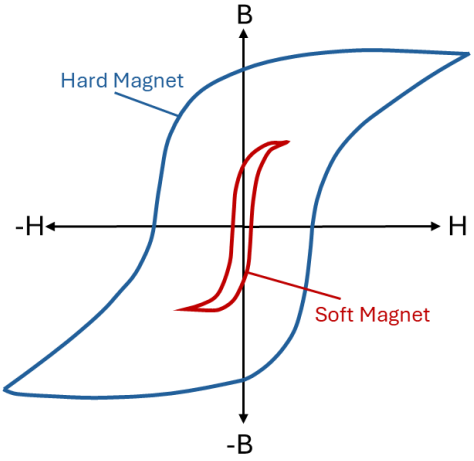

Figure 2.5 Diagrammatic representation of the distinction between soft and hard magnets in a hysteresis loop.

Reducing the grain size under the single domain particle size is a particularly efficient method of increasing coercivity. In this case, interaction domains arise as a result of exchange coupling between neighbouring grains. The domain walls often demonstrate their pinning effect by following the grain boundaries. Thus, coercivity usually rises as grain size decreases with the decoupling of neighbouring grains [19].

2.3.2.3 Remanence

Remanence is the value of the residual induction (B_r) or magnetization (M_r) after the field is removed for a magnetic material that has been magnetized to saturation. It is the highest amount of M_r or B_r that may be obtained without the use of an external field after saturation [18].

A PM has to retain a high level of magnetization when removed from the applied field in order to work as a magnetic field source. High remanence, and consequently high saturation magnetization are therefore essential [14].

2.3.2.4 Maximum Energy Product

The maximum energy product (BH)max of a permanent magnet, representing the highest product of flux density (B) and magnetic field strength (H), measures the maximum useful work a magnet can perform. Stated differently, the energy needed to magnetize and demagnetize the magnet is expressed by (BH)max. It is frequently used to evaluate the performance characteristics of magnets. It offers essential details about the magnet's performance capabilities and is mostly used to assess if magnet materials are suitable for a specific application [12], [14], [20].

The (BH)max, the largest rectangle that can be visually fitted into the second quadrant of the hysteresis loop, is the result of multiplying remanence by coercivity (see. Figure 2.6) [21].

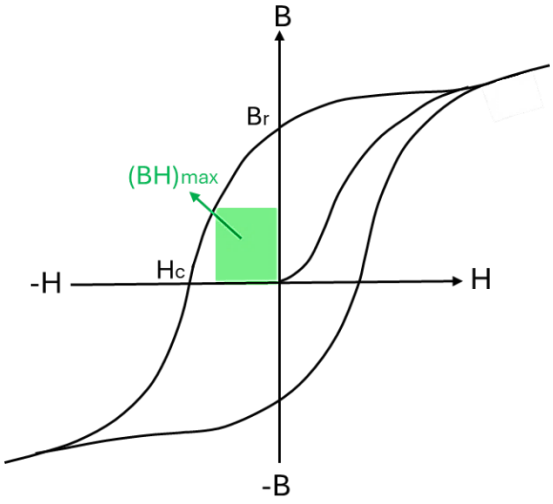

Figure 2.6 Representation of (BH)max in a hysteresis loop.

2.4 Permanent Magnets

Permanent magnets (PMs) are widely used in various fields of transportation, industries, household devices, military applications, and medical technology since they can generate a magnetic force without depending on an electrical supply, PMs, as opposed to electromagnets, generate magnetic flux that requires no ongoing electricity to operate after they are magnetized. They are used in applications that do not require frequent recharging; hence, they have zero operating costs once they have been magnetized. This characteristic places magnets as energy storage products; the energy that is employed in the magnetization of magnets is maintained in reserve and through this, magnets have the ability to apply force in the attraction or the repulsion of other magnetic products. Because PMs can interact with charged particles and conductive materials without making physical contact, the application of permanent magnets is essential to the operation of many devices such as motors, wind turbines, and many electric devices [22], [23], [24], [25]. Figure 2.7 shows different types of devices containing permanent magnets.

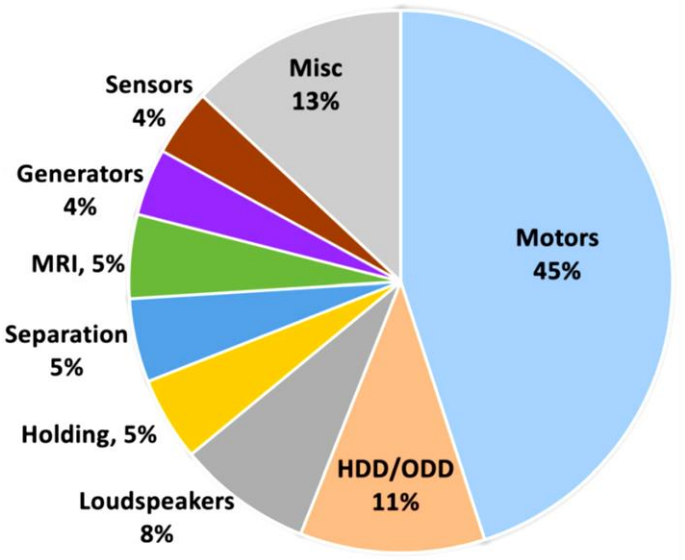

Figure 2.7 Different devices contain permanent magnets [14].

The history of PMs can be traced back to the lodestones when Chinese and Greek mariners first used iron-oxide magnets (ferrite magnets) in compasses. Nevertheless, the insufficient magnetic characteristics of these materials limited their early applications. A major turning point in this field was the discovery of Alnico magnets, which appeared in the 1930s and led to advances in PM studies that lasted until the 1980s.

During this period, there was a notable breakthrough in magnetic energy storage, which is about a 100-fold increase in energy density and a significant improvement in the coercivity of the PMs. A revolution in PM technology began in the 20th century with a series of important discoveries, most notably the invention of novel materials with enough anisotropy to maintain their magnetic properties independent of their shape. The discovery of Sm-Co magnets [26] in the 1960s and Nd-Fe-B magnets in the 1980s directed significant advancement in the research area of magnetism and reinforced the progression of PM technology. These REE-based PMs now produce the magnetic field required for a myriad of practical applications [27], [28], [29].

To describe the chronology of PMs shown in Figure 2.8 the maximum energy product, (BH)max, is used, which is the most commonly used value to rank and compare different magnet families and grades. This value is related to the energy capacity of PMs, as well as the amount of work they can accomplish. Figure 2.8 indicates that the maximum energy product rose by around fifty times between 1917 and 2000. Intrinsic coercivity levels have risen from around 250 Oe (Oersted) to as high as 25,000 Oe throughout the same period, an approximately 100-fold increase [29]. Table 2.1 presents an overview of the intrinsic properties of some PMs.

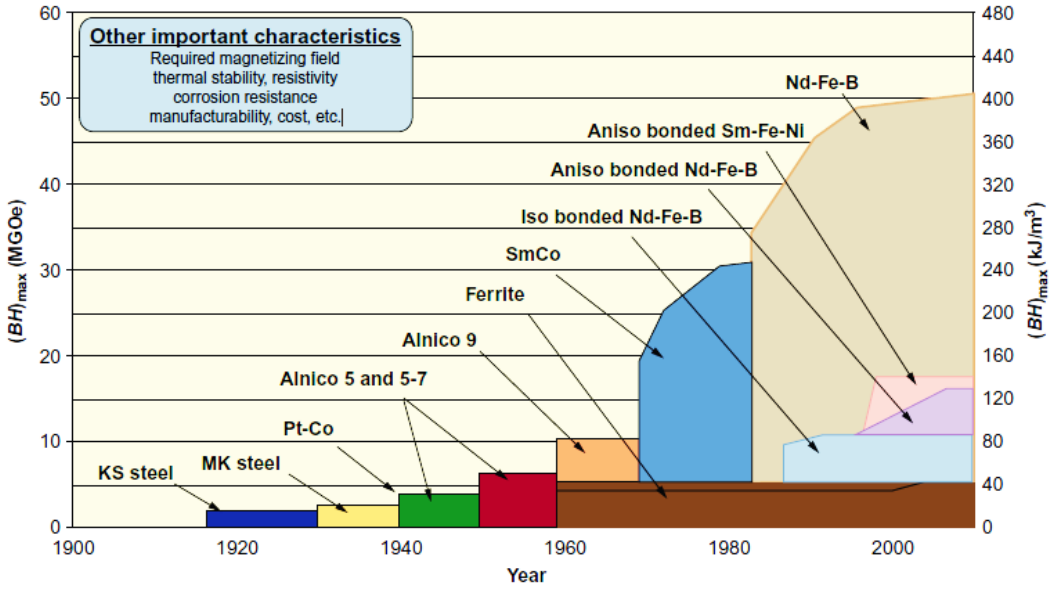

Figure 2.8 Development of the energy product BHmax for commercial permanent magnets during the last few decades at room temperature [30].

Table 2.1 Magnetic properties of some permanent magnets [1].

Material	**T_c (K)**	**M_s (MA m^{-1})**	**K_1 (MJ m^{-3})**	**(BH)max (kJm^{-3})**
Alnico 5	1210	1.12	0.68	310
$SmCo_5$	1020	0.86	17.2	231
Sm_2Co_{17}	838	0.97	4.2	294
$Nd_2Fe_{14}B$	588	1.28	4.9	512

Magnetically isotropic and magnetically anisotropic PMs are the two different kinds that fall under each of these families [31]. Depending on the manufacturing method of PMs, the final product can be isotropic or anisotropic magnets.

Isotropic magnetic materials have the crystallographic axes randomly oriented in each grain, and hence, the magnetic properties are independent of the direction. One example is the NdFeB magnetic powder prepared by melt spinning, which has the characteristic of a nanocrystalline microstructure and has random orientation of the magnetic moments because of rapid quenching of the melt. Besides, isotropic properties are observed in compression and injection molding of magnets in which particles are not aligned. An illustration of an isotropic magnet is presented in Figure 2.9 (a). However, it must be noted that sometimes, usual diagrams regarding isotropic magnets may give an impression that they are planar, while, in reality, crystallographic axes are randomly situated in three-dimensional space. Among the most commercially available PM materials include anisotropic magnets: $SmCo_5$; $Sm_2(Co, Fe, Cu, Zr)_{17}$; sintered NdFeB, and sintered ferrites. Their microstructure comprises a preferred orientation where all grain's crystallographic axes are nearly parallel to the easy axis through a magnetic field that also increases the directional magnetic characteristics. Furthermore, it is also suitable for anisotropic bonded magnets, which include SmFeN anisotropic powder, crushed hot-deformed NdFeB powder, and anisotropic hydrogenation-disproportionation-desorption-recombination (HDDR) powders to enhance performance by maintaining this alignment. An illustration of an isotropic magnet is presented in Figure 2.9 (b) [31].

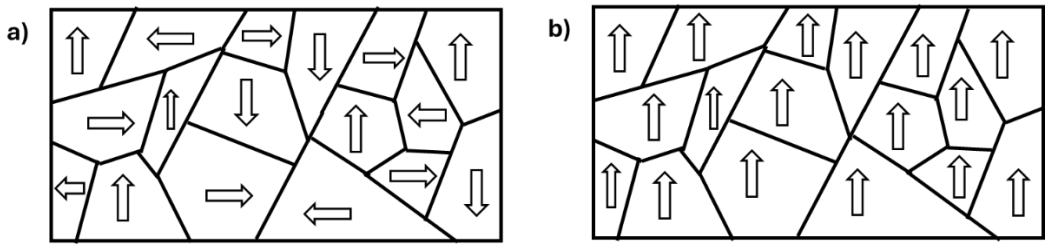

Figure 2.9 Illustration of a) an isotropic magnetic material with randomly aligned crystallographic axes of different grains, b) anisotropic magnetic material with parallel aligned crystallographic axes of different grains.

2.4.1 Overview of NdFeB Magnets

REE-based PMs, which were first discovered in the mid-1960s [26], controlled the market throughout the 1970s. Due to the relatively high cost of both Sm and Co, the search began for a less expensive and high-performance iron-based REE magnet [29]. After numerous studies, a sufficient new magnetic material was finally discovered with the development of neodymium-iron-boron magnets ($Nd_2Fe_{14}B$). In early 1982, the $Nd_2Fe_{14}B$ magnet was found almost simultaneously by two different research groups: General Motors Research Laboratories (GMRL) [32] and the Sumitomo Special Metals Corporation [33]. Sumitomo's discovery was based on the search for ternary R-Fe-X intermetallic compounds and adapted the powder metallurgical method that was used in the production of Sm-Co PMs; the General Motors discovery was the result of efforts to create metastable intermetallic compounds from rapidly solidifying rare earth-iron materials [29]. This novel material $Nd_2Fe_{14}B$ has a tetragonal structure of space group P42/nmn [34], [35], [36] and had an energy product that peaked in 1984. Each unit cell of the $Nd_2Fe_{14}B$ phase is made up of 4 formula units, or 68 atoms. In the crystal structure, there are two REE locations, f and g, six non-equivalent iron sites, j_1, j_2, k_1, k_2, c, and e, and 1 boron site, g. The tetragonal unit cell of Nd2Fe14B is shown in Figure 2.10.

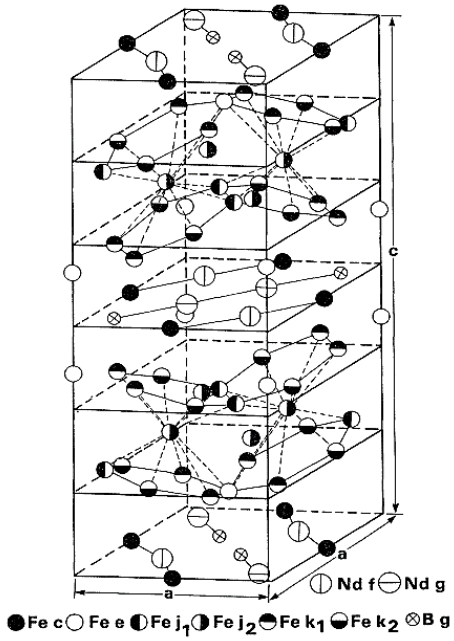

Figure 2.10 The tetragonal unit cell of $Nd_2Fe_{14}B$ [37].

NdFeB magnets have been preferred in many advanced technological products since the day they were first produced. The production of sintered NdFeB magnets has rapidly been used in electronics, automotive applications, medical instruments, wind turbines, computer components, communications, and many more due to high magnetic performance and cost-efficiency as compared to other magnet types.

Total production of electric motors and related applications using NdFeB magnets increased up to nearly 1000 metric tonnes especially improved by interior permanent magnet (IPM) motors that improve the energy ratio of air conditioner compressors and motors of hybrid cars. Growing environmental concerns, which have led to increased demand for electric and hybrid vehicles, e.g., the Toyota Prius that consumes more than 2 kg of NdFeB, are predicted to drive increased demand for high-performance PMs, thus accelerating their growth in this sector [38], [39].

2.4.1.1 The NdFeB Ternay Sytem

Studies on the NdFeB interaction have resulted in the obtainment of ternary phase diagrams [33], [40], [41].

The NdFeB ternary system mainly consisted of 3 regions: a matrix phase of $Nd_2Fe_{14}B$ (T1), a secondary phase of $Nd_{1+\varepsilon}Fe_4B_4$ (or $R_{1+\varepsilon}Fe_4B_4$ or B-rich) (T2), which ε changes with REEs, and a ternary eutectic at the grain boundaries that included some Nd-rich phase (T3). Other frequently used designations for T1, T2, and T3 are ϕ, η, and ρ, respectively [42].

The liquidus curves for ternary phases are displayed in Figure 2.11 and the reactions at monovariant and invariant points are listed in Table 2.2. According to the NdFeB ternary phase diagram, the $Nd_2Fe_{14}B$ phase crystallizes at the region with the highest iron content: the first to crystallize in this region is the Fe phase, as also seen in the vertical section in Figure 2.12. In a peritectic reaction involving liquid and iron ($L + Fe \rightarrow Nd_2Fe_{14}B$) (marked as p5 in Figure 2.11), the primary phase generated is the $Nd_2Fe_{14}B$ phase. If the cast structure includes αFe + $Nd_2Fe_{14}B$ + Nd-rich eutectic phase, this is due to the incomplete peritectic reaction. The formation of the magnetically soft α-Fe phase, which was transformed from γ-Fe, greatly affects the magnetic properties negatively; therefore, there is a need for excess B and Nd to prevent it.

Two techniques have been applied to suppress the peritectic reaction: undercooling the melt considerably below the peritectic temperature and rapidly cooling the melt more rapidly than the properitectic phase nucleation. From further heat treatment at a temperature lower than that of the peritectic temperature, $Nd_2Fe_{14}B$ and $Nd_{1+\varepsilon}Fe_4B_4$, as well as the liquid phase having a composition that is relatively high in B and Nd, would be at equilibrium with each other.

$Nd_2Fe_{14}B$, $Nd_{1+\varepsilon}Fe_4B_4$, and a liquid phase with a composition comparatively high in B and Nd would be in equilibrium with each other following further heat treatment at a temperature lower than the peritectic temperature. Subsequent cooling after the

heat treatment leads to increased saturation with $Nd_2Fe_{14}B$ and $Nd_{1+\varepsilon}Fe_4B_4$ and shifting the position of the liquid phase composition through the monovariant curve e_5E_2, with the liquid phase being consumed at the ternary eutectic at the Nd-rich corner of the phase diagram (designated as E_2 in Figure 2.12). Below the ternary eutectic temperature, the liquid phase solidifies to provide three phases of $Nd_2Fe_{14}B$, $Nd_{1+\varepsilon}Fe_4B_4$, and Nd [40], [43].

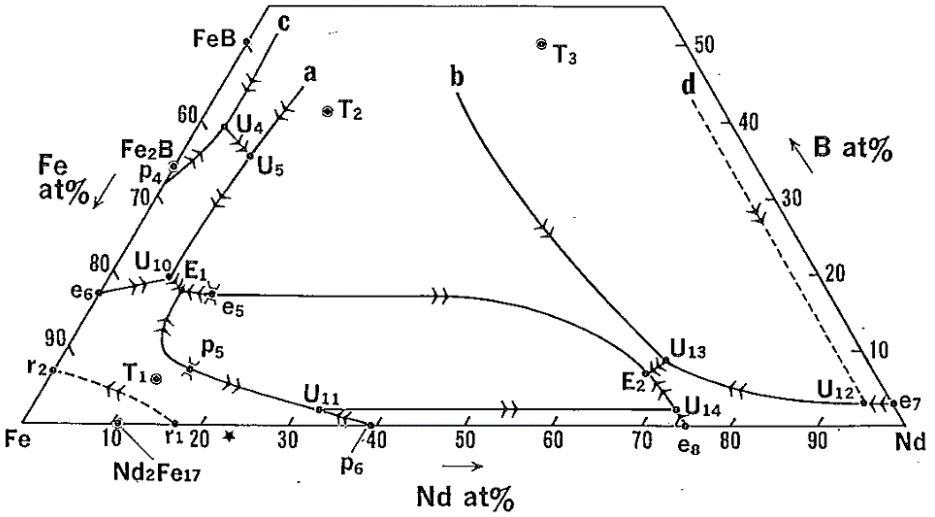

Figure 2.11 The liquid phase projection of the NdFeB ternary system, where U = transition, p = peritectic, e = eutectic, and E = ternary eutectic [44]

Table 2.2 Invariant and monovariant reactions for the NdFeB ternary system [41].

Symbol	Type of Invariant Reaction	Reaction	Composition (at%) Nd	Fe	B	Temperature (K)
p_4	peritectic	L+FeB↔Fe_2B	-	68	32	1680
p_5	peritectic	L+γ-Fe↔T1	14	79	7	1428
p_6	peritectic	L+γ-Fe↔Nd_2Fe_{17}	39	61	-	1458
r_1	remelting	δ↔γ-Fe+L	17	83	-	1665
r_2	remelting	δ↔γ-Fe+L	-	93	7	1654
e_5	eutectic	L↔T1+T2	12	71	17	1368
e_6	eutectic	L↔γ-Fe+Fe2B	-	83	17	1450
e_7	eutectic	L↔Nd+Nd_2B_5	97	-	3	1275
e_8	eutectic	L↔Nd+Nd_2Fe_{17}	75	25	-	913
U_4	transition	L+FeB↔NdB_4+Fe_2B	3	58	39	
U_5	transition	L+NdB_4↔Fe_2B+T_2	6	57	37	
U_{10}	transition	L+Fe_2B↔T2+γ-Fe	7	74	19	1403
U_{11}	transition	L+γ-Fe↔Nd_2Fe_{17}+T1	32	66	2	
U_{12}	transition	L+Nd_2B_5↔T3+Nd	94	3	3	1393
U_{13}	transition	L+T3↔Nd+T2	68	24	8	
U_{14}	transition	L+ Nd_2Fe_{17}↔T1+Nd	73	25	2	958
E_1	ternary eutectic	L↔γ-Fe+T1+T2	8	74	18	1363
E_2	ternary eutectic	L↔Nd+T1+T2	67	26	7	938

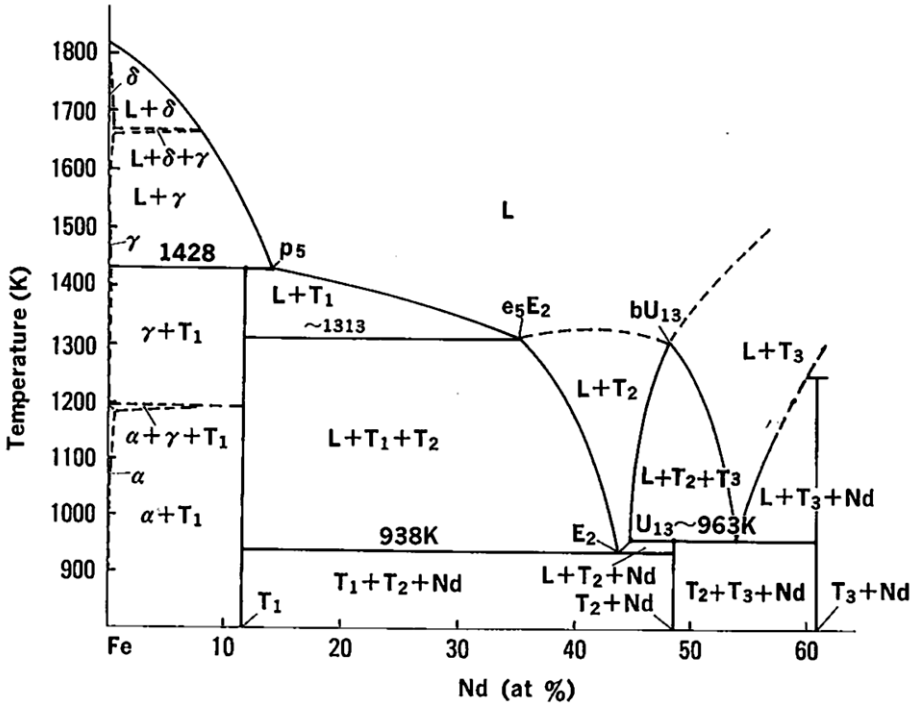

Figure 2.12 Binary phase diagram of the NdFeB alloy [44]

2.5 Production of NdFeB Magnets

NdFeB-based magnets can be manufactured using a variety of production methods depending on their intended application. Sintering and polymer bonding are two common techniques used for manufacturing bulk NdFeB magnets. Anisotropic sintered magnets with high performance are made using powder metallurgy. Sintered NdFeB magnets have outstanding magnetic characteristics when compared to bonded NdFeB magnets. As seen in Figure 2.13, sintered NdFeB magnets possess the highest (BH)max, which makes sintered NdFeB magnets the most affordable PMs to date. However, although they have outstanding magnetic properties, they have some drawbacks including limited corrosion resistance, insufficient coercivity, and average high-temperature characteristics. Although these shortcomings are partially due to the intrinsic properties of materials, their microstructural characteristics also have a significant influence on magnetic properties [38], [45].

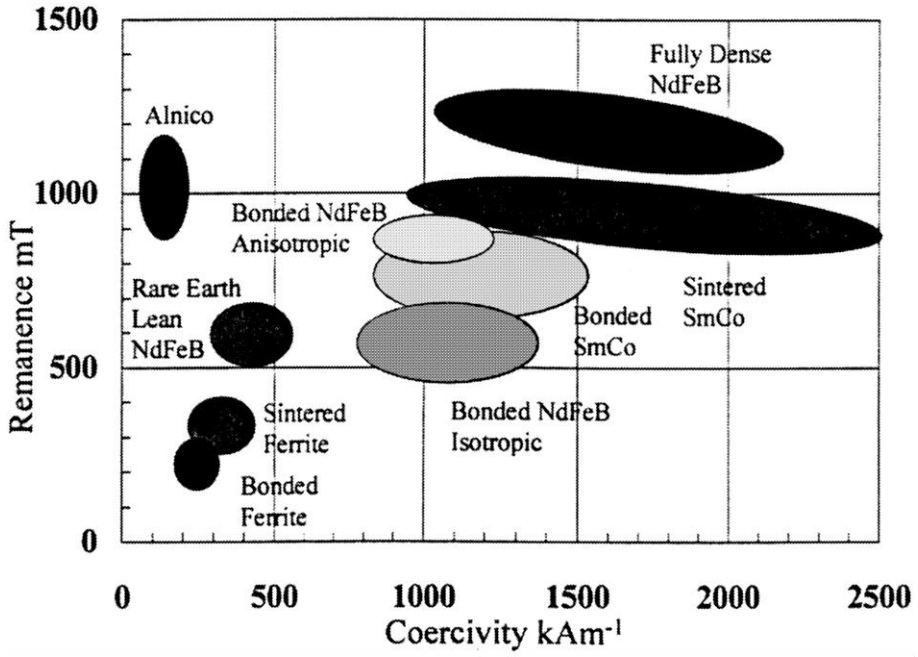

Figure 2.13 Representation of magnetic properties of the permanent magnets [38].

The manufacturing procedure of sintered NdFeB magnets involves the following steps: alloy preparation, composition modification, milling, pressing, aligning particles, sintering, and heat treatment, followed by machining and magnetizing [33].

During alloying preparation, alloying elements are often used to improve the microstructure and magnetic properties of the NdFeB alloy. Heavy rare earth elements (HREEs) such as Dy and Tb are presently partially substituted for Nd to enhance coercivity and stability at higher temperatures and are useful in enhancing the 2:14:1 phase anisotropy field [34], [46], [47], [48]. This strategy's drawbacks include a decrease in energy density [34], [47]. Many additive elements, including Cu, Co, Al, Pr, Nb, Ho, Gd, and more, are utilized in addition to Dy and Tb for the following purposes [38]:

- development of corrosion resistance,
- raising the Curie temperature (for $Nd_2Fe_{14}B$, it is merely 583 K),
- enhancing grain boundary wetting to promote sintering as well as avoid reverse domain nucleation.

Determining the precise quantity of Nd during alloy preparation is essential. It is generally accepted that the magnetocrystalline anisotropy of the main $Nd_2Fe_{14}B$ phases is the primary source of coercivity in Nd-Fe-B magnets. However microstructural elements, such as the distribution and composition of Nd-rich phases at the grain boundary, also have a significant impact on it. In addition to their important function in densification, the Nd-rich phases facilitate grain sliding and offer channels for atom diffusion, resulting in a c-axis texture [49].

Vacuum induction melting is frequently used in alloy preparation. In alumina crucibles, Fe and B are first melted in a pure argon environment before being degassed under a vacuum. The melt, which is kept at a temperature slightly higher than the Fe-B liquidus temperature, follows by adding Nd. An essential factor in the manufacturing of sintered magnets is the microstructure of the starting alloy. The formation of $Nd_2Fe_{14}B$ through a peritectic reaction presents challenges, as normal cooling rates frequently result in a mixture of $Nd_2Fe_{14}B$, $NdFe_4B_4$, and ductile α-Fe. The presence of ductile α-Fe complicates powder production and reduces the magnetic performance of sintered magnets. Extended high-temperature annealing is required to remove these secondary phases, which is expensive and time-consuming. The melt is cooled rapidly to prevent oxidation and α-Fe formation during casting [22], [40]. Although the rapid cooling method helped to prevent the formation of α-Fe, it was not a complete solution. The challenge of producing high-quality NdFeB alloys was overcome through the development of strip-casting [22]. A schematic illustration of typical manufacturing steps of NdFeB alloy is shown in Figure 2.14.

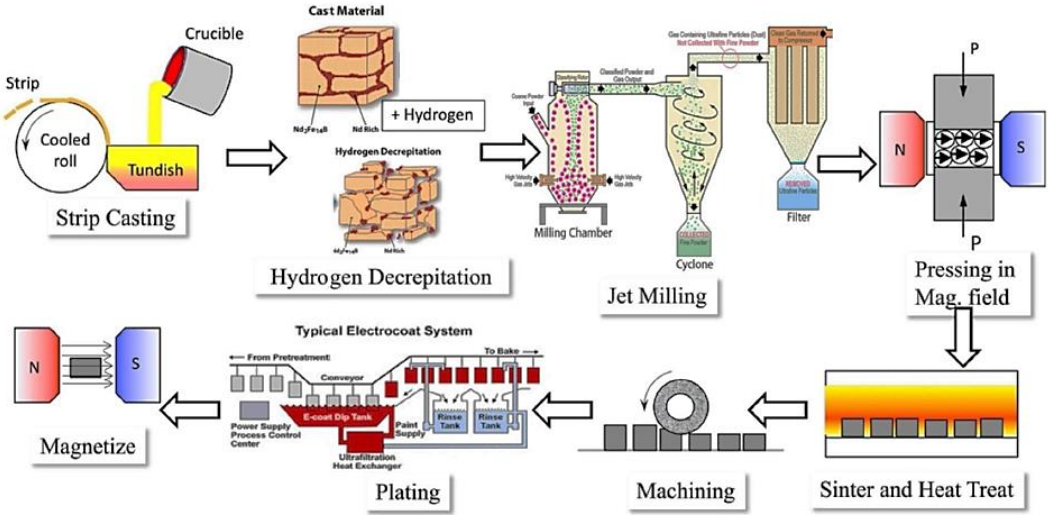

Figure 2.14 A schematic illustration of typical manufacturing steps of NdFeB alloy [22].

A significant advancement in NdFeB magnet production was the replacement of mechanical crushing with the hydrogen decrepitation (HD) process [50]. Internal stress resulting within the NdFeB material from hydrogen embrittlement, which is brought on by hydrogen penetrating grain boundaries, leads to microcrack propagation and the formation of friable flakes. As shown in Figure 2.15, compared to mechanically crushed materials, the average particle size of HD powder is far less reliant on the powder input rate, allowing for much higher processing efficiency in the following milling stages. This method is now the industry standard, reducing production costs by approximately 25% [12], [22]. (The HD process is described in more detail in the following sections.)

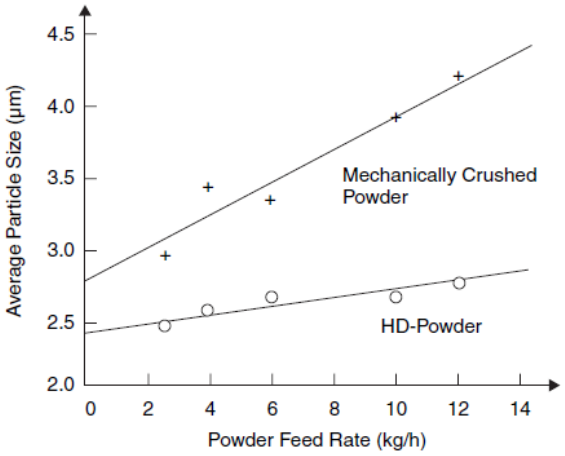

Figure 2.15 Mean size of particles compared to the powder input rate to the jet mill [12].

Another way to produce NdFeB magnet powders is the hydrogenation-decomposition-desorption-recombination (HDDR) process. The HDDR method involves four transformations of hydrogen-absorbing intermetallic compounds in a hydrogen environment. $Nd_2Fe_{14}B$ first forms $Nd_2Fe_{14}BH_x$ by absorbing hydrogen at 300 °C. Then, at higher temperatures, this compound decomposes into NdH_y hydride, Fe_2B, and Fe. Under vacuum, NdH_y desorbs hydrogen and recombines with Fe_2B and Fe to regenerate $Nd_2Fe_{14}B$. This process typically carried out under vacuum, produces fine crystalline microstructures and metastable phases, assists in the commercial production of NdFeB anisotropic magnet powders [51].

After the HD process, for further milling process, jet mills under an inert atmosphere, planetary ball milling systems, and high-energy milling systems can be used. The ultrafine particles are successfully removed by further jet milling, which reduces the particle size distribution to around 5 μm and produces a powder primarily composed of single-crystal particles [22]. In studies using ball milling systems [52] or high-energy ball milling systems [53], [54], [55], [56], [57], inert gases as well as liquid media are frequently used as milling media. The parameters of ball milling affect the size distribution, shape, and properties of the resulting powder. In wet milling, an organic liquid is used alone or in combination with solvents, e.g. toluene, heptane, etc., and surfactants, e.g. oleic acid (OA), oleylamine (OY), etc. OA and OY are

more efficient than other surfactants in preventing the agglomeration of particles or flakes. They also prevent the milled powders from turning into an amorphous structure [54].

After milling, the aligned powder is pressed and sintered under vacuum or in inert gas atmospheres, removing residual hydrogen and producing a dense, fine-grained microstructure. The sintering process is generally applied in the temperature range of 1080 °C - 1120 °C [58], [59], [60]. The density of $Nd_2Fe_{14}B$ is 7.69 $g \cdot cm^{-3}$ and typically needs to exceed 98% of the theoretical density. To achieve optimal coercivity and hysteresis loop properties, an isothermal heat treatment is also required [13], [22].

The volume of the pressed product decreases to the final magnet body during the sintering process. The ultimate size and form of the magnet as well as production conditions influence its shrinking. A machining procedure is consequently required since this leads to some variation in the size of the magnet.

Most applications necessitate a protective coating because $Nd_2Fe_{14}B$ magnets are prone to corrosion. This vulnerability is mainly caused by the microstructure, which is composed of 2:14:1 grain bound by a thin, highly reactive Nd-rich grain boundary phase. One major aspect affecting the final magnetic characteristics is the concentration of oxygen. Humid environments lead to grain boundary degradation, weakening intergranular bonding, and releasing corrosion products. Neodymium oxide (mainly Nd_2O_3) formation at the grain boundary in the presence of oxygen can reduce the coercivity [21]. According to the studies conducted by Kim et al. [61] and Minowa et al. [62] an average oxygen content of 0.7 wt% falls into the range identified. Even though corrosion resistance has improved due to developments in alloy chemistry, processing, and microstructure, a protective coating is still essential. Optimal coatings are thin, uniform, and applied using hydrogen-free methods across a variety of shapes and sizes; common coatings include electroless nickel, Ni-Cu-Ni, epoxy, aluminum, zinc, etc. [22], [63]. Finally, the coated magnets undergo magnetization in a high magnetic field.

2.5.1 Effect of Particle Size Distribution on Microstructure and Magnetic Properties

The microstructure and magnetic properties of sintered NdFeB magnets are significantly influenced by particle size distribution, which affects (BH)max, remanence, and coercivity. A configuration where the paramagnetic Nd-rich phase surrounds the $Nd_2Fe_{14}B$ grains and the average grain size of the main phase $Nd_2Fe_{14}B$ is small is required to produce magnets with high H_c and Br values. The high density of the material is dependent on the liquid Nd-rich phase that occurs during sintering. The $Nd_2Fe_{14}B$ grains are decoupled by the Nd-rich phase in high-quality magnets based on the exchange interaction. Therefore, nucleation of reverse domains must occur in each grain during a demagnetization process [64].

Coercivity in NdFeB magnets is governed by the nucleation of reverse magnetic domains at the grain boundaries of $Nd_2Fe_{14}B$. The coercivity of sintered magnets often exhibits an opposite grain-size dependency because smaller grain sizes decrease the possibility of reverse domain nucleation at the grain boundaries and local demagnetizing stray fields. In other words, as particle size reduces, the coercivity of sintered magnets usually improves. Nevertheless, small particles can result in abnormal grain growth during liquid phase sintering, which is caused by thermally activated processes that create large grains to minimize surface energy. This growth negatively affects coercivity by disrupting the grain boundary isolation needed to decouple $Nd_2Fe_{14}B$ grains, thus diminishing magnetic performance [65]. There have been some published articles about the relationship between coercivity and particle size. Using powder metallurgy, Scott et al. [66] created sintered NdFeB magnets utilizing powders with typical particle sizes ranging from 2.5 to 4.2 μm. The study examined how the average grain size and properties of sintered magnets are affected by particle size and oxygen concentration. Magnets from 4.2 μm particles demonstrated constant coercivity despite oxygen variations, but those from smaller powders exhibited decreasing coercivity with increasing oxygen levels. Li et al. [67] investigated how grain size affected the coercivity of NdFeB sintered

magnets and observed that the coercivity decreased below an average grain size of 4.5 μm (particle size of 3 μm), with the maximum coercivity being achieved at this particle size. In addition, the result shows that the area ratio of the Nd phase decreased from 58% of the total area of the Nd-rich phase for a grain size of 4.5 μm to 27% for 3 μm, while the NdO_x phase increased from 2.9% to 9.3%. This suggests that the NdOx fraction is enhanced at the loss of Nd when finer particles absorb more oxygen. Since an interconnected network structure forms, resulting higher NdOx volume percentage makes it more difficult for a continuous thin grain boundary phase to occur, which leads to a loss of coercivity.

Remanence is determined by factors such as magnetic volume, density, and grain alignment, all of which are influenced by particle size. An ideal range of particle sizes (D10 to D90) exists that maximizes grain alignment and enhances magnetic properties. However, excessively fine powders can lead to decreased orientation of grains as smaller particles do not possess adequate torque to overcome inter-particle friction, thereby negatively impacting remanence [65].

In previous studies, jet mill powders of different sizes have been used, e.g. Davies et al. [38] used 6 μm, Kim et al. [68] used 5 μm, Guo et al. [69] used 3.6 μm, Cui et al. [70] used 3.3 μm. According to studies, the ideal powder size range for NdFeB powders is 3-6 μm. To improve the magnetic properties of NdFeB magnets, jet-milled powder particle size classification and optimization are important. It is possible to increase the remanence and maximum energy product by eliminating extremely fine or coarse particles. While coarse powders inhibit densification, excessively fine powders create difficulties with grain growth. Maintaining the ideal grain size is crucial for obtaining optimum coercivity and remanence values. Improved magnetic properties depend on high material density as well as effective grain isolation, which is made possible by the Nd-rich phase surrounding $Nd_2Fe_{14}B$ grains. Consequently, in order to achieve the desired magnetic performance in NdFeB sintered magnets, controlling the particle size distribution is essential [65].

2.6 Recycling of NdFeB Magnets

NdFeB magnets are important for high-technology applications and clean energy, including electric vehicles, hard disk drives (HDDs), wind turbines, etc. However, due to their reliance on REEs, mostly imported from China, which dominates the REE market, imposes export restrictions, and causes price volatility, these magnets face supply problems. This has brought attention to the possibility of Nd, Pr, and Dy supply shortages. Therefore, the availability issue is a major concern to many countries. Opening rare earth mines outside of China, utilizing alternative technologies, lowering the amount of rare earth in applications, and recycling already-existing NdFeB magnets are some strategies for addressing these shortages. Nevertheless, mining is energy-intensive and harmful to the environment, alternatives can decrease efficiency, and current technology can't replace rare earths entirely without sacrificing performance. To improve the sustainable supply of NdFeB magnets, it is important to implement effective recycling procedures [71].

The recycling of the magnets from End-of-life (EOL) products has the potential to serve as a sustainable secondary supply source for NdFeB magnets. Recycling NdFeB magnets presents a viable strategy to mitigate these issues. Although recycling is expected, today, less than 1% of REEs are recycled due to various difficulties in collection and sorting as well as purification from electronic waste. Since NdFeB magnets have different lifetimes depending on how they are used, it dictates their chances of being reused. Even though some NdFeB magnets are recycled, efficient economically viable technologies are absent when it comes to small electronics products. The existing recycling technique is still in the research and development stage, and it is expected to be a significant driver for recycled REEs regarding magnet sector demand in the future, especially by 2030. However, there are still problems in terms of contemporary feasibility and cost effectiveness which are mainly attributed to issues of processing as well as low concentration of magnetic materials found in e-waste. In general, effective chains of recycling these products

are critical for the provision of more sustainable sources of REEs, meeting the supply-demand crises and environmental concerns [71], [72], [73].

NdFeB magnet recycling at different technology-readiness levels (TRLs) can be done through a variety of metallurgical processes, including liquid metal extraction, oxidation or chlorination, hydrometallurgical processing, and pyrometallurgical slag extraction, electrolysis in molten salts, and hydrogen decrepitation [73], [74]. NdFeB recycling involves various approaches, including direct reuse, waste-to-REE, waste-to-alloy, and magnet-to-magnet (MtM) methods. The MtM route has the benefit of requiring fewer processing steps compared to conventional production, leading to lower energy and chemical consumption, minimal waste generation, reduced emissions, and improved magnetic performance. It provides a closed-loop recycling concept for commercial use and is especially well-suited for HDDs. However, challenges such as its inapplicability to mixed scrap feeds and oxidized magnets, as well as potential material losses, must be addressed. All things considered, the MtM recycling method offers an effective and sustainable solution for NdFeB magnets that are getting close to commercial viability [75].

2.6.1 Hydrogen Decrepitation Process

The basis of hydrogen decrepitation (HD) is the selective synthesis of neodymium hydrides via the chemical reaction of hydrogen gas with Nd present in the NdFeB magnet. A schematic drawing of the HD process is given in Figure 2.16. Large amounts of hydrogen gas can be reversibly absorbed by $Nd_2Fe_{14}B$ alloys. The process of hydrogen absorption is divided into two phases. The HD process is first initiated at the Nd-rich grain boundaries at room temperature and ambient pressure and involves the formation of NdH_x. The hydrogenation of the Nd-rich grain boundary phase can induce a volume increase of up to 16%, resulting in stresses that primarily promote crack propagation along grain boundaries. This exothermic process is followed by the formation of a hydrogen solution inside the $Nd_2Fe_{14}B$ matrix phase, resulting in differential expansion and subsequent inter- and

transgranular fracture, eventually resulting in the efficient decrepitation of the material. The entire magnet expands and becomes brittle, allowing it to crumble and produce a partly demagnetized hydrogenated powder [13], [74], [76], [77] The exothermic absorption of hydrogen from the Nd-rich phase and the $Nd_2Fe_{14}B$ matrix phase is represented by Equation 6 and Equation 7, respectively, where x and y depend on temperature and pressure [78].

$$Nd + \frac{x}{2} H_2 = NdH_x \qquad (Equation\ 6)$$

$$Nd_2Fe_{14}B + \frac{y}{2} H_2 = Nd_2Fe_{14}BH_y \qquad (Equation\ 7).$$

This exothermic absorption can occur at room temperature and nearly 1 bar of hydrogen pressure [79], and the most stable phase is NdH_2 among neodymium hydride phases [21]. However, according to Onal et al. [80] and Habibzadeh et al. [81], upon hydrogenation at room temperature, no observable NdH_x is present; its formation occurs at higher temperatures. In addition, the formation of the hydride phase inhibits oxidation of the structure, creating a more stable structure [81].

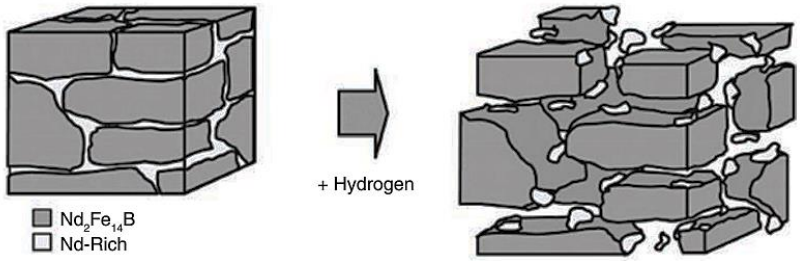

Figure 2.16 Schematic drawing of the HD process of NdFeB magnet [82] .

Different fracture types arising during the HD process are depicted in Figure 2.17. Although intergranular cracking is the predominant mode (Figure 2.17 (c)) throughout the HD process, transgranular cracking also happens (Figure 2.17 (b)). The degree of anisotropy in the final powder may be decreased if some particles have several grains due to incomplete intergranular fracture propagation along all grain boundary phases (Figure 2.17 (d)) [76].

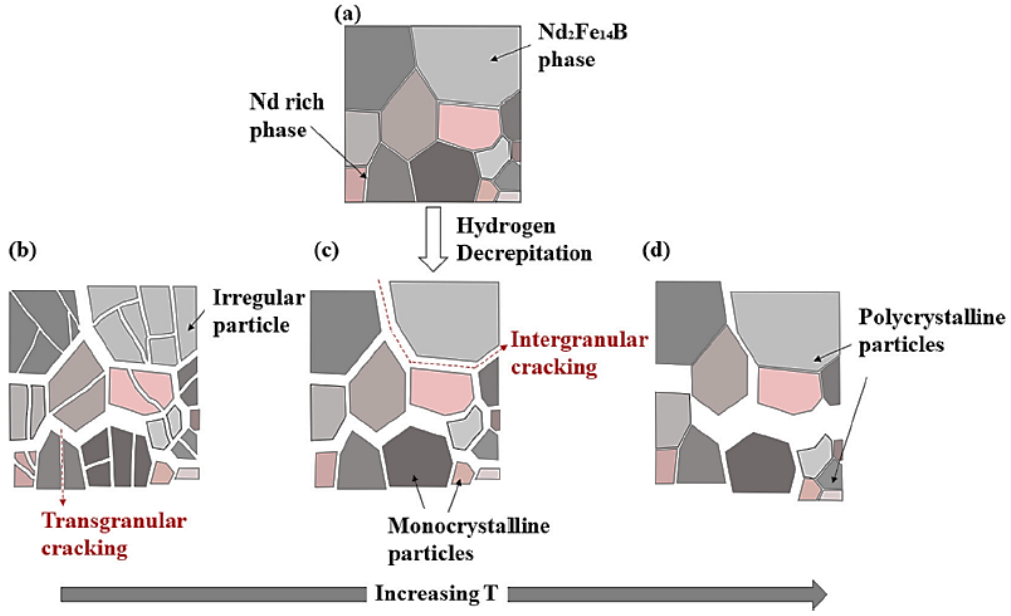

Figure 2.17 Diagrammatic illustration of the various fracture forms that may arise during the HD process: a) starting sample, b) intergranular and transgranular cracking c) entirely intergranular cracking, d) inadequate intergranular cracking [76].

The NdFeB magnet phases have widely differing particle sizes; based on the hydrogen cycle conditions, the matrix phase can range from 10 to 500 μm, while the grain boundary phase is usually smaller than 2 μm [83]. Furthermore, significant advantages are provided by the HD method for preparing bulk alloys to produce sintered magnets. This method overcomes the toughness related to free iron, making it easier to turn large alloy particles into fine powder. The HD process enables the production of single-crystal particles with clean surfaces appropriate for sintering or bonding later by encouraging intergranular failure. Additionally, the HD process reduces oxygen pick-up during milling since the treated material is less oxidizable and offers a non-oxidizing sintering process because of hydrogen desorption. Despite improving mechanical strength and coercivities by reducing grain sizes in the sintered magnets, this also makes it possible to manipulate the HD process parameters to better manage particle size, shape, and distribution [12], [13], [50].

The microcracks in the particles are responsible for the friability obtained during the HD process, as mentioned before. These microcracks enable c-axis alignment in a

magnetic field even when the powder continues to be hydrogenated, allowing to production of fully aligned green compacts. These green compacts are different from standard powders because they do not exhibit coercivity at all as there is a large drop in coercivity due to hydrogen absorption that modifies the Nd-rich phase. This makes handling easier because the green compacts have almost no remanent magnetization.

In order to promote hydrogen desorption, the green compacts are sintered in a vacuum. This process typically takes place in two phases, at around 200 °C and 600 °C, showing that hydrogen evaporates from both the Nd-rich grain boundaries and the $Nd_2Fe_{14}B$ matrix (see. Figure 2.18). The magnets regain considerable coercivity only when all hydrogen is vacated from the particles in the course of sintering, However, multi-crystallines have low coercivity which may be caused by the production of free iron at the boundaries of the grains during the hydrogenation reaction thereby explaining the reason behind lower-than-normal coercivity in HD green compacts [84].

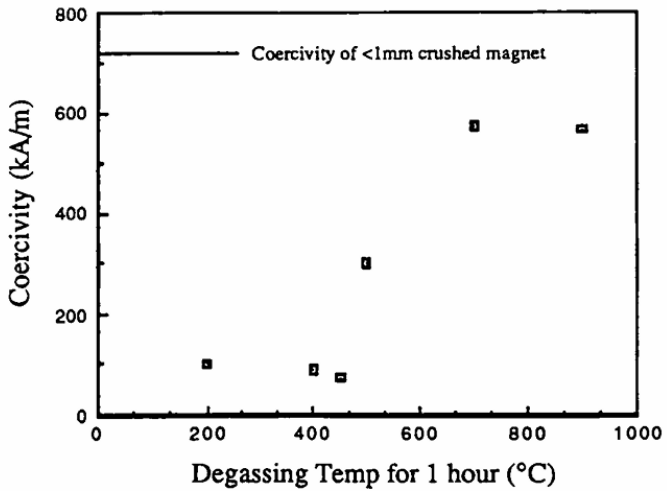

Figure 2.18 Variation in coercivity with degassing temperature of HD powder of sintered material [84].

The primary phase, $Nd_2Fe_{14}BH_x$, must be allowed sufficient time to desorb hydrogen before being elevated to a higher temperature ($T \geq 600$ °C) to enable desirable permanent magnetic characteristics. If the hydrogen desorption is not complete, the

ternary hydride, $Nd_2Fe_{14}BH_x$, will be disproportioned into the binary Nd hydride, Fe, and Fe_2B. While the Nd hydride desorbs H_2 gas, forming Nd metal, at above 600 °C, the coercivity will remain unaffected. Nevertheless, the precipitation of Fe and Fe_2B in the main phase can prevent the improvement of large coercivity by forming domain wall nucleation centers. However, it is normally expected that when the precipitates are reduced to a certain size, they will dissolve in Nd metal to form $Nd_2Fe_{14}B$, which eventually gets dissolved as sintering proceeds [13].

X-ray and neutron diffraction studies [85] reveal that the insertion of hydrogen into the $Nd_2Fe_{14}B$ crystal structure does not alter its lattice symmetry, maintaining a space group of P42/mnm. However, as the hydrogen atoms occupy the interstitial sites, such as 8j, 16k, and 4e, hydrogen insertion significantly expands the unit cell volume between 4 and 6%, [86], [87]. On the other hand, at higher hydrogen content, the cell expansion rate can be reduced, meaning a saturation of the interstitial site. More surprisingly, the saturation magnetization Ms increases when the hydride of $Nd_2Fe_{14}B$ is formed. The increased volume of the unit cell appears to be the reason for this. In particular, the shortest Fe-Fe bond distances are observed to significantly increase with hydrogen, increasing exchange interactions and potentially raising the Curie temperature. Moreover, it has been observed that during the HD process, the amount of H_2 absorbed has a tendency to greatly reduce the anisotropy field of the $Nd_2Fe_{14}B$ phase, having a direct impact on the decrease of the coercivity and also significantly reducing the (BH)max [88], [89]. According to earlier research, hydrogen insertion significantly decreases uniaxial magnetic anisotropy by around 70% [90].

The HD process facilitates the recovery of hard magnetic powder from devices such as hard disk drives (HDDs), electric motors, actuators, wind turbines, and generators for the MtM process. Hydrogen effectively degrades the sintered Nd-Fe-B magnets in these devices, but coated magnets may need partial coating removal to allow hydrogen absorption. The stress arising during the HD process can help the coating to separate and disintegrate. Efficient separation of the coating is important to ensure the purity of the recycled material [71], [91], [92].

The HD process is mainly influenced by two factors: temperature and pressure. Temperature variations impact the kinetics of hydrogenation processes. Elevated temperatures impact the synthesis of hydrides like NdH_2 and $NdH_{2.27}$ and accelerate the reaction kinetics [74]. Higher temperatures are also associated with more oxidation, especially in finer particles, potentially leading to decreased magnetic properties due to Nd_2O_3 formation [93]. Furthermore, the hydrogen content increases up to 100 °C but starts to decrease above this temperature [74], [81].

Low-temperature HD is primarily driven by local expansion between matrix grains and the formation of NdH_x from the Nd-rich grain boundary phases, ultimately leading to the structural collapse of the magnet. Temperature is a critical factor influencing the degree of pulverization. At lower temperatures, higher pulverization levels are achieved, as hydride formation is less pronounced, resulting in increased material brittleness and easier fragmentation. In contrast, at higher temperatures, pulverization decreases due to the formation of neodymium hydride (NdH_x), a stable phase that prevents further oxidation of Nd-rich regions and reduces material fragmentability. According to the study conducted by Habibzadeh et al. [81], higher temperatures result in larger particle sizes compared to lower temperatures due to a decreased degree of pulverization; specifically, the D50 value is 33 μm at 100 °C and 1220 μm at 400 °C. Additionally, the formation of transgranular cracks with longer structures has been observed in larger particle sizes. Furthermore, in a microstructural analysis, they observed spherical Nd-rich particles. They noted that through vacuum sintering, these particles most likely came from the liquid phase and were not melted again during the following heat treatment. Due to the lower activation energy required for fracture initiation and propagation at lower temperatures, it was mentioned that this spherical phase could be an extra driving force for crack initiation.

Pressure is another key parameter in the HD process. Piotrowicz et. al. [74] demonstrated that increasing pressure results in an increase in hydrogen uptake with decreasing process duration. According to the study, total disintegration occurred at pressures between 2 bar and 4 bar and temperatures below 100 °C. However, when

using sieving techniques to remove the protective coating from the magnet, excessive pressure is not recommended; the ideal decrepitation conditions have been determined to be between 29-100 °C at 1-2 bar.

Li et. al. [78] indicated that the HD process involves four stages at initial hydrogen pressures between 0.1 and 1 MPa: surface activation of magnets, slow hydrogenation of the Nd-rich grain boundary phase, rapid hydrogenation of the $Nd_2Fe_{14}B$ main phase, and slow hydrogenation of the material's interior. Both surface activation and hydrogenation processes are accelerated by rising hydrogen pressure thanks to improved physical adsorption and hydrogen contact with the sample. At pressures of 6–15 MPa, surface activation becomes negligible, merging the hydrogenation stages of the Nd-rich and $Nd_2Fe_{14}B$ phases. Furthermore, it was observed in the study that the hydrogen concentration was independent of the pressure at hydrogen pressures between 0.1 and 0.5 MPa. When the hydrogen pressure exceeds 0.5 MPa, the hydrogen content starts to increase.

Higher pressures facilitate hydrogen absorption, leading to greater volumetric expansion and favoring the formation of intergranular and intragranular cracks. Increased hydrogen absorption leads to smaller-sized powders, which are preferred during subsequent forming operations. Insufficient pressure can result in incomplete hydrogenation, which lowers the degree of anisotropy of the powder with insufficient decrepitation and the formation of polycrystalline particles [76].

CHAPTER 3

EXPERIMENTAL PROCEDURE

3.1 Starting Materials

In this study, 4 scrap sintered $Nd_2Fe_{14}B$ magnets, which have the same serial number, located in the voice coil motor (VCM) of EoL hard disk drives (HDDs) (Figure 3.1) were used as the starting material. The VCM was removed from the HDD using the manual separation method. As seen in Figure 3.2, there are two magnets inside a VCM assembly.

Figure 3.1 Inside of the HDD.

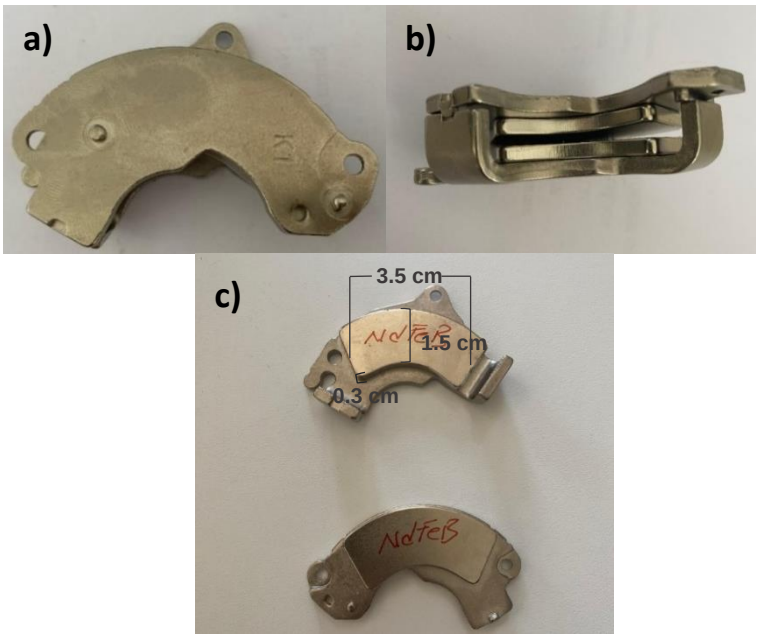

Figure 3.2 a) VCM assembly b) NdFeB magnets in VCM assembly c) NdFeB magnets after separation of VCM assembly.

3.2 Sample Preparation

The coating of the scrap magnet needs to be removed slightly to allow hydrogen to react to the magnet during the HD process; however, removing the coating in the open atmosphere leads to oxidation. In addition, the VCM assembly can only be separated using tools in the open atmosphere and when separated from the magnet it leads to the removal of the coating, thus oxidation occurs. Therefore, the magnet was not separated from the VCM assembly. The coating removal was carried out in a glovebox to minimize the contact of the magnet with oxygen. The oxygen concentration in the environment of the glovebox is 13.5 ppm, and the moisture content is less than 0.5 ppm. The coating of the magnet was slightly removed with a rasp to create fresh surfaces where hydrogen can penetrate the magnet (Figure 3.3). Before HD processing, the magnets were in a magnetic state and had not undergone thermal demagnetization.

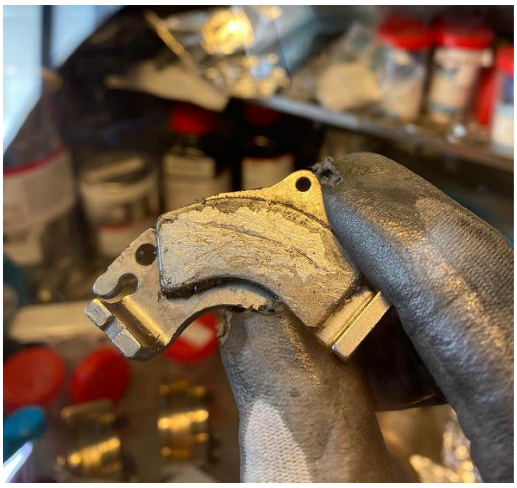

Figure 3.3 Fresh surfaces after the coating removal and hydrogen penetration into the magnet

3.3 Experimental Techniques

3.3.1 Hydrogen Decrepitation Process

The reactor used for the HD process is given in Figure 3.4 (a). Since the reactor is removable, it was placed in the glovebox and the magnet partially separated from its coating was placed in the stainless steel hydrogenation chamber, Figure 3.4 (b), then connected to the system. Initially, the chamber was purged several times using argon gas to ensure that the atmosphere inside the chamber was clean and oxygen-free. Subsequently, hydrogen flow into the system was initiated. The HD process was carried out at room temperature with a constant hydrogen pressure of 2 bar for 2 hours. At the end of 2 hours, the hydrogen flow was stopped, and the hydrogen in the chamber was evacuated. To completely remove the remaining H_2 gas in the chamber, it was purged with argon gas again and then the chamber was opened in the glovebox (Figure 3.4 (c)). To eliminate the broken coating particles of scrap magnets, the HD powder was first softly crushed through a mortar and pestle following the HD process. Then, the powders were sieved with a 500-micron sieve.

After sieving, if any visible coating remained in the powder, it was removed with tweezers. The same procedure was performed for hydrogen pressures of 4 and 6 bar.

Figure 3.4 a) The hydrogenation reactor b) Preparation of the reactor in the glove box c) Magnet powders separated from the VCM assembly after the HD process

3.3.2 Ball Milling

For the ball-milling (BM) process after the HD process, the Spex Sampleprep 8000D Mixer/Mill Figure 3.5 was used. The ball-to-powder ratio for the ball milling process was determined at 10/1. According to this ratio, 8 g of HD powders, 80 g of 3 mm AISI 52100 chrome steel balls, 10 ml of toluene, and 5 drops of oleic acid were placed in a stainless steel jar in the glove box. To prevent oxygen contact that may occur during the BM process, the jar was placed in a vacuum pack Figure 3.6 (a) and then milled for 30 minutes. After BM, the jar was placed in the glove box for 3-4 days to allow the toluene to evaporate and the powders to dry Figure 3.6 (b).

Figure 3.5 Spex Sampleprep 8000D Mixer/Mill.

Figure 3.6 a) Placement of the jar in a vacuum pack to prevent oxygen contact during the BM process b) Dried powders after the BM process

3.4 Characterization Techniques

3.4.1 Chemical Composition Analysis

The chemical composition of the bulk scrap sintered $Nd_2Fe_{14}B$ magnet was determined using inductively coupled plasma optical emission spectroscopy (ICP-OES) (Thermo Scientific/ICAP 7000). The bulk scrap magnet was demagnetized at 300 ^{0}C, and it was ground with a mortar and pestle to prepare 7 individual samples of approximately 0.1 gram for ICP-OES analysis. The powders placed in an acidic combination of 4 mL HNO_3, 1 mL HCl, and 6 mL HNO_3 were completely dissolved

in the microwave at 220 ^{0}C in about 75 minutes. Then diluted 1000 times with 2% HNO_3, ICP-OES measurements were conducted.

3.4.2 Microstructural Analysis

For the microstructural analysis, the demagnetized bulk magnet was first embedded in DuroFast epoxy resin. Then, 500 and 1200-grain grinding papers were used to grind the sample, respectively. Polishing was performed using Diadoublo Mono suspension as a diamond suspension, with a 3 μm grain size. As a final step, oxide polishing was applied using Colloidal Silica Suspension 50 nm Alkaline.

Thickness measurement and elemental analysis were performed on the coating separated from the magnet after the HD process. HITACHI SU5000 Field Emission-Scanning Electron Microscope (FE-SEM) (Figure 3.7) was used to examine the protective coating. The system was equipped with an Oxford X-MaxN 80 Energy Dispersive X-ray Spectroscopy (EDS) detector. The secondary electrons (SE) were used for morphological analysis, and backscattering electrons (BSE) for elemental mapping to obtain the distribution of chemical composition.

Figure 3.7 HITACHI SU5000 FE-SEM.

3.4.3 Magnetic Measurement

Magnetic field-dependent magnetization (M/H) measurements were conducted by Vibrating-Sample Magnetometry (VSM) (Figure 3.8) under a ± 1.8 Tesla magnetic field at room temperature.

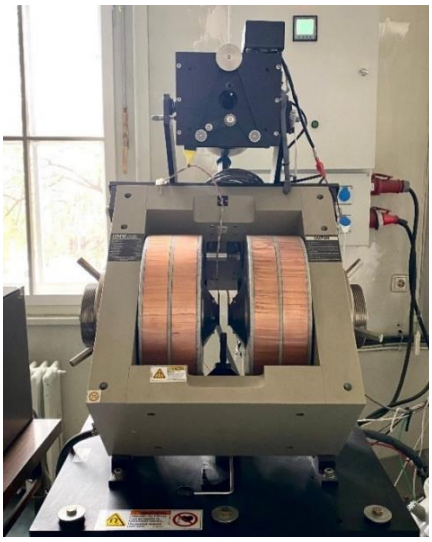

Figure 3.8 GMW Magnet Systems Model 3473-70 Electromagnet VSM

3.4.4 Particle Size Analysis

Particle size analysis of the HD and BM powders was obtained from particle sizes measured from SE images taken at different sites with a HITACHI SU5000 FE-SEM (Figure 3.7).

3.4.5 Oxygen and Hydrogen Contents

LECO TCH 600 N O, H Determinator (Figure 3.9) used for measurement of oxygen and hydrogen contents of HD and BM powders. Approximately 0.05 grams of each sample was weighed, and the measurements were repeated 3 times for each sample. This analysis is carried out by burning the samples at high temperatures. After

combustion, oxygen is converted to CO and/or CO_2, nitrogen to NO_x, and hydrogen to H_2O, and then the measurement is performed.

Figure 3.9 LECO TCH 600.

3.4.6 X-Ray Diffraction (XRD) Analysis

Phase constituents of HD powders and ball-milled (BM) powders were measured by X-ray diffractometer (XRD) (Malvern Panalytical/Empyrean) (Figure 3.10). XRD analysis was continuously scanned between 20° and 80° 2θ angles, provided Co-Kα radiation at 40 kV, and the scan speed was 0.07 °/sec. Phase analysis was performed using HighScore Plus XRD Analysis Software.

The crystallite size and microstrain of the HD and BM powders were calculated from the XRD pattern using HighScore Software. The crystallite size calculation is based on Debye-Scherrer Equation [94]:

$$D = k\,\lambda / \beta\cos\theta \quad (\textit{Equation 8})$$

where D is the crystallite size, λ is the x-ray wavelength (λ= 1.7902 Å), β is full width at half maximum (FWHM) of the detected peak and θ is the diffraction angle.

The following formula is used to determine strain-induced broadening:

$$\varepsilon = \beta/4 \tan \theta \quad (\textit{Equation 9})$$

Figure 3.10 X-ray diffractometer (Malvern Panalytical/Empyrean).

CHAPTER 4

RESULTS AND DISCUSSION

In this section, the compositional and microstructural analysis of the scrap sintered NdFeB magnets are initially presented and discussed. Then, the microstructural, magnetic, and structural characterization of the scrap magnets after the HD process using different hydrogen pressures and the subsequent ball-milling process are introduced, and the effect of different pressures on the powders is compared. Figure 4.1 provides a schematic representation of the entire context of the obtained results.

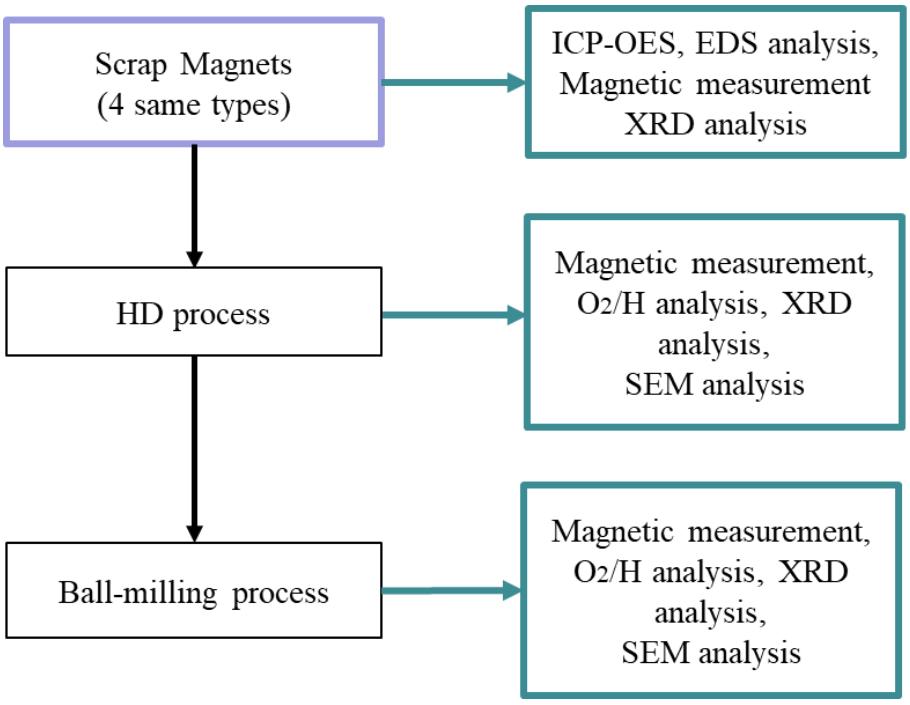

Figure 4.1 A schematic representation of the results and discussion chapter.

4.1 Inductively Coupled Plasma Optical Emission Spectroscopy

According to ICP-OES results, the chemical composition of the scrap NdFeB magnet is given in Table 4.1. Along with the conventional NdFeB magnet composition (Nd,

Fe, and B), the starting material additionally included praseodymium (6.05 wt%), dysprosium (1.13 wt%), cobalt (0.88 wt%), and nickel (1.05 wt%), which are part of the protective coating. These values are in line with the composition ranges of typical HDD magnets [95]. There are also small amounts of other alloying elements (in total about 1.84 wt.%). The composition of the scrap NdFeB magnet is given in Table 4.1.

Table 4.1 The composition of the scrap NdFeB magnet with standard deviations

	Fe	**Nd**	**B**	**Pr**	**Dy**	**Nb**	**Ni**
wt%	62.72	22.20	0.85	6.05	1.13	1.28	1.05
Std dev	3.03	1.01	0.08	0.28	0.07	0.64	0.06
	Co	**Al**	**Tb**	**Ho**	**Cu**	**Ti**	**Gd**
wt%	0.88	0.45	0.37	0.15	0.16	0.02	0.05
Std dev	0.07	0.08	0.06	0.04	0.04	0.01	0.02

4.2 Microstructural Examination

4.2.1 Before Hydrogen Decrepitation Process

Figure 4.2 shows the microstructure of the sintered scrap magnet. It consists mainly of the $Nd_2Fe_{14}B$ main matrix with gray areas and is surrounded by the Nd-rich phase with other alloying elements with white areas and B-rich phases ($Nd_{1+\varepsilon}Fe_4B_4$) [96], [97]. Additionally, the neodymium oxide phase is also observed [92].

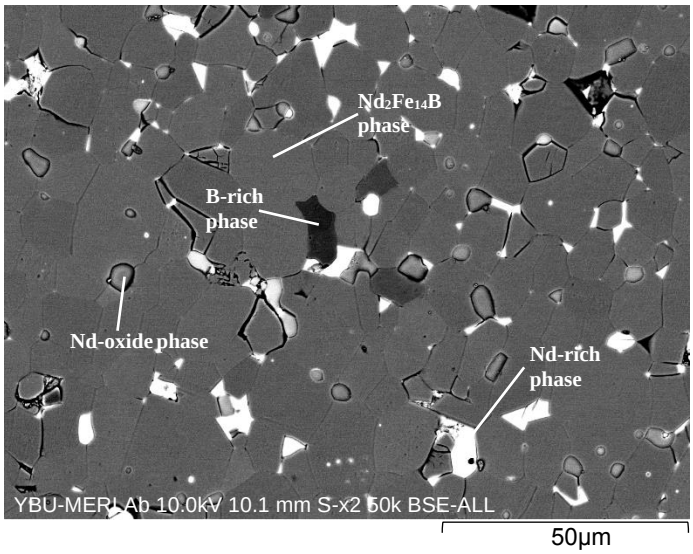

Figure 4.2 SE image of the microstructure of the sintered scrap magnet

A BSE photograph of the protective coating is seen in Figure 4.3 (a). The thickness of the protective coating was measured as 10 µm (Figure 4.3 (b)).

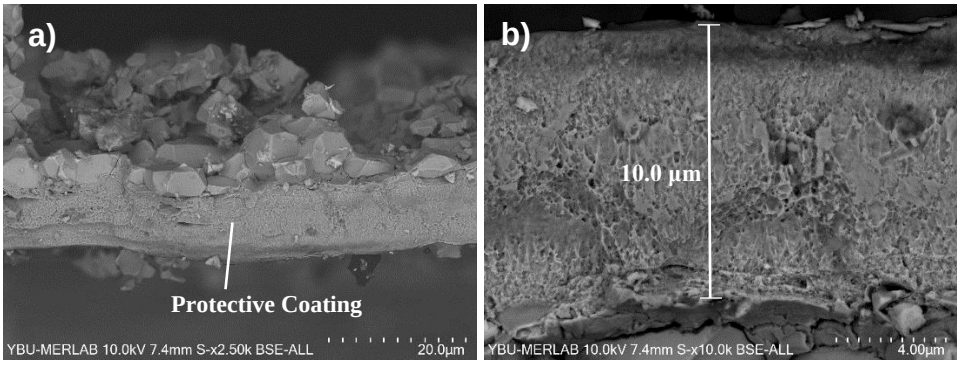

Figure 4.3 BSE images of protective coating a) at 2500x magnification and b) at 10,000x magnification

To determine the chemical composition of the coating, EDS measurements were conducted on the top of the surface. The chemical composition of the coating is given in Table 4.2. According to the results, the coating was made of nickel (95.1 ± 0.2 wt%). The carbon content (4.5 ± 0.1 wt%) can be due to the production line during the manufacturing of the magnet, and the carbon band used for attaching the sample holder. Additionally, as this scrap magnet was removed from an EOL HDD, it is to be expected that the coating will be damaged over time, which explains the oxygen content (0.4 ± 0.1 wt%).

Table 4.2 Chemical composition (wt%) of the protective coating

Ni	C	O
95.1 ± 0.2	4.5 ± 0.1	0.4 ± 0.1

4.2.2 After Hydrogen Decrepitation Process

Intergranular and transgranular fractures were observed in the SEM images of the HD powders (see. Figure 4.4). As mentioned in the literature [76], the dominant mode was observed to be intergranular fracture (Figure 4.4 (b, c, d)), since at lower temperatures the degree of pulverization increases. Figure 4.4 (a) shows the enclosed transgranular fracture, which originates inside the matrix grain but does not extend to the grain's edges. As observed in the study conducted by Habibzadeh et al. [81], although intergranular cracks were observed in the structure due to lower pulverization degree in studies carried out at high temperatures, the transgranular crack rate is higher according to this study. Furthermore, in accordance with the studies of Habibzadeh et al. [81], spherical Nd-rich phase and micro-indent impression, which is an effect of this phase, were observed, as seen in Figure 4.4 (c, e), which is indicated to contribute to the initiation of crack formation at low temperatures.

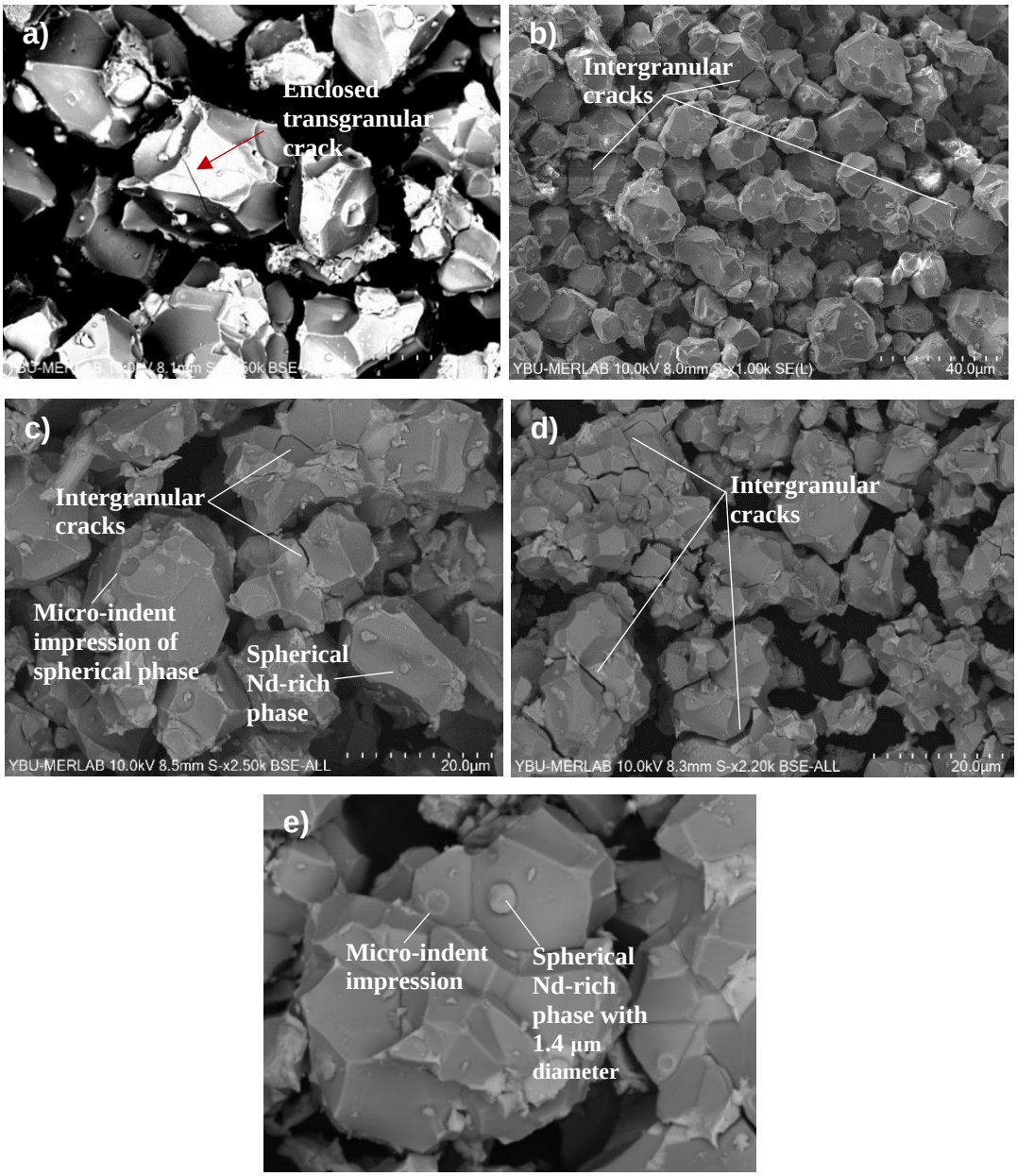

Figure 4.4 SEM images of intergranular and enclosed transgranular cracks, spherical Nd-rich phase, and its micro-indent impression after the HD processing at a) 2 bar (1), b) 2 bar (2) c) 4 bar, d) 6 bar. e) Closer look at the spherical Nd-rich phase.

Figure 4.5 shows the SE images of 2 bar, 4 bar, and 6 bar HD powders at 1000x magnification. As seen in the images, the bulk magnet effectively turned into powder through the HD process. However, with increasing pressure, increasing polycrystalline particles, which consist of many grains, were observed. It can be due to a decrease in diffusion rate differences between the main matrix and grain boundary. This may reduce the stress required to break the particles [78]. Polycrystalline particles affects adversely the homogeneity of particle size distribution; however, subsequent ball-milling already aims to achieve a more uniform and smaller particle size distribution. Notably, it can be said that there is a considerable reduction in particle size when comparing 2 bar HD powder (Figure 4.5 (a)) with 4 and 6 bar (Figure 4.5 (b, c)), but there is no observable difference between 4 and 6 bar HD powders.

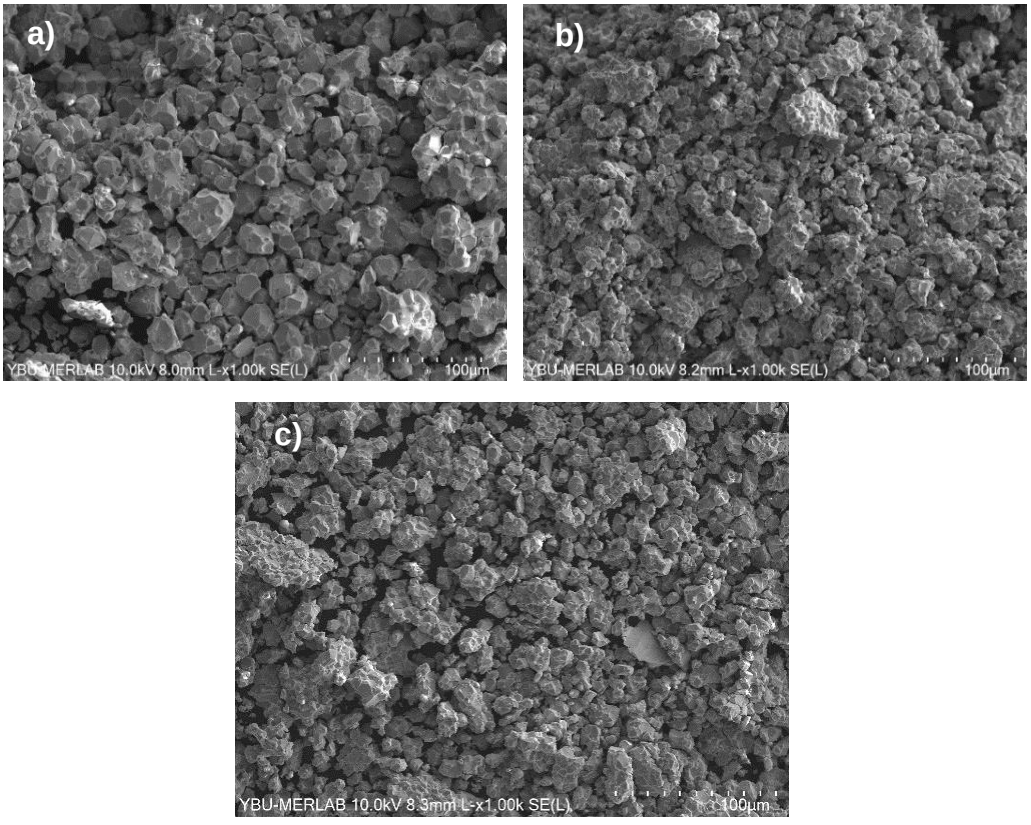

Figure 4.5 SE images of a) 2 bar HD, b) 4 bar HD, c) 6 bar HD powders at 1000x magnification.

SE images taken after the ball milling process applied to 2, 4, and 6 bar HD powders are represented in Figure 4.6. A notable reduction in particle size was observed when comparing BM powders to HD powders. Furthermore, the shape of the particles became flake-like, which is in line with the literature [96]. Although some drops of oleic acid were used during the BM process to prevent particle agglomeration, the large particles seen in the images are likely due to agglomeration. Particle agglomeration may result from decreasing particle size as it increases surface area and raises surface energy. To bring the formula back into balance, the particles have a tendency to gather together by lowering their surface energy [98].

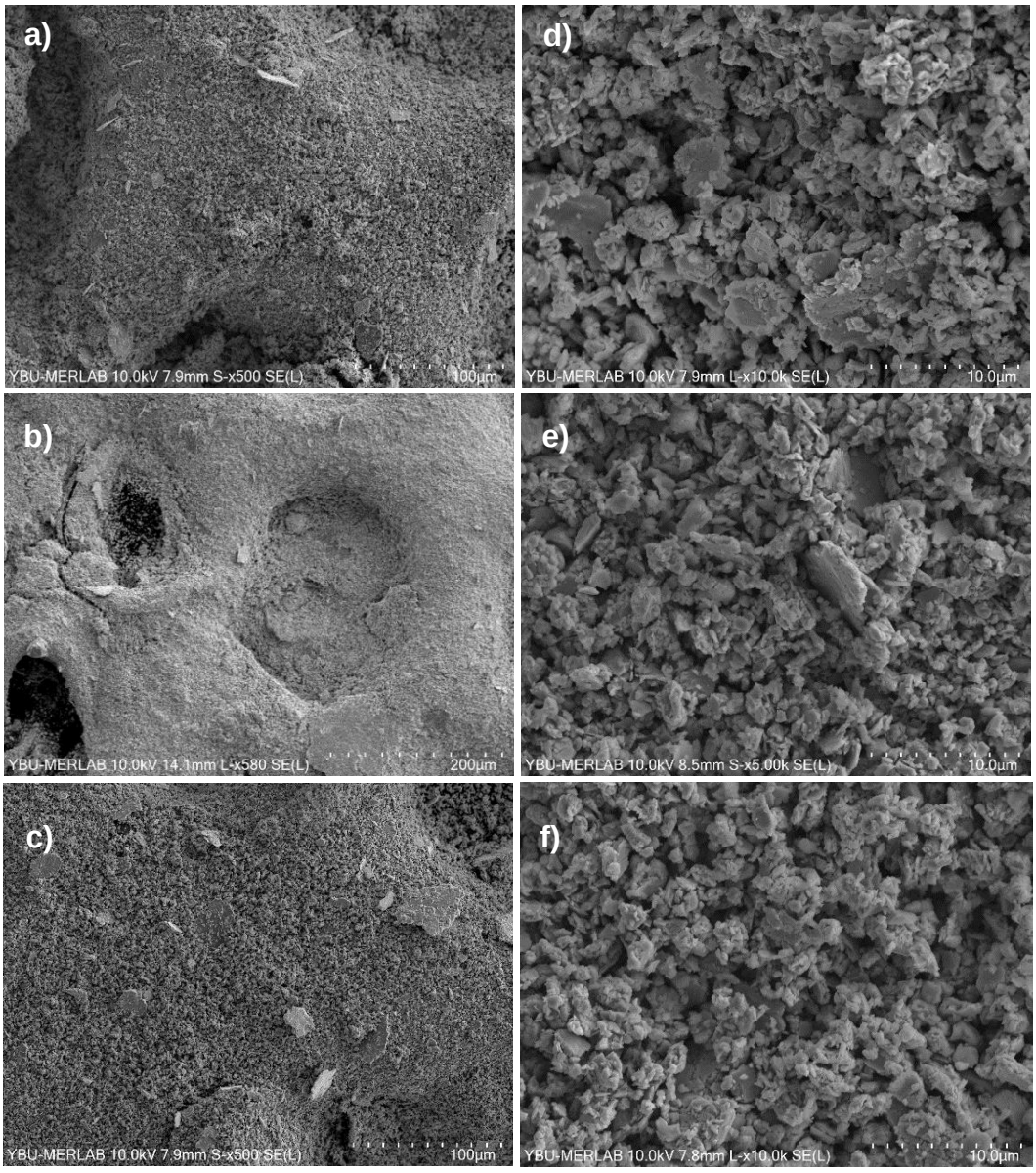

Figure 4.6 SE images of a) 2 bar BM, b) 4 bar BM, c) 6 bar BM powders at 500x magnification, d) 2 bar BM, e) 4 bar BM, f) 6 bar BM powders at 10,000x magnification.

4.3 Magnetic Measurement

The hysteresis curves for raw scrap NdFeB magnets and HD powders highlight significant differences in magnetic properties, which are represented in Figure 4.7 (a). The scrap NdFeB magnet exhibited a coercivity (H_c) of approximately 2555 Oe and a remanent magnetization (M_r) of 141 emu/g. In contrast, the H_c of the HD powders (Figure 4.7 (b)) was below the threshold required for PM performance, which is above 125 Oe [18], indicating a transition from hard magnetic to soft magnetic behavior due to hydrogen entrance into the structure. In other words, the magnet is demagnetized as a result of the HD process, aligning with findings in the literature [12].

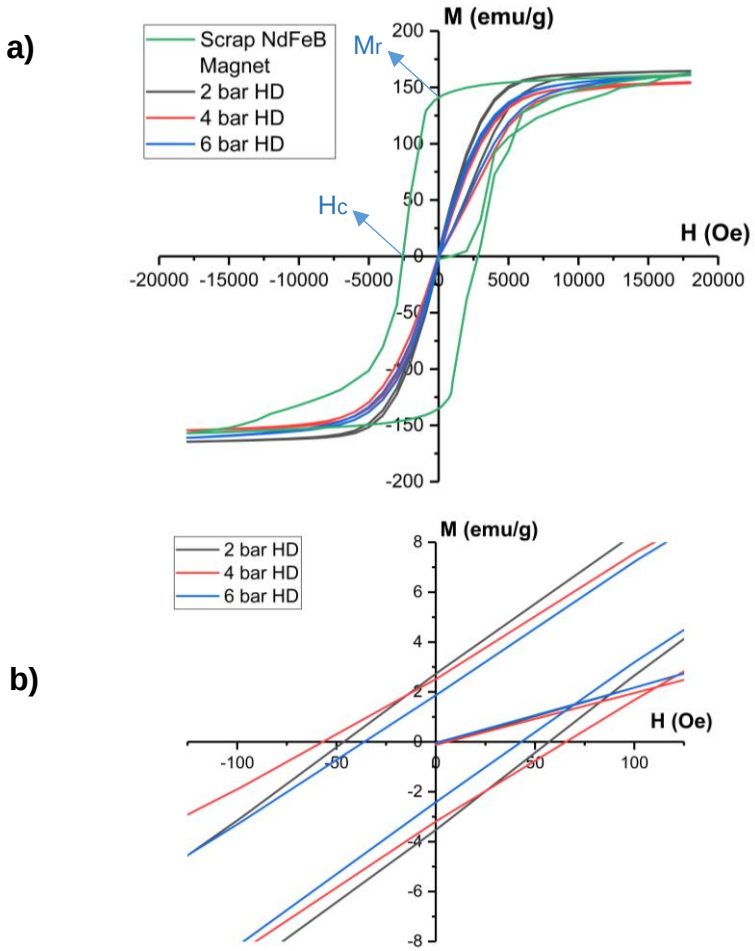

Figure 4.7 a) M-H graphs of scrap NdFeB magnet and, 2 bar, 4 bar, and 6 bar HD powders b) closer look at HD powders M/H curves

The magnetic hysteresis loops obtained after the BM process are given in Figure 4.8. Interestingly, powders demagnetized by HD treatment exhibited an increase in H_c values following the BM process. H_c values reached the range of 600-800 Oe values, which is above the limit required for hard magnetic material.

Smaller particle sizes have a larger surface-area-to-volume ratio, which increases surface anisotropy. In addition, smaller grains lead to a higher density of grain boundaries that serve as pinning sites. This increase in H_c could be due to decreasing grain size increases coercivity [19]. However, the existing literature lacks research on this point, highlighting the need for further research.

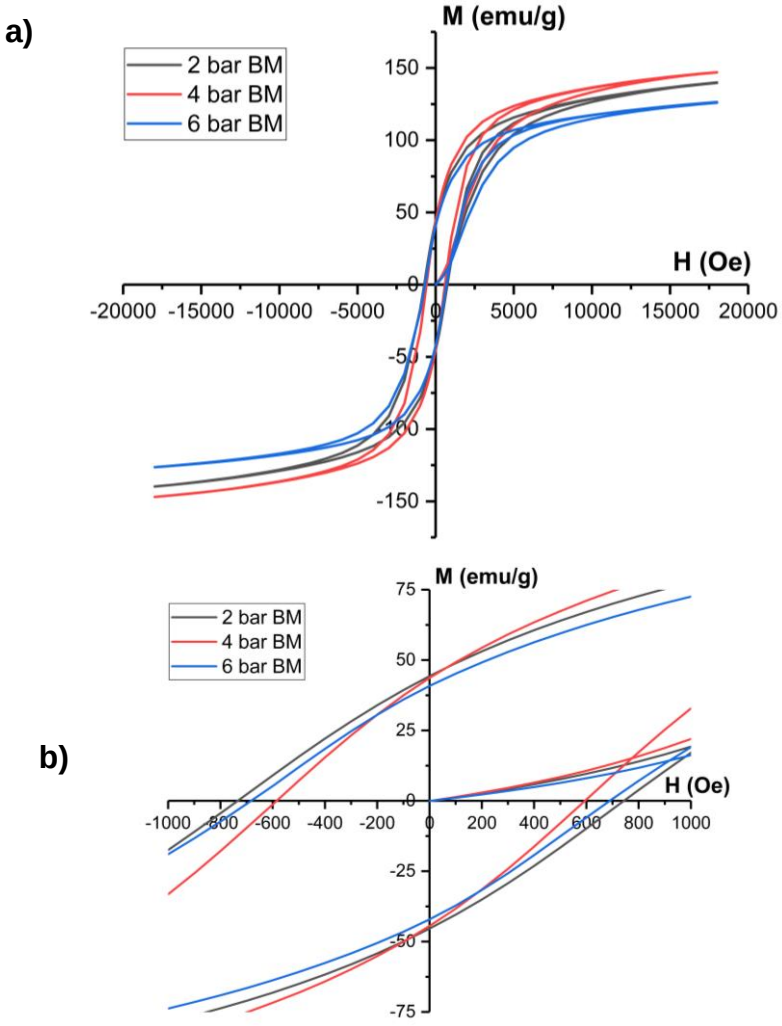

Figure 4.8 a) M-H graphs of scrap NdFeB magnet and, 2 bar, 4 bar, and 6 bar BM powders b) closer look at BM powders M/H curves

4.4 Oxygen and Hydrogen Content

The oxygen and hydrogen concentration results after the HD process and subsequent ball-milling process are given in Table 4.3. According to the results, an average oxygen content of 0.7 wt% falls into the range identified by Kim et al. [61] and Minowa et al. [62]. Although the 4 bar HD is the closest to the recommended oxygen concentration, the oxygen rates after the HD process are above the recommended oxygen rate, and these values increase even more after the ball-milling process.

Table 4.3.Oxygen and Hydrogen contents (wt%).

Sample	Oxygen	Hydrogen
2 bar HD	1.58 ± 0.03	0.307 ± 0.01
4 bar HD	0.796 ± 0.015	0.275 ± 0.004
6 bar HD	0.837 ± 0.027	0.255 ± 0.002
2 bar BM	3.827 ± 0.542	0.335 ± 0.017
4 bar BM	3.233 ± 0.684	0.465 ± 0.148
6 bar BM	3.328 ± 0.2	0.309 ± 0.018

Considering the literature, an increase in hydrogen content was expected as the hydrogen pressure increased [74]. On the contrary, the results of the HD powders show a decrease in hydrogen content as the hydrogen pressure increases, even though there are very small differences between the hydrogen contents. This can be explained in two ways. (1) Increasing the pressure enhances the diffusion kinetics and decreases the processing time [74]. In other words, increasing pressure increases the mobility of hydrogen. Accordingly, hydrogen with increased mobility enters the structure faster and can also exit the structure more quickly. The entry of hydrogen into the structure is sufficient for the HD process to take place, it does not need to remain in the structure. (2) Additionally, LECO analysis conducted at room temperature and 1 bar pressure may not reflect actual hydrogen content quantitatively. At pressures higher than 1 bar, some of the residual hydrogen in

hydrogenated powders may be released at 1 bar, considering that higher pressures increase hydrogen solubility.

On the other hand, the increase in hydrogen content after the BM process compared to the HD process can be due to the moisture in the glove box and toluene ($C_6H_5CH_3$) used during the process. However, moisture in the glove box was very small (< 0.5 ppm), and toluene was evaporated. There is no information about this situation in the literature; therefore, this needs further investigation.

4.5 X-Ray Diffraction

X-ray powder diffraction analyses of crystal structure and phase analyses were performed between 2θ=20°-80° using a Co-Kα source (λ= 1.7902 Å). Using the obtained XRD analysis data, the crystal structure and phase analysis of the powders were analyzed using Panalytical HighScore Plus software. In phase analysis, phases compatible with reference databases were determined.

XRD pattern of the scrap NdFeB magnet before the HD process is presented in Figure 4.9. The measurement was made after the demagnetized bulk magnet was crushed into powder in a mortar and pestle in the glovebox. In the XRD phase analysis of the scrap magnet, Neodymium Iron Boron ($Nd_2Fe_{14}B$) and Neodymium Oxide (Nd_2O_3) phases were matched with ICSD database 98-004-1393 and ICSD database 98-002-6867, respectively. This is consistent with the literature [81]. Since oxygen content was detected due to the possibility of damage to the protective coating based on the EDS findings, it was expected to detect the Nd_2O_3 phase (0.9 wt%) in the scrap NdFeB magnet at the XRD phase analysis results. Lattice parameters of the $Nd_2Fe_{14}B$ phase and Rietveld parameters are shown in Table 4.4.

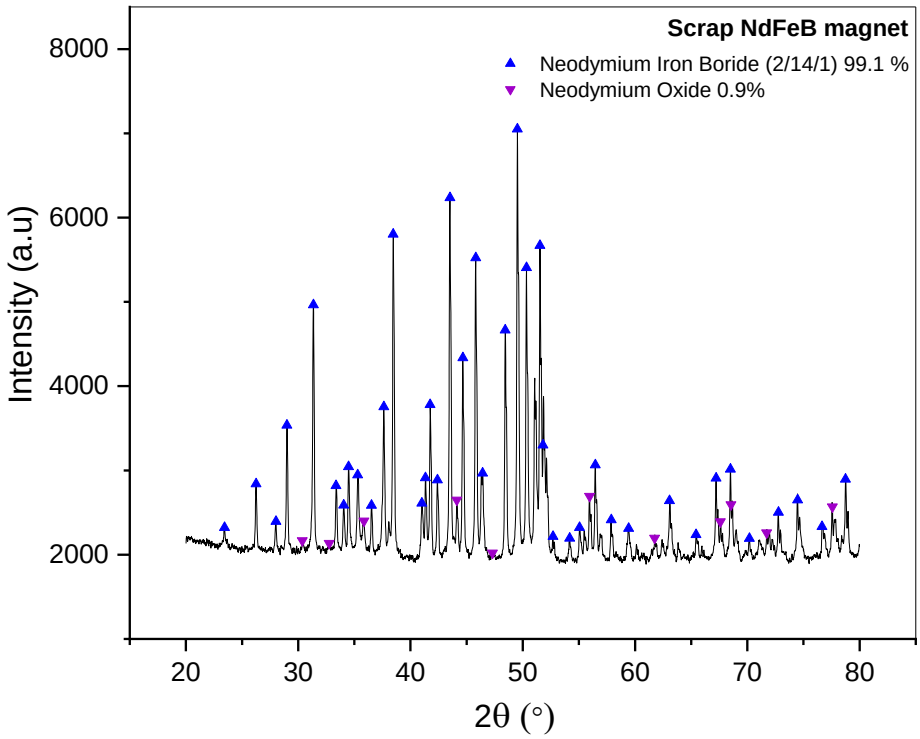

Figure 4.9 XRD pattern of the scrap NdFeB magnet before the HD process.

Table 4.4 Lattice parameters of $Nd_2Fe_{14}B$ phase and Rietveld parameters for demagnetized NdFeB magnet.

	a [Å]	**c [Å]**	**V [Å³]**	**Chi Square (χ^2)**	**Rp**	**Rwp**	**Rexp**
NdFeB Magnet	8.799	12.211	945.405	1.40	2.1	2.8	1.9

XRD patterns for 2 bar, 4 bar and 6 bar HD powders are given in Figure 4.10, Figure 4.11, and Figure 4.12, respectively. Neodymium Iron Boron Hydride ($Nd_2Fe_{14}BH_{3.31}$) and Neodymium Oxide (Nd_2O_3) phases were observed in phase analysis. It is seen that the main phase crystallizes in P 42/mnm (space group no= 136) tetragonal crystal structure, which also belongs to the 2:14:1 structure. As noted in Chapter 2, hydrogen enters the microstructure without changing the microstructure and the space group [85]. The observed $Nd_2Fe_{14}BH_{3.31}$ phase for each

sample indicates that hydrogen was successfully incorporated into the structure and formed the desired phase.

In the XRD phase analysis of HD powders, Neodymium Iron Boron Hydride ($Nd_2Fe_{14}BH_{3.31}$), Neodymium Oxide (Nd_2O_3) and Neodymium(III) Oxide (Nd_2O_3) phases were matched with ICSD database 98-0008-0974, ICSD database 98-003-2514, and ICSD database 98-018-4526 reference codes respectively.

The results of the phase analysis for the HD powders are given in Table 4.5. The Nd_2O_3 phase values in the table are the total values of Neodymium Oxide (Nd_2O_3) and Neodymium(III) Oxide (Nd_2O_3) phases. Although the absence of NdH_2 phase formation in the phase analysis contradicts some studies [21], [79], it has been revealed by previous studies that the NdH_2 phase does not form at room temperature [80], [81]. In this study, since the HD process was conducted at room temperature, and therefore no hydride formation was observed in the material. The increasing Nd-oxide phases in HD powders compared to the scrap magnet (0.9 wt%) may be attributed to the absence of hydride formation at low temperatures. The presence of Nd-oxide phases in the microstructure may be attributed to the absence of hydride formation at low temperatures. Without hydride formation, the Nd-rich regions are unable to develop a stable structure that effectively prevents oxidation, leading to the observed Nd oxide phases [81].

LECO analysis results (Table 4.3) are consistent with XRD phase analysis results. As the hydrogen contents were almost constant, the phase distribution was proportional to the oxygen contents. Since 2 bar HD has the highest oxygen content (1.58 ± 0.03 wt%), the formation of the Nd_2O_3 phase (in total about 8 wt%) is higher than others. Furthermore, according to LECO analysis results, 6 bar HD has more oxygen content (0.837 ± 0.027 wt%) compared to 4 bar HD (0.796 ± 0.015 wt%), and based on phase analysis results, the oxide phase formed at 6 bar HD (3.9 wt% Nd_2O_3) is more than at 4 bar HD (3 wt% Nd_2O_3). According to this, the best outcomes were obtained in 4 bar HD powder with the formation of the highest main phase (96.6 wt% $Nd_2Fe_{14}BH_{3.31}$) and the lowest oxide phase (3 wt% Nd_2O_3).

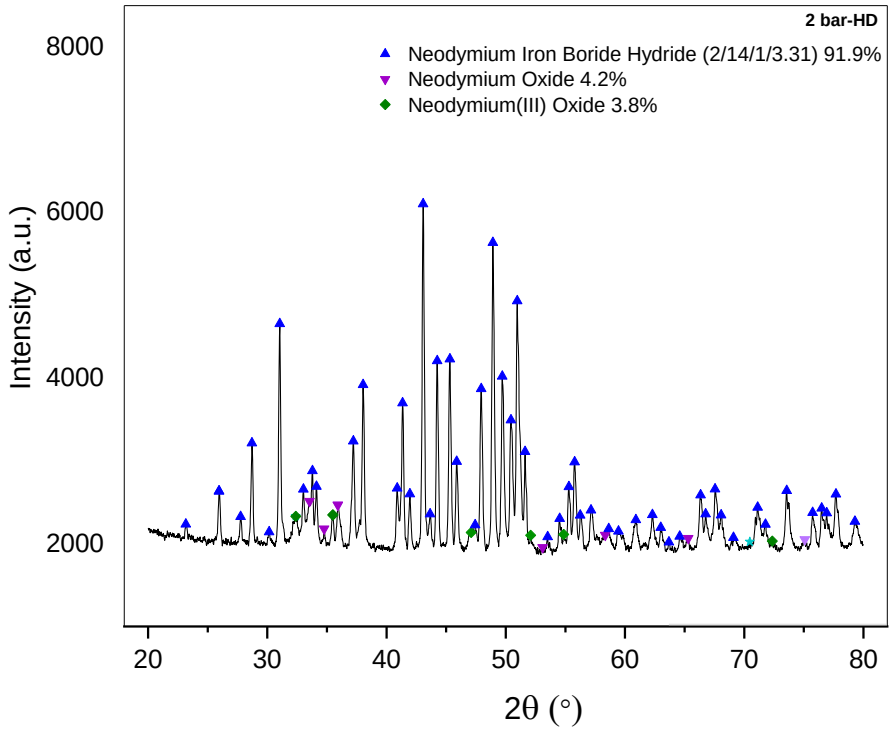

Figure 4.10 XRD pattern of 2 bar HD

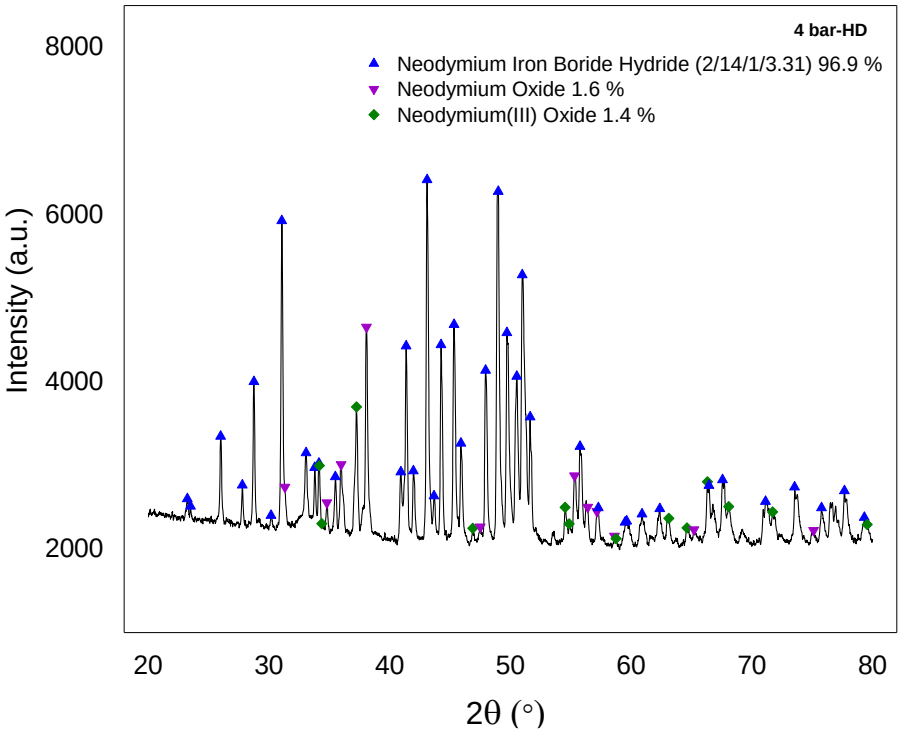

Figure 4.11 XRD pattern of 4 bar HD

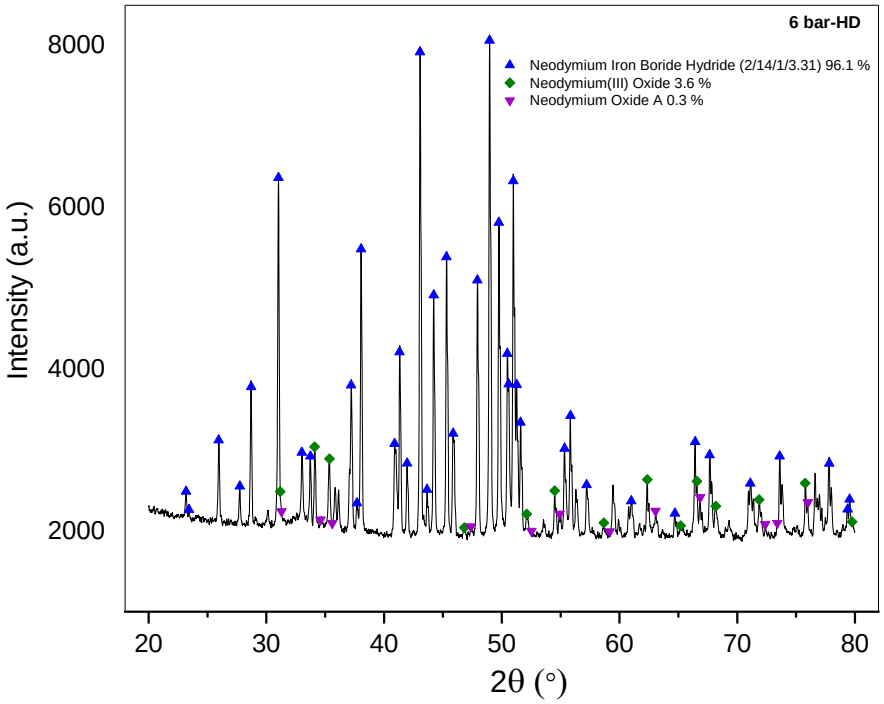

Figure 4.12 XRD pattern of 6 bar HD

Table 4.5 XRD phase analysis results (wt%) for 2 bar HD, 4 bar HD, and 6 bar HD.

	$Nd_2Fe_{14}BH_{3.31}$	Nd_2O_3
2 bar HD	91.9	8.1
4 bar HD	96.9	3
6 bar HD	96.1	3.9

Lattice parameters of the $Nd_2Fe_{14}BH_{3.31}$ phase and Rietveld parameters are given in Table 4.6. As seen in the table lattice parameters of HD powders increased compared to the scrap magnet (a = 8.799 Å, c = 12.211 Å). The volume of the main matrix of the scrap magnet (V= 945.405 Å^3) experienced an increase of 3.59%, 3.62%, and 3.18% for 2, 4, and 6 bar HD powders, respectively. According to the growth rates of the volumes, the most expansion was achieved in 4 bar HD powders. The fact that 6 bar HD has the least expansion might be due to decreasing stress between the main matrix and grain boundary, as mentioned earlier. Moreover, when the XRD patterns

before and after HD treatment are compared, the HD peaks are shifted to the left as seen in Figure 4.13. Overall, the left shift of the peaks and the increase in the lattice parameters compared to before hydrogenation prove that hydrogen enters the structure, leading to volume expansion.

Table 4.6 Lattice parameters of $Nd_2Fe_{14}BH_{3.31}$ phase and Rietveld parameters for 2 bar HD, 4 bar HD, and 6 bar HD.

	a [Å]	**c [Å]**	**V [Å³]**	**ΔV (%)**	**Chi Square (χ^2)**	**Rp**	**Rwp**	**Rexp**
2 bar HD	8.912	12.331	979.374	3.59	1.3	2.1	2.7	2.1
4 bar HD	8.913	12.332	979.673	3.62	1.9	2.8	3.8	2.0
6 bar HD	8.896	12.326	975.465	3.18	1.9	2.5	3.5	2.1

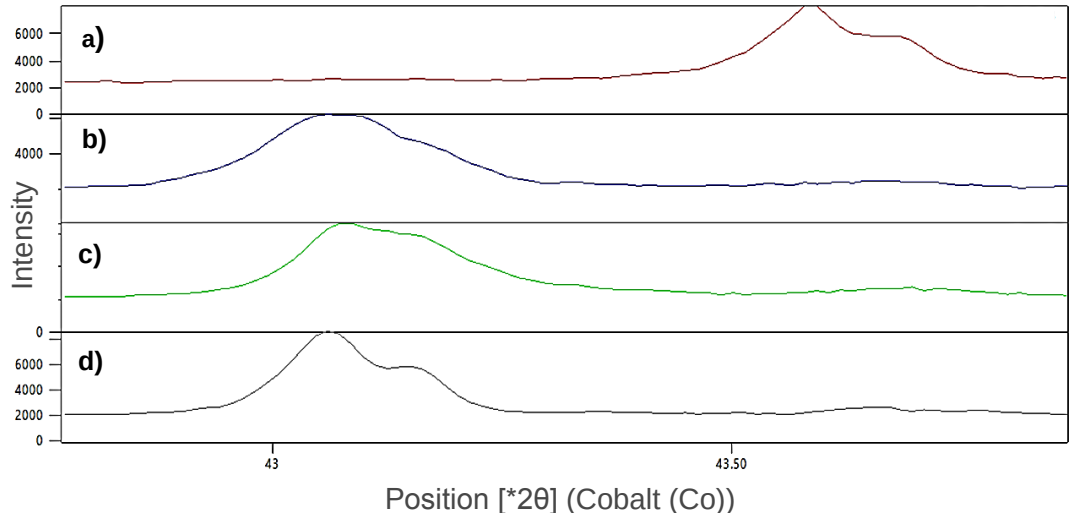

Figure 4.13 Comparison of XRD peaks of a) the scrap NdFeB magnet before the HD process, b) 2 bar HD, c) 4 bar HD, and d) 6 bar HD.

XRD analysis was performed to observe how the crystal structure changed after the BM process. XRD patterns of 2 bar BM, 4 bar BM, and 6 bar BM are presented in Figure 4.14, Figure 4.15, and Figure 4.16, respectively. In the phase analysis, Neodymium Iron Boron Hydride ($Nd_2Fe_{14}BH_{3.31}$) and Neodymium Oxide (Nd_2O_3) phases were matched with ICSD database 98-0008-0974 and ICSD database 98-002-6867, respectively, as in the HD powders.

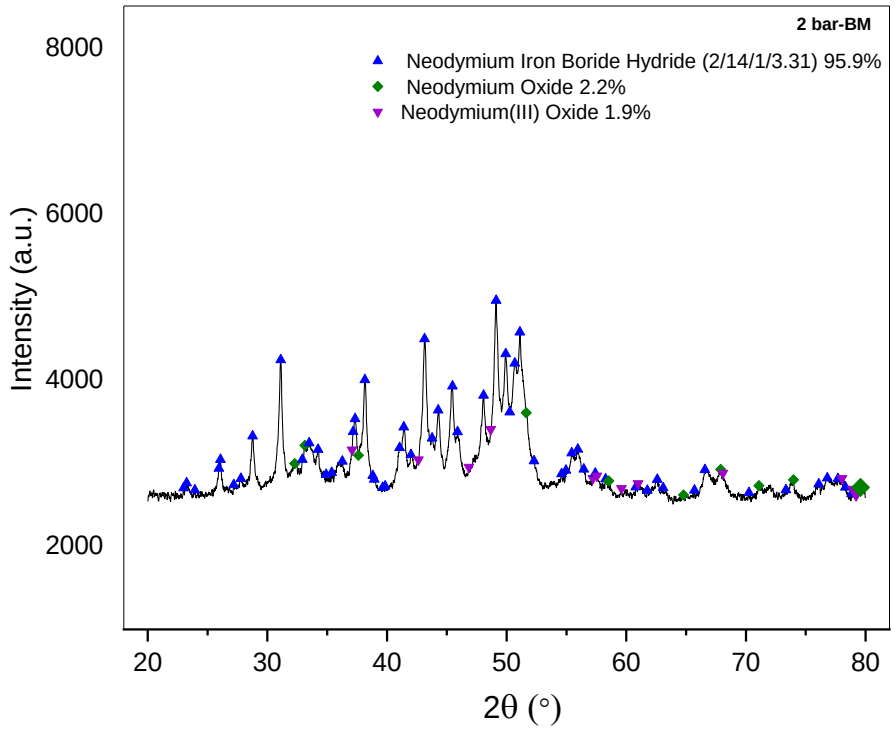

Figure 4.14 XRD patterns of 2 bar BM

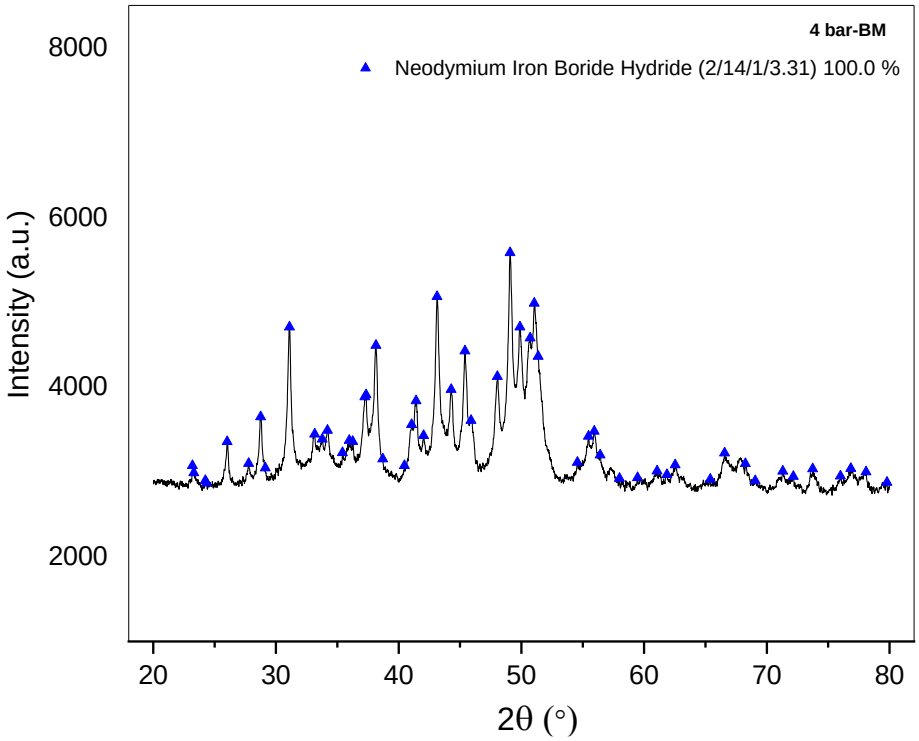

Figure 4.15 XRD patterns of 4 bar BM

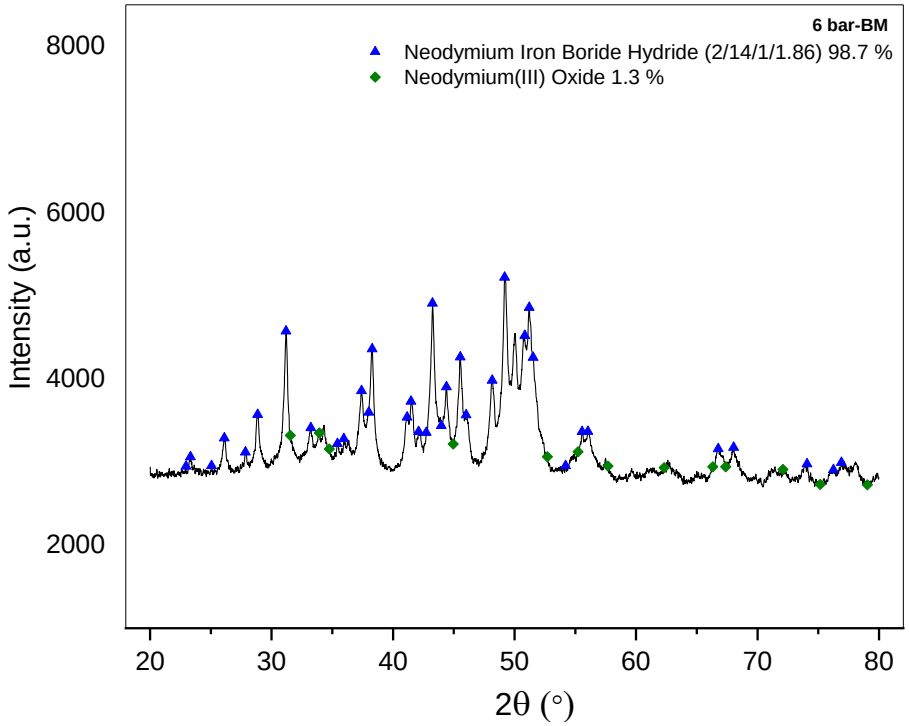

Figure 4.16 XRD patterns of 6 bar BM

The results of the phase analysis can be seen in Table 4.7. According to the LECO analysis results (Table 4.3), it was observed that the oxygen content increased after BM compared to the HD process, while the phase analysis results showed that the oxide phase decreased. Even 100 wt% $Nd_2Fe_{14}BH_{3.31}$ phase was detected for 4 bar BM. However, when the XRD patterns of BM powders are analyzed, a broadening of the peaks is observed compared to the HD powders. The broadening observed in the peaks following the BM process may have caused the oxide phases to remain beneath the dominant peaks in the XRD analysis, making their detection challenging. This could be attributed to the broadening effect, which may have masked or overlapped the weak signals of the oxide phases. According to the literature that Williamson and Hall stated, strain and crystallite size both contribute to the broadening of the diffraction line [99].

Table 4.7 XRD phase analysis results (wt%) for 2 bar BM, 4 bar BM and 6 bar BM.

	$Nd_2Fe_{14}BH_{3.31}$	**Nd_2O_3**
2 bar HD	95.8	4.1
4 bar HD	100	-
6 bar HD	98.7	1.3

Lattice parameters of the $Nd_2Fe_{14}BH_{3.31}$ phase and Rietveld parameters are given in Table 4.8. When BM powders were compared with the volume of HD powders, a decrease of 0.91% in 2 bar HD, 0.81% in 4 bar HD, and 0.71% in 6 bar HD powder was observed.

Table 4.8 Lattice parameters of $Nd_2Fe_{14}BH_{3.31}$ phase and Rietveld parameters for 2 bar BM, 4 bar BM, and 6 bar BM.

	a [Å]	c [Å]	V [Å³]	ΔV (%)	Chi Square (χ^2)	Rp	Rwp	Rexp
2 bar BM	8.877	12.315	970.436	- 0.91	1.3	1.9	1.9	1.9
4 bar BM	8.882	12.318	971.766	- 0.81	1.4	2.5	2.5	2.4
6 bar BM	8.871	12.308	968.574	- 0.71	1.3	1.9	1.8	1.8

The crystallite size and microstrain of the HD and BM powders were calculated using HighScore Plus Software. The calculation involves Equation 8 and Equation 9. For the comparison of the crystallite size of HD and BM powders, the highest intensity peak of HD powders was selected as indicated in Table 4.9.

Table 4.9 The position, FWHM, crystalline size, and microstrain for the observed peak having the highest intensity

	Position (°2θ)	FWHM (°2θ)	Crystallite Size (Å)	Microstrain
2 bar HD	43.050	0.1602	836	0.146
2 bar BM	43.119	0.34	198	0.613
4 bar HD	43.088	0.1408	1009	0.121
4 bar BM	43.109	0.3199	220	0.553
6 bar HD	43.053	0.0953	2822	0.043
6 bar BM	43.226	0.3036	206	0.590

According to the FWHM measurements, it can be seen that the FWHM values increase after the BM process, i.e. the peaks broaden as mentioned before. Peak

broadening results from strain in the structure caused by deformation and defects in the crystal. XRD peaks expand as crystallite size decreases and crystal lattice defects develop [99]. In line with this, analysis of crystallite size reveals significant reductions when comparing BM powders to HD powders under varying pressures. Specifically, crystallite size in 2 bar BM powders decreased by 76.32% relative to 2 bar HD powders, 4 bar BM powders showed a 78.20% decrease compared to 4 bar HD powders, and 6 bar BM powders exhibited a 92.7% reduction in crystallite size compared to their 6 bar HD powders. The reduction in crystallite size is accompanied by an increase in lattice imperfections, leading to higher microstrains. Compared to HD powders, the microstrain values in BM powders at pressures of 2 bar, 4 bar, and 6 bar increased by factors of 4.2, 4.57, and 13.72, respectively. As a consequence, the decrease in particle size led to peak broadening, decreased crystallite size, and increased microstrain.

4.6 Particle Size Distribution

SE images taken from 3 different locations of each sample were used to determine the particle size distribution of HD powders. The measurements of the particle size were done by visual observation, and Figure 4.17 shows an example from the measurements. Particle size measurement with SEM images is limited by the number of particles selected and depends on user choice. 156 particles for 2 bar HD, 83 particles for 4 bar HD, and 131 particles for 6 bar HD were selected and measured manually. For BM powders, 122 particles were measured for 2 and 4 bar BM and 127 particles for 6 bar BM. As shown in Figure 4.17 (a), small non-polycrystalline particles were selected during HD powder particle size measurement. On the other hand, during BM powder measurements (Figure 4.17 (b)), both agglomerated particles and single particles were selected.

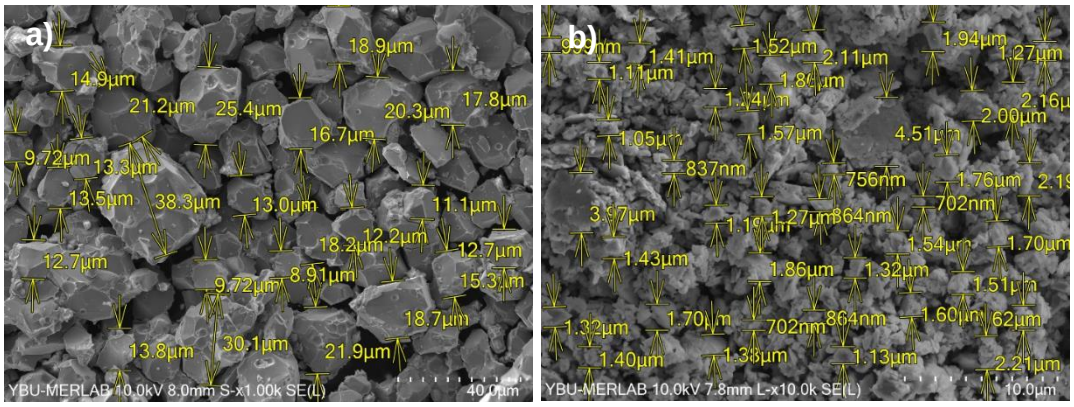

Figure 4.17 SEM images of particle size measurement of a) 2 bar HD, and b) 2 bar BM powders

The calculated average particle diameters for the HD powders are as follows: 16.25 ± 3.91 µm for 2 bar HD, 13.84 ± 4.52 µm for 4 bar HD, 9.59 ± 2.24 µm for 6 bar HD. Particle size distribution graphs for HD powders at 2 bar, 4 bar, and 6 bar are presented in Figure 4.18, Figure 4.19, and Figure 4.20, respectively. The graphs indicate that the Gaussian curves for the particle size distribution are in the ranges of 12-16 µm for 2 bar, and 8-12 µm for 4 bar and 6 bar HD powders. This is supported by the fact that the 2 bar HD powder observed in the SEM analysis had a larger particle size than the others, but there was no observable difference in the 4 and 6 bar HD powders.

It was observed in the microstructural analysis that intergranular fracture was dominant due to the increase in the degree of pulverization at low temperatures. When the particle sizes obtained in the previously mentioned study [81] where the HD process was carried out at high temperatures were examined, it was determined that much smaller particle sizes were obtained in this study.

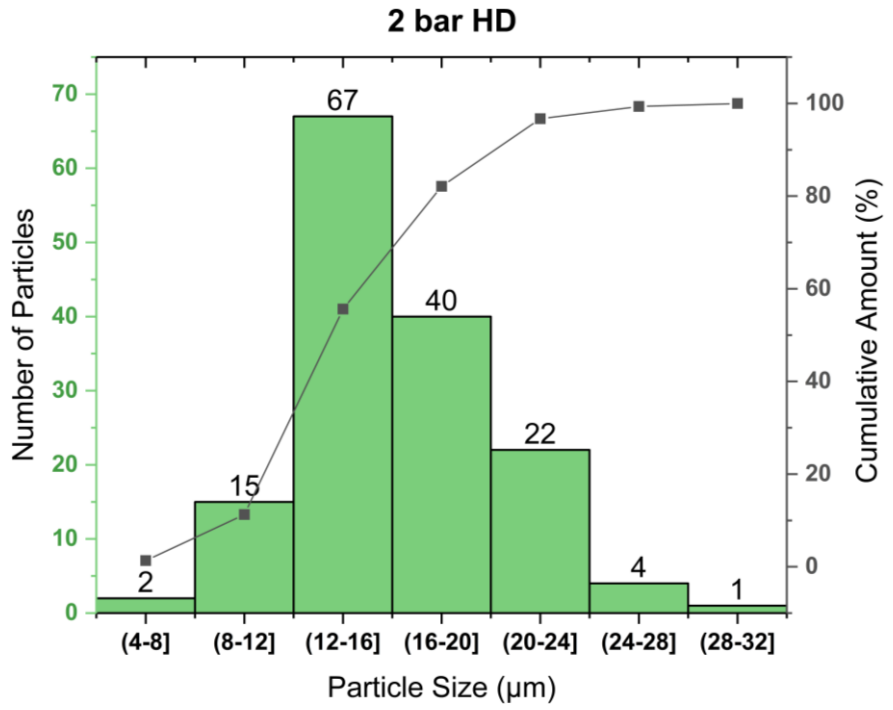

Figure 4.18 The graph of the particle size distribution for 2 bar HD powder

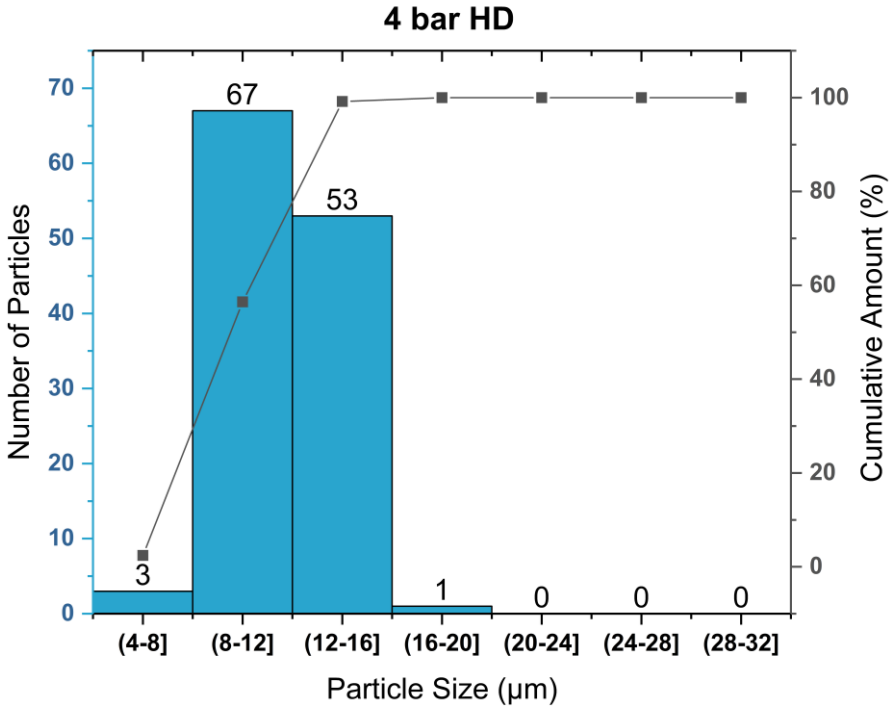

Figure 4.19 The graph of the particle size distribution for 4 bar HD powder

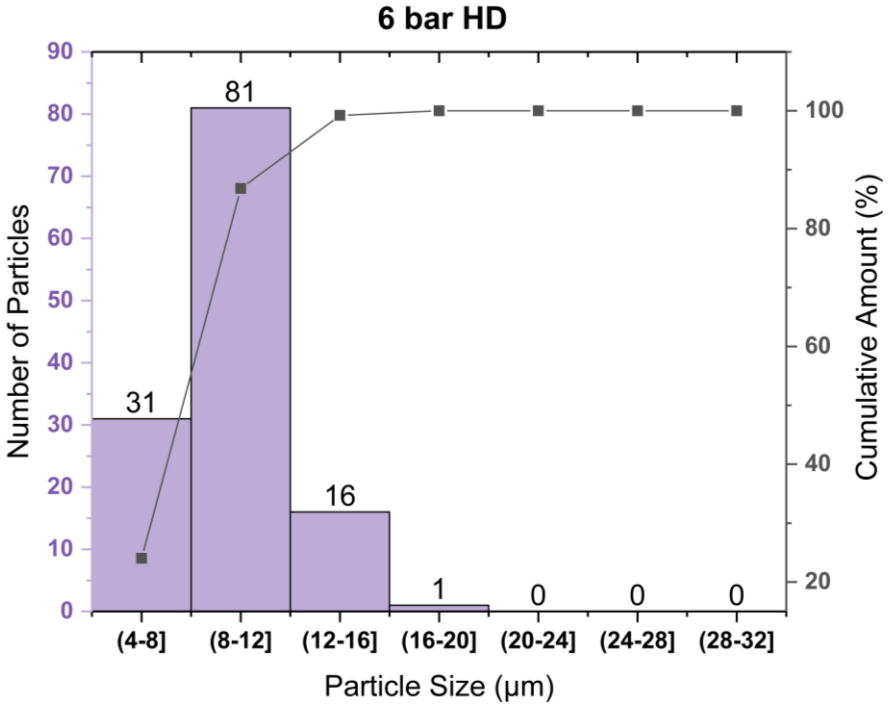

Figure 4.20 The graph of the particle size distribution for 6 bar HD powder

D10, D50, and D90 values calculated approximately according to the cumulative amount curves from particle size distribution graphs are presented in Table 4.10. Although an increased polycrystalline particle was observed in SEM images, it can be seen that increasing pressure decreased the particle size of small particles. The comparison of the D50 values showed that the particle size decreased by 21.1% when the pressure was raised from 2 bar to 4 bar and by 24.4% when the pressure was raised from 4 bar to 6 bar. The results indicate that the small particle size decreases almost linearly with increasing hydrogen pressure. However, with decreasing particle size, the size of the protective coating particles also decreased. Therefore, after the HD process at 6 bar, the separation of the coating from the powder was more challenging than the others.

Looking at the hydrogen content (Table 4.3) and volume change of the main matrix (Table 4.6), the lowest hydrogen content and volume change was observed in the 6 bar HD powder, but it has the lowest particle size distribution. Increasing pressure leads to an increase in hydrogen mobility. This might increase the concentration of

accumulating hydrogen at grain boundaries. This may also cause to occur hydrogen embrittlement [12], leading to localized stress concentrations —not just the volume expansion— and particles may become more fragile.

Table 4.10 D10, D50, and D90 values based on the cumulative amount after the HD process

	D10 (µm)	**D50 (µm)**	**D90 (µm)**
2 bar HD	9	14.25	20
4 bar HD	7.25	11.25	19
6 bar HD	5.5	8.5	12

Based on the LECO and XRD analysis results, 4 bar HD powder had the lowest oxygen content with the highest $Nd_2Fe_{14}BH_{3.31}$ phase formation, although 6 bar HD has the lowest particle size distribution. Since these characteristics have the potential to improve the overall quality and performance of the finished product, 4 bar HD powder is therefore considered to be more suitable for the subsequent ball-milling step.

The calculated average particle diameters for 2, 4, and 6 bar BM powders are 1.69 ± 0.75, 0.80 ± 0.38, and 0.85 ± 0.35 µm, respectively. Figure 4.21, Figure 4.22, and Figure 4.23 show the particle size distribution graphs of 2, 4, and 6 bar BM powders, respectively. The plots indicate that for 2, 4, and 6 bar BM powders, the Gaussian curve falls between 1.5-2, 0.4-0.6, and 0.6-0.8 µm, respectively.

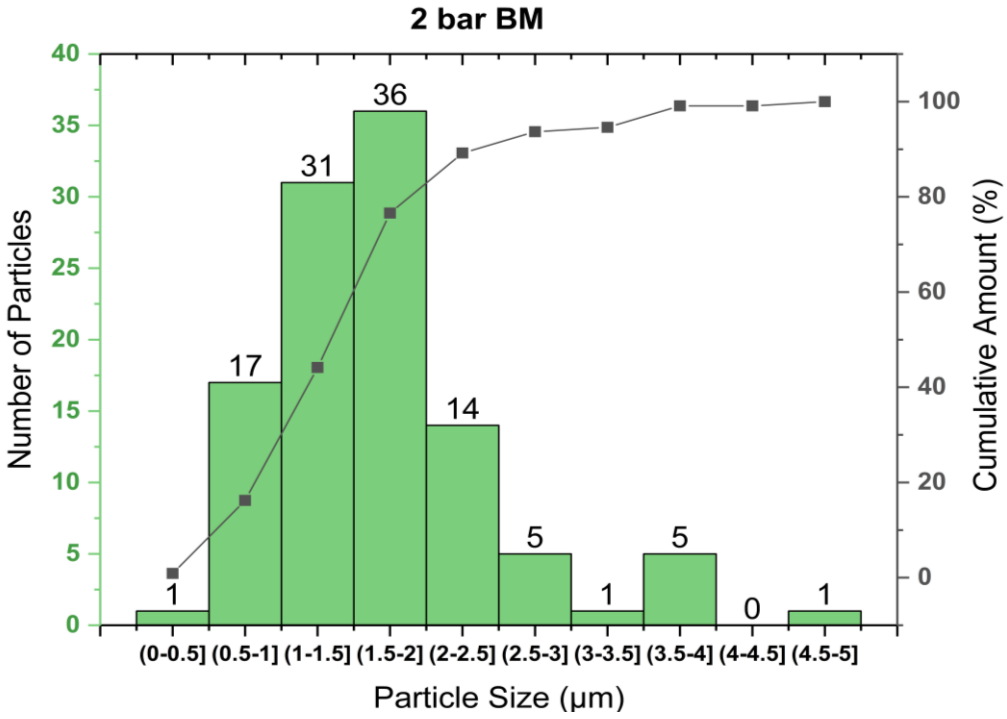

Figure 4.21 The graph of the particle size distribution for 2 bar BM powder

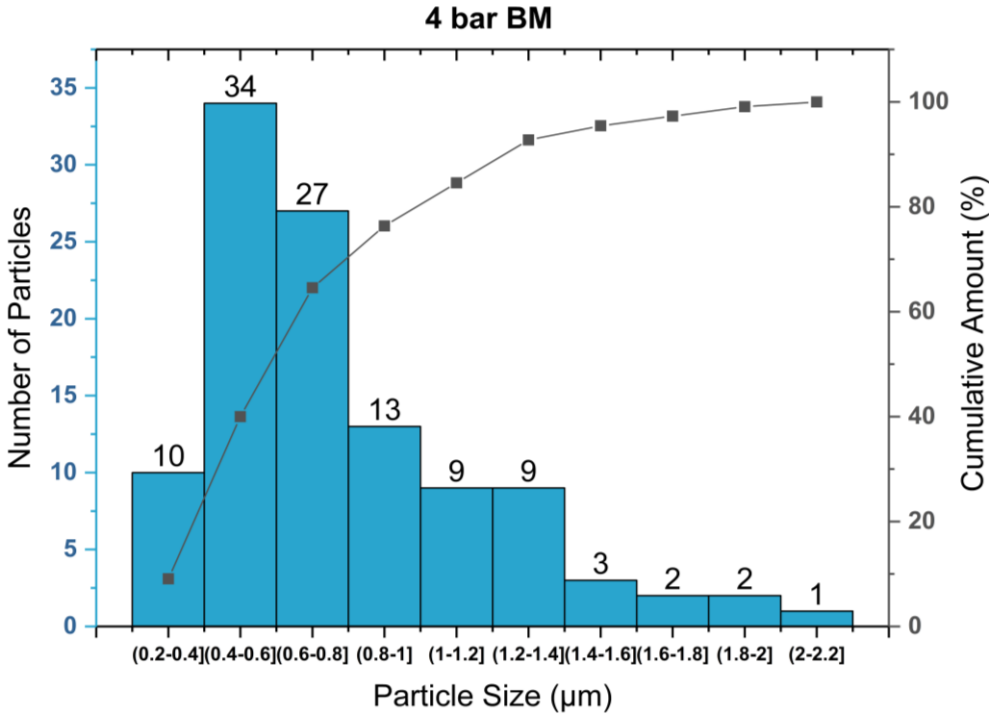

Figure 4.22 The graph of the particle size distribution for 4 bar BM powder

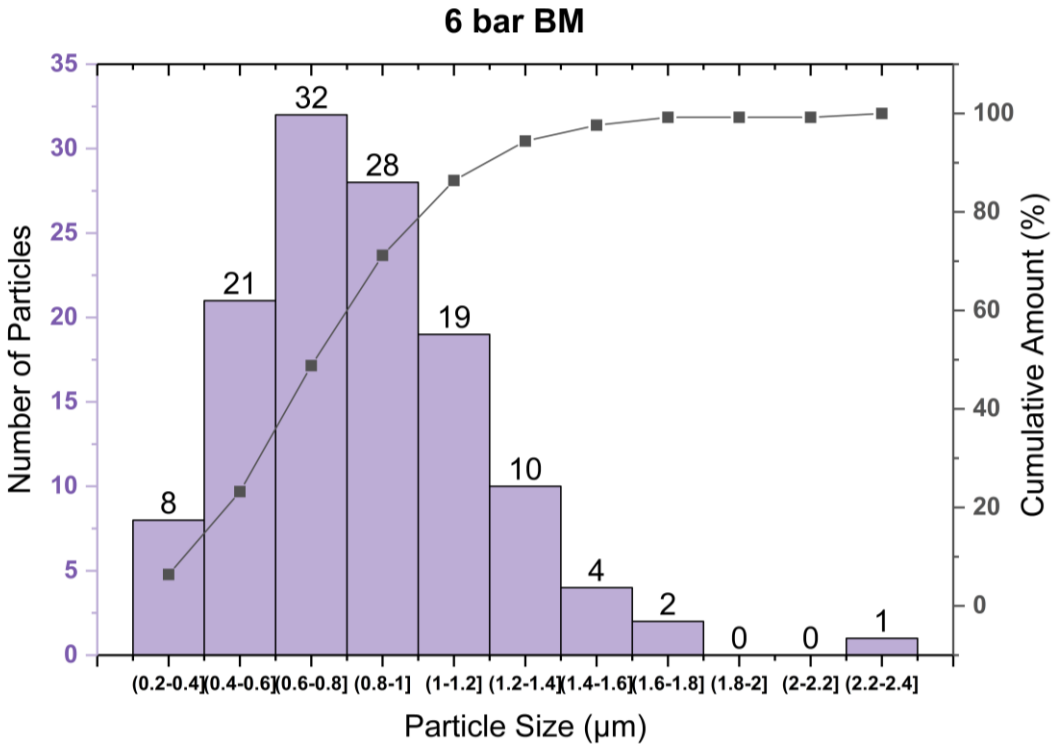

Figure 4.23 The graph of the particle size distribution for 6 bar BM powder

Table 4.11 displays the approximate D10, D50, and D90 values based on the percentage of cumulative amount. After ball-milling, there was a significant decrease in particle size. While the 4 bar and 6 bar BM powders exhibited similar particle size distributions, analysis of D50 values revealed that the 4 bar BM powder had the smallest distribution, followed by the 6 bar and 2 bar BM powders. The small difference in the D50 values of 6 bar HD and 4 bar HD may be due to the higher density of polycrystalline particles. Besides, the fact that they have a similar distribution may indicate that hydrogen makes the 4 bar HD more fragile. In addition, XRD data indicated that the volume expansion of the 4 bar HD powder was greater than the others. Consequently, this increased brittleness may account for the smaller D50 value observed in the 4 bar BM powder.

Table 4.11 D10, D50, and D90 values based on the percentage of the cumulative amount after ball-milling

	D10 (µm)	**D50 (µm)**	**D90 (µm)**
2 bar BM	0.6	1.4	2.4
4 bar BM	0.3	0.6	1.25
6 bar BM	0.3	0.75	1.2

As noted in Chapter 2, the optimum particle size range for ideal performance is between 3-6 µm. Achieving the ideal particle size is crucial to obtaining the desired microstructure and density in the production of PMs, as it directly affects the performance and properties of the magnet. Optimal alignment and interaction between magnetic grains are facilitated by proper particle size, which results in enhanced magnetic performance reflected by higher maximum energy product (BH)max. However, much smaller particle sizes than the desired particle sizes were obtained with the BM process. This excessive reduction in particle size indicates that the ball-milling time was too long.

CHAPTER 5

CONCLUSION AND FUTURE RECOMMENDATIONS

5.1 Conclusions

1. In the composition analysis of the scrap NdFeB magnet, which is the starting material, it was observed that it was compatible with the composition of the standard HDD NdFeB magnets. EDS results indicated that oxygen was present in the protective coating. This was expected since the coating is likely to damage the magnet due to long-term use.
2. In the microstructural analysis performed after the HD process, it was determined that the intergranular fracture mode was more dominant, and spherical Nd-rich particles were found in the structure and these findings were found to be consistent with the literature.
3. In addition to the microstructural analysis observations, an increased polycrystalline particles density was observed with increasing pressure. This was attributed to the fact that as the pressure increases, the diffusion rate differences between the host matrix and the grain boundary decrease, which may reduce the stress needed to break the particles, which is also consistent with the literature.
4. In magnetic measurement analysis, the H_c value of the raw scrap magnet was determined as 2555 Oe and M_r value as 141 emu/g. After the HD process, it was observed that the H_c values of HD powders remained below the limit (125 Oe) of being hard magnetic material, i.e. they turned into soft magnetic material. Meanwhile, the fact that hydrogen demagnetizes the magnet by entering the structure has been proven.
5. Interestingly, M/H measurements of the BM process after the HD process showed an increase in the H_c value of the powders. This phenomenon has not

been studied in the literature, but it is thought that the increased domain boundary density associated with decreasing particle size may have increased the coercivity.

6. The expectation that the hydrogen content would increase with increasing pressure during the HD process was in contradiction with the LECO analysis. This situation was evaluated in 2 different approaches. (1) Increased hydrogen pressure accelerates the diffusion kinetics, allowing hydrogen to enter and exit the structure more rapidly. (2) Hydrogenated powders at pressures higher than 1 bar, can release residual hydrogen when placed under the pressure of 1 bar, as well as increasing pressure enhances hydrogen solubility. Therefore, LECO analysis at room temperature and 1 bar may not accurately indicate actual hydrogen content.
7. According to the LECO results, it was found that the oxygen ratio increased significantly after ball-milling. On the other hand, it was suggested that the increased hydrogen content may be due to the toluene ($C_6H_5CH_3$) used as liquid media in the BM process or moisture environment in the glove box, but this situation requires further investigation.
8. In the XRD phase analysis of scrap NdFeB magnet, $Nd_2Fe_{14}B$ and Nd_2O_3 phases were found and it was mentioned that the presence of the oxide phase is expected due to the damaged coating.
9. After the HD process, the formation of $Nd_2Fe_{14}BH_{3.31}$ and Nd_2O_3 phases were observed in XRD phase analysis in accordance with the literature. The fact that hydrogen enters the crystal structure without altering the space group or microstructure was mentioned since it was observed that the main matrix phase crystallizes in P 42/mnm (space group no= 136) tetragonal crystal structure, which also belongs to the 2:14:1 structure.
10. Although it is generally accepted that the NdH_2 phase is formed after HD treatment at room temperature, previous studies have reported that the NdH_2 phase is not formed at low temperatures. The absence of NdH_2 phase formation in this study contributed to the previous studies. In addition, it was

stated that an increase in the oxygen content may have been caused by the lack of formation of the NdH_2 phase, which acts as protection against oxidation.

11. When the XRD analysis results of scrap NdFeB magnet and HD powders were compared, an increase in the lattice parameters and a left shift in the peaks of HD powders were observed. These findings indicated that the conditions for hydrogen to enter the structure and cause volume expansion were provided. However, the fact that the 6 bar HD had the lowest volume expansion was attributed to the reduced stress between the main matrix and grain boundary.
12. After the HD process, the LECO analysis results were found to be compatible with the XRD phase analysis results. According to XRD phase analysis results, the optimal results were obtained in 4 bar HD powder with the formation of the highest main phase (96.6 wt% $Nd_2Fe_{14}BH_{3.31}$) and the lowest oxide phase (3 wt% Nd_2O_3).
13. XRD phase analysis revealed the formation of $Nd_2Fe_{14}BH_{3.31}$ and Nd_2O_3 phases during the BM process, which is consistent with that of HD powders. Although the LECO results showed an increase in oxygen after ball-milling, XRD phase analysis demonstrated a decrease in the content of the oxide phase. It was stated that due to the broadening observed in the peaks after the BM process, the weak signals of the oxide phases may have remained under the dominant peaks in the XRD analysis, masking or overlapping them, making their detection difficult.
14. Upon comparison to HD powders, ball-milling results in decreased lattice parameters, increased FWHM values, confirming peak broadening, and reduced crystallite size with increased microstrain. It was stated that these changes were caused by the reduction in particle size.
15. Particle size analysis revealed a 21.2% decrease in size between 2 bar HD and 4 bar HD powder, and a 24.4% decrease between 4 bar HD and 6 bar HD powder, with the 6 bar HD powder exhibiting the smallest particle size

distribution. Therefore, it was indicated that the increase in hydrogen pressure leads to a decrease in size. However, it was reported that it was more difficult to separate the protective coating from 6 bar HD powders.

16. When the particle size distribution results were evaluated together with LECO and XRD results, it was seen that 4 bar HD powder was more suitable for further processing.
17. After the ball-mill process, the smallest particle size distribution according to D50 values was observed in 4 bar BM powder. It was suggested that this may be due to the fact that 4 bar HD has the highest volume expansion according to XRD analysis results.
18. In the BM process, the target particle size range was not achieved, resulting in excessively decreased particle sizes. For this reason, it was determined that the ball-milling process time was too long.

5.2 Future Recommendations

- Comparison of magnetic properties of scrap NdFeB magnets and magnets produced after optimization of ball milling time at 4 bar HD could be a research topic.
- To identify the underlying causes of the observed increase in coercivity after ball milling, more research is required. Microstructure analysis, association with grain size distribution, and domain wall behavior analysis may all be part of this investigation.
- Since NdH_2 is not formed at low temperatures, the changes in oxidation rates in the structure after HD and BM processes with NdH_2 doping can be compared with this study.
- By maintaining the HD process at a constant pressure of 4 bar, the changes in the structure at varying temperatures can be observed.

- Since hydrogen solubility and stability of phases change with pressure, a study can be carried out using computational modeling or simulation to predict them.

REFERENCES

[1] J. M. D. Coey, “Hard magnetic materials: A perspective,” *IEEE Trans Magn*, vol. 47, no. 12, pp. 4671–4681, Dec. 2011, doi: 10.1109/TMAG.2011.2166975.

[2] J. Lucas, P. Lucas, T. Le Mercier, A. Rollat, and W. Davenport, “Permanent Magnets Based on Rare Earths: Fundamentals,” in *Rare Earths*, Elsevier, 2015, ch. 13, pp. 213–230. doi: 10.1016/b978-0-444-62735-3.00013-9.

[3] A. Trench and J. P. Sykes, “Rare Earth Permanent Magnets and Their Place in the Future Economy,” *Engineering*, vol. 6, no. 2, pp. 115–118, Feb. 2020, doi: 10.1016/j.eng.2019.12.007.

[4] U. Geological Survey, “Mineral Commodity Summaries 2024,” 2024.

[5] European Commission, “Study on the Critical Raw Materials for the EU 2023 – Final Report,” 2023.

[6] S. Massari and M. Ruberti, “Rare earth elements as critical raw materials: Focus on international markets and future strategies,” *Resources Policy*, vol. 38, no. 1, pp. 36–43, Mar. 2013, doi: 10.1016/j.resourpol.2012.07.001.

[7] A. Hajalilou, M. Tavakoli, and E. Parvini, “Introduction to Magnetic Materials,” in *Magnetic Nanoparticles*, Wiley, 2022, pp. 1–16. doi: 10.1002/9783527840762.ch1.

[8] J. S. Galsin, “Magnetism,” in *Solid State Physics*, Elsevier, 2019, pp. 383–405. doi: 10.1016/B978-0-12-817103-5.00018-9.

[9] N. A. Spaldin, *Magnetic Materials Fundamentals and Applications*. Cambridge University Press, 2010.

[10] K. H. J. Buschow and F. R. Boer, *Physics of Magnetism and Magnetic Materials*. 2003. doi: 10.1007/978-0-306-48408-7.

[11] M. E. Mchenry and D. E. Laughlin, “Magnetic Moment and Magnetization,” 2012, doi: 10.1002/0471266965.com042.pub2.

[12] I. R. Harris and G. W. Jewell, “Rare-earth magnets: properties, processing and applications,” 2012. doi: 10.1016/9780857096371.4.600.

[13] K. H. J. Buschow, “Magnetism and processing of permanent magnet materials,” in *Handbook of Magnetic Materials*, vol. 10, 1997, pp. 463–593. doi: 10.1016/S1567-2719(97)10008-7.

[14] D. C. Jiles, “Recent advances and future directions in magnetic materials,” *Acta Mater*, vol. 51, no. 19, pp. 5907–5939, Nov. 2003, doi: 10.1016/j.actamat.2003.08.011.

[15] J. M. D. Coey, *Magnetism and Magnetic Materials*. Cambridge University Press, 2010. doi: 10.1017/CBO9780511845000.

[16] Y. Liu, D. J. Sellmyer, and D. Shindo, Eds., *Handbook of Advanced Magnetic Materials*. Springer, 2006.

[17] R. Skomski, “Permanent magnets: History, current research, and outlook,” in *Springer Series in Materials Science*, vol. 231, Springer Verlag, 2016, pp. 359–395. doi: 10.1007/978-3-319-26106-5_9.

[18] D. Jiles, *Introduction to Magnetism and Magnetic Materials*. Springer US, 1991. doi: 10.1007/978-1-4615-3868-4.

[19] S. Fähler and L. Schultz, “Magnetic Films: Hard,” pp. 4767–4771, 2001, doi: 10.1016/B0-08-043152-6/00833-0.

[20] K. H. J. Buschow, “Permanent Magnet Materials Based on 3d-rich Ternary Compounds,” in *Handbook of Ferromagnetic Materials*, vol. 4, 1988, pp. 1–129. doi: 10.1016/S1574-9304(05)80076-8.

[21] A. Habibzadeh, M. A. Kucuker, and M. Gökelma, “Review on the Parameters of Recycling NdFeB Magnets via a Hydrogenation Process,” May 23, 2023, *American Chemical Society*. doi: 10.1021/acsomega.3c00299.

[22] J. Cui *et al.*, “Manufacturing Processes for Permanent Magnets: Part I—Sintering and Casting,” 2022, *Springer*. doi: 10.1007/s11837-022-05156-9.

[23] J. Cui *et al.*, “Manufacturing Processes for Permanent Magnets: Part II—Bonding and Emerging Methods,” Jun. 01, 2022, *Springer*. doi: 10.1007/s11837-022-05188-1.

[24] E. P. Furlani, “Permanent Magnet Applications,” in *Permanent Magnet and Electromechanical Devices*, 2001, pp. 207–333. doi: 10.1016/B978-012269951-1/50005-X.

[25] J. Ormerod, “Permanent magnet markets and applications,” in *Modern Permanent Magnets*, Elsevier, 2022, pp. 403–434. doi: 10.1016/B978-0-323-88658-1.00012-1.

[26] K. Strnat, G. Hoffer, J. Olson, W. Ostertag, and J. J. Becker, “A family of new cobalt-base permanent magnet materials,” *J Appl Phys*, vol. 38, no. 3, pp. 1001–1002, 1967, doi: 10.1063/1.1709459.

[27] J. M. D. Coey, *Perspective and Prospects for Rare Earth Permanent Magnets*, vol. 6, no. 2. Elsevier Ltd, 2020. doi: 10.1016/j.eng.2018.11.034.

[28] K. J. Strnat, “A Review of Rare-Earth Permanent Magnets, Applicatons and Prospects,” in *New Frontiers in Rare Earth Science and Applications*, vol. 2, 1985, pp. 872–878. doi: 10.1016/B978-0-12-767662-3.50036-X.

[29] J. J. Croat and J. Ormerod, “The history of permanent -magnets,” in *Modern Permanent Magnets*, Elsevier, 2022, pp. 1–30. doi: 10.1016/B978-0-323-88658-1.00004-2.

[30] J. Lucas, P. Lucas, T. Le Mercier, A. Rollat, and W. Davenport, “Rare Earth-Based Permanent Magnets Preparation and Uses,” in *Rare Earths*, Elsevier, 2015, pp. 231–249. doi: 10.1016/b978-0-444-62735-3.00019-x.

[31] K. Narasimhan, “Fundamental properties of permanent magnets,” in *Modern Permanent Magnets*, Elsevier, 2022, pp. 31–64. doi: 10.1016/B978-0-323-88658-1.00005-4.

[32] J. J. Croat, J. F. Herbst, R. W. Lee, and F. E. Pinkerton, “Pr-Fe and Nd-Fe-based materials: A new class of high-performance permanent magnets (invited),” 1984.

[33] M. Sagawa, S. Fujimura, N. Togawa, H. Yamamoto, and Y. Matsuura, “New material for permanent magnets on a base of Nd and Fe (invited),” *J Appl Phys*, vol. 55, no. 6, pp. 2083–2087, 1984, doi: 10.1063/1.333572.

[34] J. F. Herbst, J. J. Croat, F. E. Pinkerton, and W. B. Yelon, “Relationships between crystal structure and magnetic properties in Nd2Fe14B,” *Phys Rev B*, vol. 29, no. 7, pp. 4176–4178, 1984, doi: 10.1103/PhysRevB.29.4176.

[35] J. M. Friedt, A. Vasquez, J. P. Sanchez, P. L. Heritier, and Fruchart R, “Magnetism and crystal field properties of the RE2Fe14 BHx, alloys (RE=Y, Ce, Dy, Er) from Mossbauer spectroscopy,” *Journal of Physics F: Metal Physics*, vol. 16, pp. 65–66, 1986, doi: 10.1088/0305-4608/16/5/013.

[36] D. Frucharta, S. Miraglia, S. Obbade, R. Verhoefb, and P. Wolfers, “Crystal and non-colinear magnetic structures of R,Fe 14B, R=Nd, Ho,” *Physica B*, vol. 180, pp. 578–580, 1992.

[37] J. F. Herbst, “R2Fe14B materials: Intrinsic properties and technological aspects,” *Rev Mod Phys*, vol. 63, no. 4, pp. 819–898, 1991, doi: 10.1103/RevModPhys.63.819.

[38] B. E. Davies, R. S. Mottram, and I. R. Harris, “Recent developments in the sintering of NdFeB,” in *Materials Chemistry and Physics*, vol. 67, 2001, pp. 272–281. doi: 10.1016/S0254-0584(00)00450-8.

[39] Y. Kaneko, “Highest Performance of Nd-Fe-B Magnet Over 55 MGOe,” *IEEE Transactions on Magnetics* , vol. 36, no. 5, pp. 3275–3278, 2000, doi: 10.1109/20.908767.

[40] K. Buschow, “New Permanent Magnet Materials,” in *Materials Science Reports*, vol. 1, 1986, pp. 1–63. doi: 10.1016/0920-2307(86)90003-4.

[41] Y. Matsuura, S. Hirosawa, H. Yamamoto, S. Fujimura, M. Sagawa, and K. Osamura, “Phase diagram of the nd-fe-b ternary system,” *Jpn J Appl Phys*, vol. 24, no. 8, pp. 635–637, 1985, doi: 10.1143/JJAP.24.L635.

[42] V. Raghavan, “B-Fe-Nd (Boron-Iron-Neodymium),” *Phase Diagram Evaluations*, vol. 24, pp. 451–454, 2003, doi: 10.1361/105497103770330136.

[43] S. Ozawa, K. Kuribayashi, S. Hirosawa, S. Reutzel, and D. M. Herlach, “Heat treatment of metastable Nd2Fe17Bx phase formed from undercooled melt of Nd-Fe-B alloys,” *J Appl Phys*, vol. 100, no. 12, 2006, doi: 10.1063/1.2386943.

[44] M. Sagawa, S. Hirosawa, Y. Hitoshi, S. Fujimura, and Y. Matsuura, “Nd–Fe–B Permanent Magnet Materials,” *Japanese Journal of Applied Physics*, vol. 26, 1987, doi: 10.1143/JJAP.26.785.

[45] J. He *et al.*, “Grain boundary diffusion sources and their coating methods for nd-fe-b permanent magnets,” Sep. 01, 2021, *MDPI*. doi: 10.3390/met11091434.

[46] T. G. Woodcock *et al.*, “Understanding the microstructure and coercivity of high performance NdFeB-based magnets,” *Scr Mater*, vol. 67, no. 6, pp. 536–541, 2012, doi: 10.1016/j.scriptamat.2012.05.038.

[47] S. Hirosawa, Y. Matsuura, H. Yamamoto, S. Fujimura, M. Sagawa, and H. Yamauchi, “Magnetization and magnetic anisotropy of R2Fe14B measured

on single crystals," *J Appl Phys*, vol. 59, no. 3, pp. 873–879, 1986, doi: 10.1063/1.336611.

[48] E. A. Périgo *et al.*, "Small-angle neutron scattering study of coercivity enhancement in grain-boundary-diffused Nd-Fe-B sintered magnets," *J Alloys Compd*, vol. 677, pp. 139–142, Aug. 2016, doi: 10.1016/j.jallcom.2016.03.160.

[49] H. Chen, R. Wang, J. Li, and Y. Liu, "Evolution of Nd-rich phase distribution in Hot-Deformed Nd-Fe-B magnets with different height reductions," *J Magn Magn Mater*, vol. 565, Jan. 2023, doi: 10.1016/j.jmmm.2022.170235.

[50] P. J. Mcguiness, I. R. Harris, E. Rozendaal, J. Ormerod, and M. Ward, "The production of a Nd-Fe-B permanent magnet by a hydrogen decrepitation/attritor milling route," *J Mater Sci*, vol. 21, pp. 4107–4110, 1986, doi: 10.1007/BF02431659.

[51] N. Eliaz, D. Eliezer, and D. L. Olson, "Hydrogen-assisted processing of materials," *Materials Science and Engineering*, vol. 289, pp. 41–53, 2000, doi: 10.1016/S0921-5093(00)00906-0.

[52] M. Yue *et al.*, "Crystallographic alignment evolution and magnetic properties of Nd-Fe-B nanoflakes prepared by surfactant-assisted ball milling," in *Journal of Applied Physics*, Apr. 2012. doi: 10.1063/1.3679414.

[53] A. M. Gabay, Y. Zhang, and G. C. Hadjipanayis, "Effect of Cu and Ga additions on the anisotropy of R2Fe 14B/α-Fe nanocomposite die-upset magnets (R=Pr, Nd)," *J Magn Magn Mater*, vol. 302, no. 1, pp. 244–251, Jul. 2006, doi: 10.1016/j.jmmm.2005.09.013.

[54] X. An *et al.*, "High anisotropic NdFeB submicro/nanoflakes prepared by surfactant-assisted ball milling at low temperature," *J Magn Magn Mater*, vol. 442, pp. 279–287, Nov. 2017, doi: 10.1016/j.jmmm.2017.06.071.

[55] H. G. Cha, Y. H. Kim, C. W. Kim, H. W. Kwon, and Y. S. Kang, "Characterization and magnetic behavior of Fe and Nd-Fe-B nanoparticles by surfactant-capped high-energy ball mill," *Journal of Physical Chemistry C*, vol. 111, no. 3, pp. 1219–1222, Jan. 2007, doi: 10.1021/jp065997s.

[56] M. Yue, Y. P. Wang, N. Poudyal, C. B. Rong, and J. P. Liu, "Preparation of Nd-Fe-B nanoparticles by surfactant-assisted ball milling technique," *J Appl Phys*, vol. 105, no. 7, 2009, doi: 10.1063/1.3059228.

[57] M. Jurczyk, J. S. Cook, and S. J. Collocott, "Application of high energy ball milling to the magnetic powders from NdFeB-type alloys," *J Alloys Compd*, vol. 217, no. 1, pp. 65–68, 1995, doi: 10.1016/0925-8388(94)01291-O.

[58] H. Sepehri-Amin, Y. Une, T. Ohkubo, K. Hono, and M. Sagawa, "Microstructure of fine-grained Nd-Fe-B sintered magnets with high coercivity," *Scr Mater*, vol. 65, no. 5, pp. 396–399, Sep. 2011, doi: 10.1016/j.scriptamat.2011.05.006.

[59] T. T. Sasaki, T. Ohkubo, K. Hono, Y. Une, and M. Sagawa, "Correlative multi-scale characterization of a fine grained Nd-Fe-B sintered magnet," *Ultramicroscopy*, vol. 132, pp. 222–226, Sep. 2013, doi: 10.1016/j.ultramic.2013.01.006.

[60] A. G. Popov, O. A. Golovnia, and V. A. Bykov, "Pressless process in route of obtaining sintered Nd-Fe-B magnets," *J Magn Magn Mater*, vol. 383, pp. 226–231, Jun. 2015, doi: 10.1016/j.jmmm.2014.10.140.

[61] A. S. Kim, "Effect of oxygen on magnetic properties of Nd-Fe-B magnets," *J Appl Phys*, vol. 64, no. 10, pp. 5571–5573, 1988, doi: 10.1063/1.342284.

[62] T. Minowa, M. Sbimao, and M. Honshima, "Microstructure of Nd-rich phase in Nd-Fe-B magnet containing oxygen and carbon impurities," 1991.

[63] S. Constantinides, “Permanent magnet coatings and testing procedures,” in *Modern Permanent Magnets*, Elsevier, 2022, pp. 371–402. doi: 10.1016/B978-0-323-88658-1.00011-X.

[64] P. Nothnagel, K.-H. Miiller, D. Eckert, and A. Handstein, “The influence of particle size on the coercivity of sintered NdFeB magnets,” 1991. doi: 10.1016/0304-8853(91)90786-A.

[65] S. Namkung, D. H. Kim, and T. S. Jang, “Effect Of Particle Size Distribution on the Microstructure and Magnetic Properties of Sintered NdFeB Magnets,” 2011.

[66] D. W. Scott, B. M. Ma, Y. L. Liang, and C. O. Bounds, “The effects of average grain size on the magnetic properties and corrosion resistance of NdFeB sintered magnets,” *J Appl Phys*, vol. 79, no. 8 PART 2A, pp. 5501–5503, Apr. 1996, doi: 10.1063/1.362291.

[67] W. F. Li, T. Ohkubo, K. Hono, and M. Sagawa, “The origin of coercivity decrease in fine grained Nd-Fe-B sintered magnets,” *J Magn Magn Mater*, vol. 321, no. 8, pp. 1100–1105, Apr. 2009, doi: 10.1016/j.jmmm.2008.10.032.

[68] S. H. Kim, J. W. Kim, T. S. Jo, and Y. Do Kim, “High coercive Nd-Fe-B magnets fabricated via two-step sintering,” *J Magn Magn Mater*, vol. 323, no. 22, pp. 2851–2854, Nov. 2011, doi: 10.1016/j.jmmm.2011.06.034.

[69] S. Guo, R. Chen, B. Zheng, G. Yan, D. Lee, and A. Yan, “Effect of temperature gradient on the microstructure of the rapidly solidified Nd-Fe-B strips,” *IEEE Trans Magn*, vol. 47, no. 10, pp. 3267–3269, 2011, doi: 10.1109/TMAG.2011.2146761.

[70] X. G. Cui *et al.*, “Effects of alignment on the magnetic and mechanical properties of sintered Nd-Fe-B magnets,” *J Alloys Compd*, vol. 563, pp. 161–164, Jun. 2013, doi: 10.1016/j.jallcom.2013.02.093.

[71] A. Walton *et al.*, “The use of hydrogen to separate and recycle neodymium-iron-boron-type magnets from electronic waste,” *J Clean Prod*, vol. 104, pp. 236–241, Oct. 2015, doi: 10.1016/j.jclepro.2015.05.033.

[72] G. Bacchetta, S. Luca, C. Rado, and S. Genevrier, “Short-loop recycling of sintered NdFeB magnets by hydrogen decrepitation,” 2022. [Online]. Available: https://cea.hal.science/cea-03864908

[73] Y. Yang *et al.*, “REE Recovery from End-of-Life NdFeB Permanent Magnet Scrap: A Critical Review,” *Journal of Sustainable Metallurgy*, vol. 3, no. 1, pp. 122–149, Mar. 2017, doi: 10.1007/s40831-016-0090-4.

[74] A. Piotrowicz, S. Pietrzyk, P. Noga, and L. Mycka, “The use of thermal hydrogen decrepitation to recycle Nd-Fe-B magnets from electronic waste,” *Journal of Mining and Metallurgy, Section B: Metallurgy*, vol. 56, no. 3, pp. 415–424, 2020, doi: 10.2298/JMMB200207032P.

[75] M. Kaya, “An overview of NdFeB magnets recycling technologies,” Apr. 01, 2024, *Elsevier B.V.* doi: 10.1016/j.cogsc.2024.100884.

[76] B. L. Checa Fernández, J. M. Martín, G. Sarriegui, and N. Burgos, “Effect of temperature on particle shape, size, and polycrystallinity of Nd-Fe-B powders obtained by hydrogen decrepitation,” *Journal of Materials Research and Technology*, vol. 24, pp. 1454–1467, May 2023, doi: 10.1016/j.jmrt.2023.03.076.

[77] V. A. Yartys, A. J. Williams, K. G. Knoch, P. J. Mcguiness, and I. R. Harris, “Further studies of anisotropic hydrogen decrepitation in Nd16Fe76B8 sintered magnets,” *J Alloys Compd*, vol. 239, no. 1, pp. 50–54, 1996, doi: https://doi.org/10.1016/0925-8388(95)02185-X.

[78] X. T. Li *et al.*, “Effect of hydrogen pressure on hydrogen absorption of waste Nd-Fe-B sintered magnets,” *J Magn Magn Mater*, vol. 473, pp. 144–147, Mar. 2019, doi: 10.1016/j.jmmm.2018.10.071.

[79] M. Verdier, J. Morros, D. Pere, and I. R. Harris, “Hydrogen Absorption Behaviours of Some Nd-Fe-B-Type Alloys,” *IEEE Trans Magn*, vol. 30, no. 2, pp. 660–662, 1994, doi: 10.1109/20.312368.

[80] M. A. R. Önal *et al.*, “Comparative oxidation behavior of Nd-Fe-B magnets for potential recycling methods: Effect of hydrogenation pre-treatment and magnet composition,” *J Alloys Compd*, vol. 728, pp. 727–738, 2017, doi: 10.1016/j.jallcom.2017.09.046.

[81] A. Habibzadeh, M. A. Kucuker, Ö. Çakır, and M. Gökelma, “Microstructural Investigation of Discarded NdFeB Magnets After Low-Temperature Hydrogenation,” *Journal of Sustainable Metallurgy*, vol. 10, no. 3, pp. 1141–1155, Sep. 2024, doi: 10.1007/s40831-024-00873-8.

[82] E. H. Lalana, “Permanent magnets and its production by powder metallurgy,” *Revista de Metalurgia*, vol. 54, no. 2, Apr. 2018, doi: 10.3989/revmetalm.121.

[83] M. Awais, F. Coelho, M. Degri, E. Herraiz, A. Walton, and N. Rowson, “Hydrocyclone separation of hydrogen decrepitated NdFeB,” *Recycling*, vol. 2, no. 4, 2017, doi: 10.3390/recycling2040022.

[84] I. R. Harris and P. J. Mcguiness, “Hydrogen: its use in the processing of NdFeB-type magnets,” 1991.

[85] O. Isnard, W. B. Yelon, S. Miraglia, and D. Fruchart, “Neutron-diffraction study of the insertion scheme of hydrogen in Nd 2Fe14B,” *J Appl Phys*, vol. 78, no. 3, pp. 1892–1898, 1995, doi: 10.1063/1.360720.

[86] D. Fruchart, S. Miraglia, P. de Rango, and P. Wolfers, “Hydrogen location in hard magnet materials: Scheme, fundamental aspects, processes,” *J Alloys Compd*, vol. 383, no. 1–2, pp. 17–22, Nov. 2004, doi: 10.1016/j.jallcom.2004.04.068.

[87] J. M. Cadogan and J. M. D. Coey, “Hydrogen absorption and desorption in Nd2Fe14B,” *Appl Phys Lett*, vol. 48, no. 6, pp. 442–444, 1986, doi: 10.1063/1.96525.

[88] K. Oesterreicher and H. Oesterreicher, “Structure and Magnetic Properties of Nd2Fe14BH2.7,” *Physica Status Solidi (a)*, vol. 85, no. 1, pp. 61–64, 1984, doi: 10.1002/pssa.2210850152.

[89] G. Wiesinger, G. Hilscher, and R. Grössinger, “Effect of hydrogen absorption on the magnetic properties of Nd15Fe77B8,” *Journal of the Less-Common Metals*, vol. 131, no. 1–2, pp. 409–417, 1987, doi: 10.1016/0022-5088(87)90540-6.

[90] L. Pareti, O. Moze, D. Fruchart, Ph. l’Heritier, and A. Yaouanc Mdih, “Effects of hydrogen absorption on the 3d and 4f anisotropies in RE2Fe14B (RE ≡ Y, Nd, Ho, Tm),” 1988. doi: 10.1016/0022-5088(88)90176-2.

[91] M. Zakotnik, I. R. Harris, and A. J. Williams, “Possible methods of recycling NdFeB-type sintered magnets using the HD/degassing process,” *J Alloys Compd*, vol. 450, no. 1–2, pp. 525–531, Feb. 2008, doi: 10.1016/j.jallcom.2007.01.134.

[92] P. A. Prokofev *et al.*, “Blending powder process for recycling sintered Nd-Fe-B magnets,” *Materials*, vol. 13, no. 14, Jul. 2020, doi: 10.3390/ma13143049.

[93] C. Li *et al.*, “Recycling of scrap sintered Nd–Fe–B magnets as anisotropic bonded magnets via hydrogen decrepitation process,” *J Mater Cycles Waste Manag*, vol. 17, no. 3, pp. 547–552, Jul. 2015, doi: 10.1007/s10163-014-0279-1.

[94] I. Boukhoubza, M. Khenfouch, M. Achehboune, B. M. Mothudi, I. Zorkani, and A. Jorio, “X-ray diffraction investigations of nanostructured ZnO coated with reduced graphene oxide,” in *Journal of Physics: Conference Series*, Institute of Physics Publishing, Sep. 2019. doi: 10.1088/1742-6596/1292/1/012011.

[95] A. Dańczak *et al.*, “The recycling-oriented material characterization of hard disk drives with special emphasis on NdFeB magnets,” *Physicochemical Problems of Mineral Processing*, vol. 54, no. 2, pp. 363–376, Apr. 2018, doi: 10.5277/ppmp1843.

[96] L. Schultz, A. M. El-Aziz, G. Barkleit, and K. Mummert, “Corrosion behaviour of Nd-Fe-B permanent magnetic alloys,” 1999.

[97] R. S. Sheridan, I. R. Harris, and A. Walton, “The development of microstructure during hydrogenation-disproportionation-desorption-recombination treatment of sintered neodymium-iron-boron-type magnets,” *J Magn Magn Mater*, vol. 401, pp. 455–462, Mar. 2016, doi: 10.1016/j.jmmm.2015.10.077.

[98] D. H. Alshora, M. A. Ibrahim, and F. K. Alanazi, “Nanotechnology from particle size reduction to enhancing aqueous solubility,” in *Surface Chemistry of Nanobiomaterials: Applications of Nanobiomaterials*, Elsevier Science Ltd., 2016, pp. 163–191. doi: 10.1016/B978-0-323-42861-3.00006-6.

[99] T. Ungár, “Microstructural parameters from X-ray diffraction peak broadening,” *Scr Mater*, vol. 51, no. 8 SPEC. ISS., pp. 777–781, 2004, doi: 10.1016/j.scriptamat.2004.05.007.